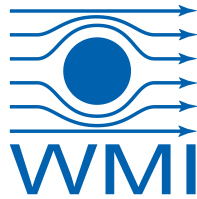




TECHNISCHE  
UNIVERSITÄT  
MÜNCHEN



WALTHER-MEISSNER-  
INSTITUT FÜR TIEF-  
TEMPERATURFORSCHUNG



BAYERISCHE  
AKADEMIE DER  
WISSENSCHAFTEN

# Spin-Pumping and Spin Wave Damping in $\text{Co}_{25}\text{Fe}_{75}$ Thin-Film Heterostructures

Master's Thesis  
Luis Flacke

Supervisor: Prof. Dr. Rudolf Gross  
Advisor: Dr. Mathias Weiler, Dr. Matthias Althammer  
Garching, May 2018

Fakultät für Physik  
TECHNISCHE UNIVERSITÄT MÜNCHEN

*“But the wisdom from above is first pure, then peaceable, gentle, open to reason, full of mercy and good fruits, impartial and sincere.”*

*- James 3, 17 - ESV*

# Contents

<b>1</b>	<b>Introduction</b>	<b>1</b>
<b>2</b>	<b>Fabrication</b>	<b>3</b>
2.1	Magnetron Sputter Deposition of $\text{Co}_{25}\text{Fe}_{75}$ . . . . .	5
2.2	X-Ray Reflectometry . . . . .	8
2.3	Micropatterning by Optical Lithography . . . . .	9
<b>3</b>	<b>Broadband Experiments - Magnetic Damping in <math>\text{Co}_{25}\text{Fe}_{75}</math></b>	<b>13</b>
3.1	Ferromagnetic Resonance . . . . .	13
3.2	Spin Pumping . . . . .	16
3.3	Experimental Technique and Setup . . . . .	17
3.4	Data Processing . . . . .	21
3.5	Experimental Results . . . . .	22
3.5.1	Ta - Cu - $\text{Co}_{25}\text{Fe}_{75}$ - Cu - Ta . . . . .	22
3.5.2	Pt - $\text{Co}_{25}\text{Fe}_{75}$ - Ta . . . . .	26
3.5.3	Pt - Cu - $\text{Co}_{25}\text{Fe}_{75}$ - Cu - Ta . . . . .	29
3.5.4	Ta - Al - $\text{Co}_{25}\text{Fe}_{75}$ - Al - Ta . . . . .	32
3.5.5	Comparison . . . . .	35
<b>4</b>	<b>Magneto-Optical Detection of FMR and Spin Wave Propagation in Structured <math>\text{Co}_{25}\text{Fe}_{75}</math></b>	<b>39</b>
4.1	Fundamentals and Setup of BLS . . . . .	39
4.2	Experimental Results . . . . .	44
<b>5</b>	<b>Summary and Outlook</b>	<b>51</b>
<b>A</b>	<b>Sputter Deposition Parameters</b>	<b>55</b>
<b>B</b>	<b>Magnetic Properties for Blanket Films</b>	<b>67</b>
<b>C</b>	<b>Frequently Encountered Issues with the PicoMaster 200</b>	<b>71</b>
C.1	Focus Capture . . . . .	71
C.2	Module Collision and Misalignment . . . . .	72
<b>D</b>	<b>Laserlithography - Optimization Parameters</b>	<b>75</b>

**Literature****85**

# Chapter 1

## Introduction

Since the discovery of the transistor in the mid-19s [1], computational technologies saw an uprising with ever increasing progress. The miniaturization enabled "cramming more components onto integrated circuits", which is Moore's publication title, which predicted a doubling of components in integrated circuits each year [2]. Even though this prognosis was adapted later on to every two years, the augmentation in component density kept going for a long time but is soon going to face fundamental physical limits [3]. On the one hand, quantum effects like tunneling hinder the shrinking of transistors at a certain limit. On the other hand Joule heating becomes a serious issue when heat accumulates between the components [3]. Due to the increasing cost of further miniaturization, the semiconductor industry has now abandoned its strict pursuit of Moore's law. Researching alternative and complimentary approaches to semiconductor transistor technology is thus of utmost interest for securing the further advance of computer technologies.

The implementation of magnetism in computational devices had a severe impact on a before purely electronic based industry. With the Nobel prize winning discovery of the GMR effect by Albert Fert [4] and Peter Grünberg [5], a milestone in the integrated circuit industry was set. The usage of spin selective devices enabled high density hard drives and many other technologies. A new sector: *spintronics* was born where electronic devices benefit from also using the spin component of the electron. There are a lot of possible applications like, e. g. spin transfer torque magnetic random access memory, where Guenole *et al.* reported of sub-ns switching [6]. Another interesting field is the conversion of dc-current into magnetic microwave signals by spin-Hall nano-oscillators. Here, magnetic auto-oscillations are driven by pure spin currents [7]. In the field of magnonics, the information transport by spin wave propagation, which does not necessarily suffer from Joule heating, is studied. All of these applications are subject to contemporary research.

An important factor for the usage of the spin degree of freedom in these examples is the magnetic damping. By diminishing the magnetodynamic relaxation, the presented applications become more efficient and benefit from longer attenuation length scales of spin waves. In many devices the transport of electric charge stays a crucial part, which impedes the implementation of electric insulators even though electrically inert magnetic materials tend to exhibit lower damping parameters in insulating phases than their metallic counterparts. It is thus of major interest to find electrically conducting materials which also perform well in respect to the magnetodynamic relaxation. Schoen *et al.* recently reported on ultra-low damping in  $\text{Co}_{25}\text{Fe}_{75}$  [8], which motivated the work realized throughout

this thesis. The research done was focused on systematically investigating home grown heterostructures containing  $\text{Co}_{25}\text{Fe}_{75}$  as a FM layer with respect to their magnetic damping properties and spin pumping contributions.

In **chapter 2**, the fabrication process of the samples will be presented. In the first part, magnetron sputter deposition is discussed which was used to grow our multilayer samples. A layer thickness check was performed for each sample by XRD, whose physical basics are shortly presented. In a third step, the optical lithography and spin coating process for microstructured samples for Brillouin Light Scattering (BLS) experiments is introduced.

**Chapter 3** engages in the broadband ferromagnetic resonance (bbFMR) experiments realized on blanket film samples. First, the theoretical background for the experiments is addressed, including the FMR and the occurring spin pumping. The experimental setup and data processing is clarified and different samples series and the experimental results are discussed afterwards.

In **chapter 4** we deal with optical measurements, viz. BLS, on micropatterned samples. A physical introduction to BLS and the experimental setup is given. In a second part, optical FMR and spin wave propagation in our structured samples is discussed and compared to our results in chapter 3.

A short summary and outlook is given in **chapter 5** presenting the most important results and hinting towards possible successive investigation.

**Appendix A** and **B** show the fabrication parameters and magnetic properties for the deposited blanket film samples, respectively.

In **appendix C**, frequently encountered issues with the laser writing machine are explained and a work around solution - if available - is presented.

A new spin coating process was developed during this thesis. In **appendix D** the spin coating parameters, exposure dose and resulting error counts from the writing unit "PicoMaster 200" are presented in the tabular form.

# Chapter 2

## Fabrication

Low-damping metallic ferromagnets with high saturation magnetization are ideally suited for many spintronic applications. Driving magnetic nano-oscillators via the spin-orbit torque would benefit from lower current densities [9]. Also spin wave propagation will be facilitated this way, leading to higher decay lengths [10]. In their work, Martin A. W. Schoen *et al.* [8] reported ultra-low magnetic damping in  $\text{Co}_{25}\text{Fe}_{75}$  (see Fig. 2.1), with a large saturation magnetization of  $\mu_0 M_S = 2.4 \text{ T}$ . The calculation of the Gilbert damping in  $\text{Co}_x\text{Fe}_{1-x}$  alloys has been attempted before this seminal experimental work [11, 12] but theory predicted the energy dissipation's minimum between  $x = 10 \%$  and  $x = 20 \%$  (see Fig. 2.2). In general, deriving an accurate expression of the Gilbert damping in ferromagnetic metal alloys is a non-trivial task. Still, this magnetic property plays a crucial role in the development of spintronic devices. Hence, several theoretical groups tackled this challenge [11–16]. A more recent derivation from Turek *et al.* [17] relying on non-local torque operators instead of traditional local torques operators predicts the damping minimum for  $x = 25\%$ , matching reasonably well with the experimental data in Ref. [8].

The common denominator of all these theories explaining the dip in damping is the direct proportionality to the density of states (DOS) at the Fermi-surface. In Fig. 2.2 the analogous behavior of DOS to magnetic damping in dependence of Co-concentration is illustrated. Schoen *et al.* argue that actually all other contributions are fairly unchanged when varying the  $\text{Co}_x\text{Fe}_{1-x}$  composition  $x$ . Indeed, the spin-orbit coupling is comparable for Co and Fe and also the broadening of electron states at the Fermi level due to alloying is rather small [8]. Therefore, the dip in the DOS is also observed in the Gilbert damping parameter.

Even though metallic ferromagnets (FMs) exhibit higher damping than insulating FMs due to the additional electron-phonon scattering mechanisms,  $\text{Co}_{25}\text{Fe}_{75}$  appears to be a good candidate for spintronic devices. Not only does it fulfill the requirement of being an itinerant FMs, but it also comes close to the low Gilbert damping regime of insulating FMs. Taking all these intriguing properties into account,  $\text{Co}_{25}\text{Fe}_{75}$  was identified as a suitable material for the investigations presented in this work.

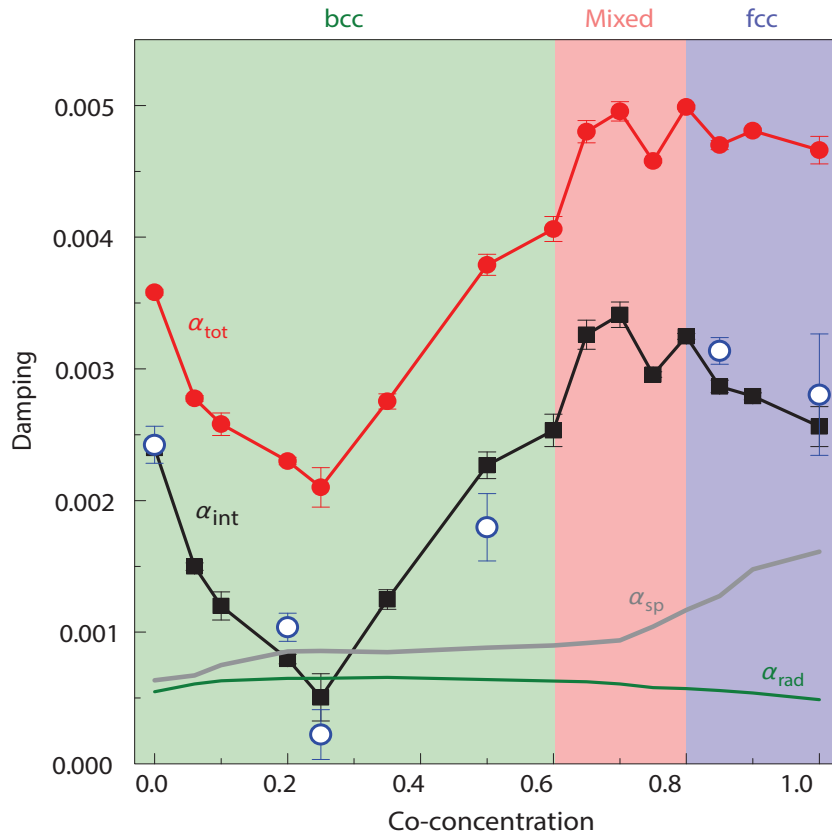


**Figure 2.1:** Measured damping of the thin films of CoFe alloys with radiative and interfacial, i.e., spin pumping, contributions. The internal damping is calculated by  $\alpha_{int} = \alpha_{tot} - \alpha_{rad} - \alpha_{sp}$ . The blue circles are  $\alpha_{int}$  values extrapolated from thickness variations of the thin films with a fixed Co-concentration. Adapted from Schoen *et al.* [8].

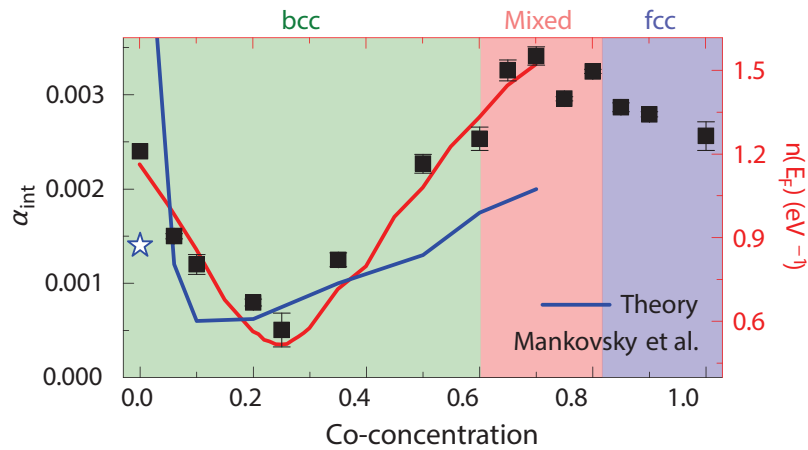


**Figure 2.2:** The internal damping parameter for the different Co-concentrations is compared to Mankovsky's theory [11] at 0K. The star denotes the expected value for pure Fe at 300K. On the right axis, the density of states of the Fermi-energy determined from theoretical calculations is plotted, matching the damping closely. Adapted from Schoen *et al.* [8].

## 2.1 Magnetron Sputter Deposition of $\text{Co}_{25}\text{Fe}_{75}$

All investigated  $\text{Co}_{25}\text{Fe}_{75}$  thin film samples were sputter deposited onto a Si (001) substrate<sup>1</sup> with a  $1\ \mu\text{m}$  thick thermally grown  $\text{SiO}_2$  layer on top using the new SUPERBOWL ultra-high vacuum (UHV) sputtering machine. The basic principle of sputtering incorporates accelerating positively charged ions towards a high purity target material, which then cause a collision cascade in the target. Due to the collisions, secondary electrons and surface atoms or, sometimes but less likely, small clusters of atoms [18] are eventually leaving the target. These atoms are then adsorbed on a substrate positioned above the target. A schematic of this process can be seen in Fig. 2.3 a). There are several ways to realize this kind of physical vapor deposition, such as ion-beam sputtering, reactive sputtering, gas flow sputtering and some more. In this work a dc-magnetron-sputtering method is used.

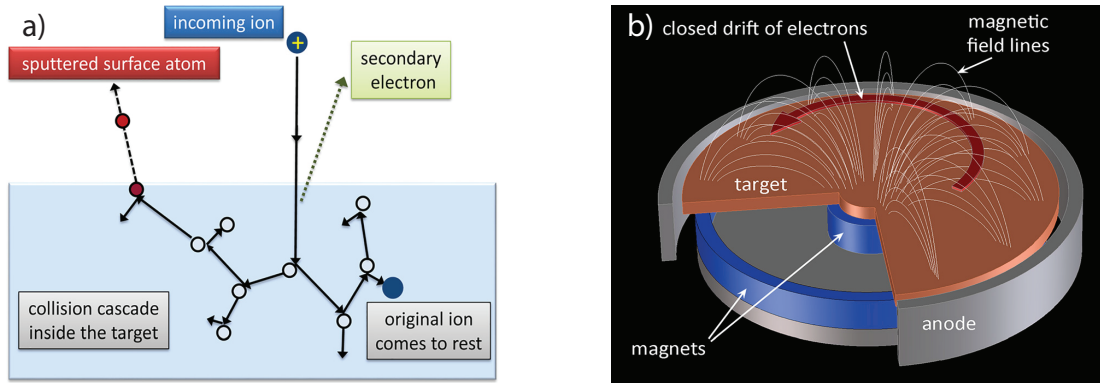


**Figure 2.3:** a) Schematic sketch of the collision process. Incident ions cause a collision cascade inside the target material rendering the sputtering of atoms and the formation of secondary electrons. b) Illustration of the magnetron setup. The target material shown in copper-color works as a cathode whereas the outer ring forms the anode. Magnets are used to implement a magnetic trap for the electrons causing them to drift in circular motion above the target, ionizing additional gas atoms.

One of the important parameters for sputter deposition is the sputtering yield

$$Y = N_a/N_i \quad (2.1)$$

which is the ratio of the numbers of sputtered atoms  $N_a$  and of the incident ions  $N_i$ . From Yamamura's data table compilation [19] one can see that its maximum lies between 10 keV and 100 keV of kinetic energy of the incident ions, but in real applications the kinetic energy  $E_i$  ranges from 300 eV to 3 keV. The sputtering yield varies for different materials as it's not only dependent on the ion's mass and energy, but is also sensitive to the composition and structure of the target [20].

While  $E_i$  is controlled by the applied bias voltage, the kinetic energy distribution for the sputtered atoms can be described by the following Thompson energy distribution [21]:

<sup>1</sup>Except for two samples grown on MgO.

$$f_{\text{Thompson}}(E) = \begin{cases} A \frac{E^{[1-\sqrt{(E_{\text{SB}}+E)/\Lambda E_i}]}}{(E+E_{\text{SB}})^3} & \text{if } 0 \leq E \leq \Lambda E_i \\ 0 & \text{if } E > \Lambda E_i. \end{cases} \quad (2.2)$$

Here,  $A$  is a normalization factor,  $E_{\text{SB}}$  is the surface binding energy of the target material and

$$\Lambda = \frac{4M_i M_a}{(M_i + M_a)^2} \quad (2.3)$$

is the known energy transfer factor for elastic scattering, where  $M_{a,i}$  is the mass of the respective particle. As this distribution is primarily dependent on the surface binding energy, it varies for different materials [22] and its proportionality can be written as

$$f_{\text{Thompson}} \propto \frac{E}{(E + E_{\text{SB}})^3}. \quad (2.4)$$

Its peak is found at  $E = E_{\text{SB}}/2$ . Atoms in the vicinity of the peak still have a kinetic energy of several eV resulting in rather high velocities

$$v_a \approx \sqrt{\frac{E_{\text{SB}}}{M_a}}. \quad (2.5)$$

A rough estimation of the velocity for Co and Fe atoms from their respective target material results in high velocities of  $v_{\text{Co}} \approx 2680 \frac{\text{m}}{\text{s}}$  and  $v_{\text{Fe}} \approx 2820 \frac{\text{m}}{\text{s}}$  ( $E_{\text{SB,Co}} = 4.39 \text{ eV}$ ,  $E_{\text{SB,Fe}} = 4.28 \text{ eV}$ ,  $M_{\text{Co}} = 58.9 \text{ u}$ ,  $M_{\text{Fe}} = 55.8 \text{ u}$ ) [19] (the derivation was adapted from Ref. [20]). The substrate to be coated is at a distance of a few centimeters from the target, which allows the atoms to reach its destination in a couple of microseconds. This is desirable, as ionization and chemical reaction of the sputtered atoms become less likely.

Another favored process parameter is a low deposition pressure, allowing the removed material to travel further without collision. Apparently, this requires a gas pressure, which yields a mean free path, which is larger than the distance to be traveled from target to substrate or at least comparable to it. A low pressure on the other hand leads to a lower density of gas atoms that can be ionized, reducing the total amount of sputtered material and thus the deposition rate. This adversity is solved by using the magnetron sputtering technique. It renders an efficient way of harvesting the available electrons for ionization of the sputter gas atoms.

For magnetron sputtering, magnetic fields are used to trap electrons in a helical motion, thus increasing their path to the anode significantly. A schematic illustration of a magnetron can be seen in Fig. 2.3b). Without magnetic field, secondary electrons spawned from the collisions in the target are directly accelerated by the electric field towards the positively charged anode. On their way they collide with gas atoms creating a plasma of ions and further electrons. By smartly implementing a magnetic trap, electrons drift in a circular motion and hence undergo more collisions. Scattering on slower electrons may activate those to produce further plasma, whereas hitting gas atoms directly creates the desired ions [20]. In Fig. 2.4a) the photograph of a used  $\text{Co}_{25}\text{Fe}_{75}$  target in a magnetron shows circular grinding spots, that indicate where the electrons circulated.



**Figure 2.4:** a) Used  $\text{Co}_{25}\text{Fe}_{75}$  target after several deposition runs and removal from the magnetron. The circular grinding of the material indicates where the electrons were kept gyrating by the magnetic fields. The diameter of the target is 50.8 mm. b) Inside of the SP4 chamber, 8 magnetrons are placed in two deposition clusters for complex multilayer deposition. Both, face-to-face and confocal sputtering is possible with this setup.<sup>2</sup>

Figure 2.4 b) shows the open SP4 chamber of the SUPERBOWL UHV sputtering cluster. The 8 tilt-able magnetrons are positioned in two clusters of four each, thus enabling simultaneous sputtering from up to four targets in a confocal adjustment. Two targets out of each cluster can also be used for direct, face-to-face sputtering of single material deposition. Each magnetron has its own power source, where six are connected to dc-sources (for metallic targets) and two are equipped with a rf-source, enabling sputter deposition of electrically insulating and semiconducting materials. The chamber's base pressure is  $< 5 \times 10^{-9}$  mbar. During sputter deposition, an Argon gas atmosphere with a pressure of a few  $10^{-3}$  mbar was maintained.

For sample loading and unloading into the deposition chamber a load-lock (LL) is attached to the deposition chamber via a pneumatic gate valve. The LL can be vented and evacuated significantly faster than the chambers due to its small size. With a magnetic transfer rod the sample can be placed on the three axes substrate manipulator in the chamber. Once the sample is installed, the manipulator is controlled via BESTEC<sup>TM</sup>-software to move it over the desired magnetrons and the target to substrate distance can be adjusted for deposition rate control. The sample can also be rotated with up to 30 rpm to avoid planar anisotropies in the thin films.

A motorized linear moving substrate shutter (wedge shutter) protects the substrate from unwanted contamination and also allows wedge structured deposition. Another feature of the system is the sample heating stage, which allows heating the substrate to a maximum temperature of  $700^\circ\text{C}$ . Both additional features, wedge structuring and heating, were not used during this work, i. e., sputtering was always performed on the whole substrate at room temperature<sup>3</sup>.

In order to control the deposition rate, a quartz-crystal (QC) micro balance is installed

<sup>2</sup>Credit: Matthias Althammer

<sup>3</sup>except for one of the MgO-substrate samples, see Table A.1.

on the sample manipulator. The crystal's resonance frequency  $f_{\text{res}}$  is measured during deposition and due to the mass change  $f_{\text{res}}$  shifts. Knowing the density of the applied material and assuming homogeneous coating one can then calculate the deposited thickness and deposition rate. That way, the required time for a desired material thickness growth can be estimated in-situ. For small process times, this approach is not always accurate, as adsorption conditions at the substrate may be different to those from the QC. Due to this fact, additional measurements using X-ray reflectometry were performed to verify material layer thicknesses of almost all samples.

## 2.2 X-Ray Reflectometry

Elastic, high energy photon scattering on thin films, (X-ray diffraction (XRD) in this case), is a well understood and a widespread measurement technique to extract layer thicknesses, layer roughness and crystallographic geometries [23–29]. It consists of the grazing incidence diffraction of light from the surface of a sample or even different layer interfaces on a thin film sample. A very fast and intuitive approach is Bragg's condition for constructive interference

$$2d \sin(\theta) = n\lambda, \quad (2.6)$$

where  $d$  is the separation of the interfaces,  $\theta$  is the angle of the incoming light with respect to the surface plane,  $n$  is a positive integer and  $\lambda$  represents the wavelength. The idea of this measurement technique is that different beams reflected on different interfaces interfere constructively or destructively. From the intensity of the reflected light depending on the angle one can then reconstruct the layer compositions.

Even though the idea appears to be rather simple, fitting real data can get very intricate when it comes to multilayer samples and layer thicknesses of only a few nanometers. The fabricated samples were characterized using XRD and the obtained data was fitted with the Leptos© fitting software. As the standard Levenberg-Marquardt algorithm only finds a local optimum, logarithmic simulated annealing was used to gain more robust results. It was shown that its probability to find the global optimum approaches 1, for long enough computing time [30]. Nonetheless, it requires an accurate implementation of material layers within the stack, which is not always a trivial task.

Most samples fabricated for FMR-measurements either consist of 3 or 5 layers of material. In any case, the implementation of the simulation demands inclusion of oxidated layers. Depending on the materials, also interlayer mixing of material needs to be taken into account. Subsequently, 4 to 7 parameters had to be fitted simultaneously for one sample, which means that an exact determination of the layer thicknesses in this work is rather complex and an error of 10% for the extracted thicknesses is assumed for the results. Additionally considering different layer roughnesses would double the amount of parameters to be fitted and was avoided for that reason. In Fig. 2.5 the reflectometry data of the investigated sample "Terminal 001" (see Table A.1 and B.2) is shown. The simulation clearly does not match the data perfectly, but it is a rather good fit. The actual requested

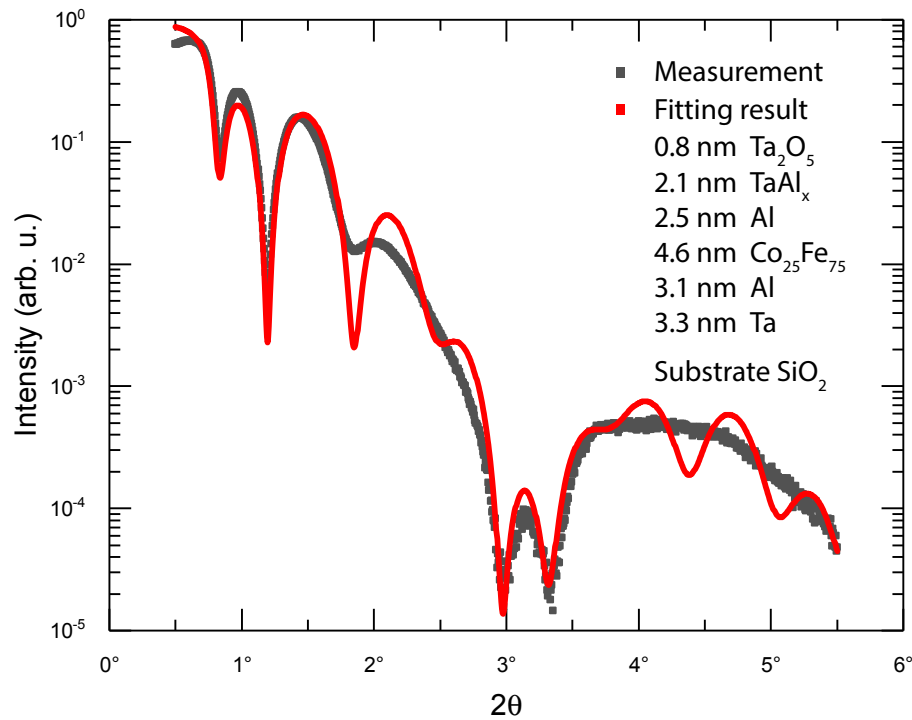


**Figure 2.5:** XRD-reflectometry of the sample "Terminal 001". The obtained thicknesses have an uncertainty of approximately 10%. The time controlled sputter deposition aimed at a multilayer containing 3nm Ta / 3nm Al / 5nm  $\text{Co}_{25}\text{Fe}_{75}$  / 3nm Al / 3nm Ta.

deposition thicknesses calculated from the deposition time and deposition rate were: 3nm Ta / 3nm Al / 5nm  $\text{Co}_{25}\text{Fe}_{75}$  / 3nm Al / 3nm Ta.

Only samples which were sputtered as a blanket film (no patterning) were probed with this technique. In addition to these samples, we also fabricated structured samples with dimensions in the micrometer regime by optical lithography for Brillouin light scattering experiments as discussed in the following.

## 2.3 Micropatterning by Optical Lithography

For the fabrication of structured multilayer samples for optical measurements in this thesis, via photolithography, the direct laser-writing tool PicoMaster 200 was used. As one of the first users of this new device, we had to develop a proper lithography process, as usage of the machine turned out to be rather delicate. In this section, we will shortly discuss the photolithography and the lift-off process and the used fabrication recipe. Afterwards, the PicoMaster 200 and its features will be introduced. In appendix C and D, some workarounds to frequently appearing issues and a sample list containing the relevant photolithography parameters are presented, respectively.

Photolithography is a commonly used structuring method allowing both, top-down and bottom-up structuring techniques [31–40]. In this work, lift-off was used exclusively for

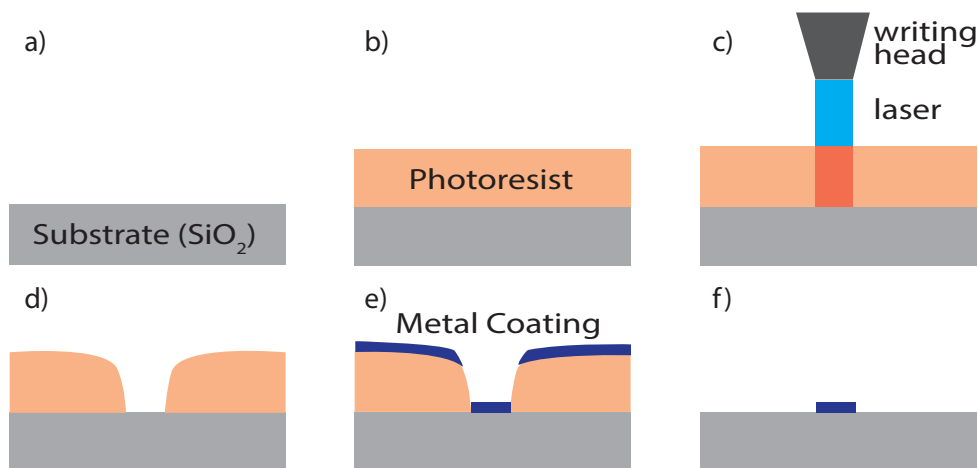


**Figure 2.6:** Process steps of a common lift-off process. a) substrate cleaning and pretreatment b) dispersion of photoresist, e. g., by spin coating and soft baking afterwards c) light exposure with a laser writing the desired structure d) development of the sample e) material deposition f) lift-off process by dissolving the resist with, e. g., acetone.

pattern definition. A simple illustration of the employed process is represented in Fig. 2.6. As a first step, the substrate is cleansed by Acetone in an ultra-sonic bath. To get rid of the protective varnish on top of a new substrate, it is sufficient to place it in an ultra-sonic bath set to the highest power in Acetone for 3 min. Afterwards, this step is repeated with Isopropanol and samples are dried immediately afterwards with a N<sub>2</sub>-gun. A photoresist (AZ® 5214 E in this case) is dispensed homogeneously on the sample using a spin coater. For that purpose, the substrate is stabilized on the coater by a vacuum pump. In case of using samples which were cleansed long before the coating it is recommended to use the N<sub>2</sub>-gun again in order to get rid of possible dust particles. For the next step, it is crucial to initialize the coater before dispensing the resist on top of the substrate. In that way, the spin-coater starts directly with the acceleration ramp after closing the cover. The resist can be poured on the sample surface using a micro pipette filled at least with 120 µl of resist. The creation of bubbles should be avoided and the the cap of the coater has to be closed immediately in order to start the spinning process. The time between applying the resist and starting the spin coating process should not exceed 2 s. Otherwise, too much solvent evaporates from the resists, which impedes a homogeneous coating on the substrate surface, necessary for the laser writer to catch focus over the whole sample dimensions. During the spin coating process, the substrate spins at 500 rpm for 3 s and then accelerates to 5000 rpm and maintains this rotation speed for 60 s. A softbake step at 110°C for 70 s removes the remaining amount of solvent from the resist after the spin coating process. This step prevents foaming of the resist during exposure due to N<sub>2</sub> creation. Moreover, the softbake minimizes dark erosion and improves resist adhesion to the substrate [41]. Residual resist on the back of the sample after spin coating can be carefully removed by a cotton bud moistened with Acetone. This step is necessary to reduce substrate tilting when mounting the sample in the laser writer and to allow for fixation by vacuum. A laser with a wavelength of 405 nm then is scanned across the surface of the sample and

writes the desired pattern into the resist by light exposure. The exposed area is later then dissolved in the developer. The laser exposure dose has to be chosen carefully. Too high doses adversely affect the resolution, whereas too low doses induce higher development times, hence amplifying dark erosion effects [42]. We thus optimized the used exposure dose systematically. For the described spin coating process a suitable dose of 175-180 mJ/cm<sup>2</sup> was found. When the writing process is finished, the sample is placed into an appropriate developer, dissolving the exposed resist. Dark erosion chamfers the edges of the photoresist as also non-exposed resist is attacked in small amounts as depicted in Fig. 2.6 d). For the given recipe, the sample is placed in AZ® 726 MIF developer for 55 s. In a fifth step, the metal coating can be deposited by different techniques. In our case, the aforementioned sputtering technique is used. Afterwards, lift-off is performed in a solvent e. g. Acetone, which dissolves the resist and hence lifts off the metal coating on top. For our samples it was performed in acetone for 3 min in an ultra-sonic bath set to the lowest intensity. Ideally, only material deposited directly on the substrate remains. This defines the pattern on the sample. The optimized recipe for sample fabrication can still be improved for better resolution, but already yields a sufficiently high success rate concerning the focus issue.

The PicoMaster 200 basically consists of a writing module and a substrate holder. The writing module can be seen in Fig. 2.7 a). The arrows in the picture show the location of the camera and the main laser, using illumination from a green LED and blue laser, respectively. Using the alignment camera the position and orientation of the sample can be calculated based on the markers on the substrate. If no markers are placed on the substrate its position can either be found automatically or manually using the camera and the edges of the sample. Its pixel resolution is of 1 μm and due to the Cognex Patmax algorithm leads to a final alignment accuracy of <0.5 μm. The installed writing module has a 405 nm wavelength GaN laser diode, which can also be replaced by a, e. g., 375 nm wavelength module. Additionally, a 650 nm wavelength red laser for the autofocus system is integrated, enabling correction of height variations during the writing process. The substrate holder accommodates substrate sizes from 5 × 5 mm<sup>2</sup> up to 220 × 220 mm<sup>2</sup>, which are mounted onto a vacuum chuck. The laser writer is equipped with high precision linear motors in X (step axis) and Y (scan axis) direction and also includes a motorized controlled Z-axis to account for substrate thickness variation.

For the photolithography process, the sample is placed on the substrate holder and held in place by the vacuum holes. The location of the substrate in coordinate system of the machine has then to be determined. For the automatic position detection, its rough position has to be known. Using the red laser focus detection, the system then searches for the edges of the sample on each of the four sides and calculates its dimensions and position. A manual alignment is performed by using the microscope camera and centering the top left corner of the substrate in the camera image. This position can then be transferred to the setup parameters. The exact substrate dimensions have to be known for this alignment option. If the substrate has already alignment markers on the surface, the software utilizes image recognition for the markers and determines the sample position from this recognition process. In the setup of the system one has to define the desired exposure dose and spot parameters (i. e., resolution and attenuation). Before starting the writing process a manual

focus check can be performed. In this step, the sample is placed below the writing module and with the red focus laser one can check whether a stable focus condition for the whole writing area of the lithography process can be found. A homogeneous resist distribution is required for a successful exposure. Hence, the optimization process of the lithography steps included not only the exposure dose, but also the spin-coating parameters like, e. g., the rotation speed. A sample list with all fabrication parameters used for the optimization is presented in appendix D.

In Fig. 2.7b) a dose test is depicted. Several dumbbell structures with different dose were written into the resist on a Si substrate. In this micrograph image the developed resist pattern is shown. Figure 2.7c) is an example of a finished sample, fabricated by the described photolithography and sputtering deposition processes. Markers were used for the alignment in the different deposition steps, which cannot be seen in the image. The sample contains a  $\text{Co}_{25}\text{Fe}_{75}$  multilayer strip and a microwave Al-antenna. Both are connected to some Al-contact pads.

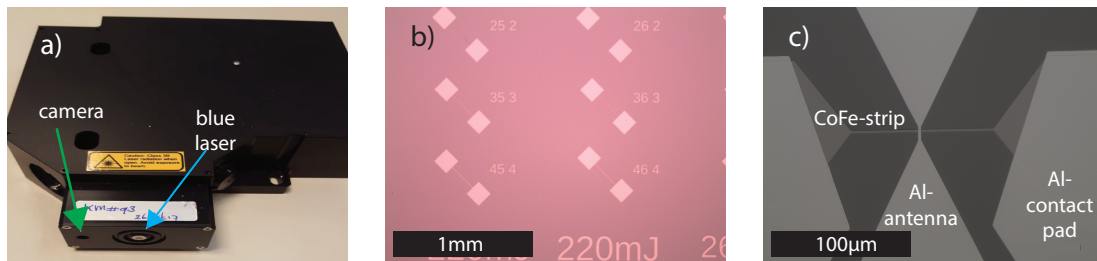


**Figure 2.7:** a) PicoMaster writing module with its green LED camera and the blue writing laser. b) Several dumbbell test structures written for a dose test. The picture only depicts developed resist. c) Finished sample containing a  $\text{Co}_{25}\text{Fe}_{75}$  multilayer strip, aluminum microwave antenna and electrical contact pads for both.

# Chapter 3

## Broadband Experiments - Magnetic Damping in $\text{Co}_{25}\text{Fe}_{75}$

### 3.1 Ferromagnetic Resonance

The resonant absorption of electromagnetic waves in a magnetic material is an invaluable measurement technique to obtain a broad spectrum of magnetic properties such as, e. g., the dispersion relation (in this case it is frequency vs. field), anisotropies and damping [43–49]. It is a commonly used method and can be realized in different ways, either with microwave resonant cavities or with coplanar waveguides (CPW) [50]. In this work a large number of samples was investigated, which made an easy sample exchange necessary. Also the damping was measured, which demands measurement in a broad range of frequencies. Cavities restrict the measurement to a single frequency (and higher modes). Hence, the CPW method is the favorable option and was consequently used for the FMR study.

Ferromagnetic materials exhibit a parallel ordering of their magnetic momenta below the critical Curie temperature  $T_C$  [51]. For  $\text{Co}_x\text{Fe}_{1-x}$  alloys  $T_C$  is found to exceed 1000 K [52], such that room temperature experiments satisfy the need of a macroscopic magnetization vector in our samples. Applying an external field will lead to a reorientation of the magnetization vector. If the applied field overcomes the demagnetizing field parallel alignment of the two vectors can be assumed. In real samples, anisotropies and demagnetization have to be considered leading to an effective field

$$\mathbf{H}_{\text{eff}} = \mathbf{H}_{\text{ext}} + \mathbf{H}_{\text{aniso}} - \mathbf{H}_{\text{demag}}, \quad (3.1)$$

which contains the applied, external field  $\mathbf{H}_{\text{ext}}$ , the anisotropy contribution  $\mathbf{H}_{\text{aniso}}$  and the demagnetization field in the sample  $\mathbf{H}_{\text{demag}}$ . In thermal equilibrium, the magnetization vector will always be aligned parallel to  $\mathbf{H}_{\text{eff}}$ . It is crucial to understand that the magnetization vector behaves like an angular momentum vector, such that by perturbing the system, i. e., creating a non-zero angle between the magnetization and the effective field a precession is initiated (see Fig. 3.1). This dynamic motion is described by

$$\frac{d\mathbf{m}}{dt} = -\gamma \mathbf{m} \times \mu_0 \mathbf{H}_{\text{eff}}. \quad (3.2)$$

with a resulting precession frequency

$$\omega = \gamma\mu_0|H_{\text{eff}}| \quad (3.3)$$

of the resonance. Here,  $\gamma = g\mu_B/\hbar$  represents the gyromagnetic ratio with the Landè-factor  $g$ , the Bohr magneton  $\mu_B$  and the reduced Planck constant  $\hbar$ ,  $\mathbf{m}$  is the normalized magnetization vector  $\mathbf{m} = \mathbf{M}/M_{\text{sat}}$  with the saturation magnetization  $M_{\text{sat}}$  and  $\mu_0 = 4\pi \times 10^{-7} \text{ Vs}/(\text{A m})$  the vacuum permeability. Deriving the more accurate relation between the angular frequency and the applied field  $H_{\text{ext}}$  requires consideration of magnetic anisotropies, which is discussed later on. Equation (3.2) is the so called Landau-Lifshitz equation, which was first worked out in 1935 [53]. As the magnetization will not precess endlessly, a "damping"-term is needed. Viscous damping of the magnetization was described in a convenient notation by Gilbert in 2004 [54]. His phenomenological description

$$\frac{d\mathbf{m}}{dt} = -\gamma\mathbf{m} \times \mu_0\mathbf{H}_{\text{eff}} + \alpha\mathbf{m} \times \frac{d\mathbf{m}}{dt} \quad (3.4)$$

is now known as the Landau-Lifshitz-Gilbert (LLG)-equation, where  $\alpha$  is referred to as the Gilbert-damping parameter. The described dynamic motion is illustrated in Fig. 3.1.

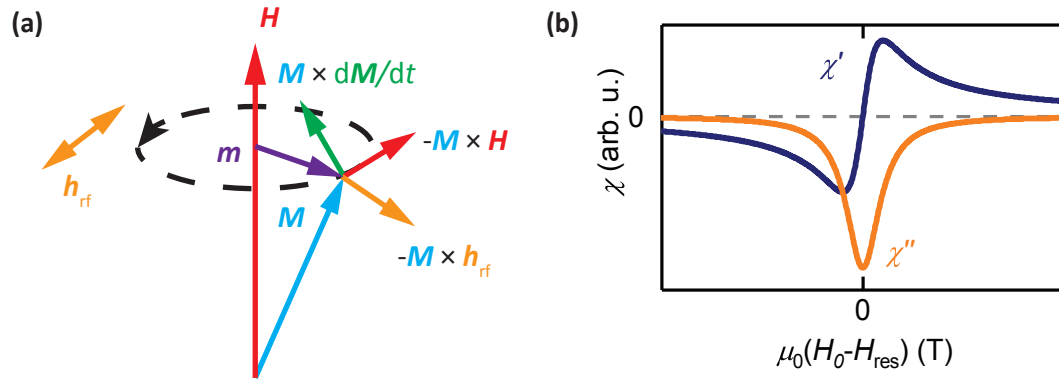


**Figure 3.1:** a) Precessional motion of a magnetization vector around an applied effective field described by the LLG-equation.  $\mathbf{H}$  creates a torque  $-\mathbf{M} \times \mathbf{H}$  (red) on  $\mathbf{M}$  resulting in a circular motion. The damping-like term  $\mathbf{M} \times d\mathbf{M}/dt$  (green) drags  $\mathbf{M}$  back into parallel alignment. When a superimposed, perpendicular rf-field  $\mathbf{h}_{\text{rf}}$  hits the resonance frequency the system absorbs energy from the electromagnetic wave driving the oscillation (orange). b) The magnetic response function, i. e., the high frequency susceptibility  $\chi$  depending on the applied field  $\mathbf{H}$ .  $\chi'$  represents the real part, whereas  $\chi''$  stands for the imaginary part. This function relates the vector  $\mathbf{m}$  in a) with  $\mathbf{h}_{\text{rf}}$  by the equation  $M_{\text{sat}}\mathbf{m} = \chi\mathbf{h}_{\text{rf}}$ .<sup>1</sup>

When an oscillatory field perpendicular to  $\mathbf{H}_{\text{eff}}$  is applied, the magnetization vector is forced into a precessional motion. The additional torque  $-\mathbf{M} \times \mathbf{h}_{\text{rf}}$  imposed by  $\mathbf{h}_{\text{rf}}$  leads to an endless precession. The absorbed energy becomes highest when the resonance condition is met. The imaginary part seen in Fig. 3.1 b) of the susceptibility reflects this absorbed energy. The relation between frequency and applied external field was described by Kittel in 1948 [56] and is known as the Kittel equation. It's derivation will be roughly sketched in

<sup>1</sup>Illustrations taken from the master thesis of Lukas Liensberger [55].

the following.

We define a coordinate system with base vectors  $\mathbf{e}_1, \mathbf{e}_2$  and  $\mathbf{e}_3$ , where the static external field  $\mathbf{H}_{\text{eff}}$  points in the  $\mathbf{e}_3$  direction. By assuming an ellipsoidal geometry for our sample and letting its main axes point parallel to our defined coordinate system, the later occurring demagnetization tensor  $\mathbf{N}$  is diagonalized. The same assumption applies to the anisotropy tensor  $\mathbf{K}$ . Let the rf-field oscillate in the 1,2-plane such that the effective field and the magnetization can be written as:

$$\begin{aligned}\mathbf{H}_{\text{eff}} &= \mathbf{H}_{\text{ext}} - \mathbf{K}\mathbf{H}_{\text{aniso}} - \mathbf{N}\mathbf{M}_{\text{sat}} + \mathbf{h}_{\text{rf}}(t) \\ \mathbf{m} &= 1 \cdot \hat{\mathbf{e}}_3 + \mathbf{m}(t).\end{aligned}\quad (3.5)$$

Here,  $\mathbf{H}_{\text{aniso}}$  and  $\mathbf{M}_{\text{sat}}$  are vectors with its respective value  $H_{\text{aniso}}$  and  $M_{\text{sat}}$  in every of its entries. We use the ansatz, where  $\mathbf{h}_{\text{rf}}(t) = \exp(i\omega t)(h_{\text{rf},1}\mathbf{e}_1 + h_{\text{rf},2}\mathbf{e}_2)$  and  $\mathbf{m}(t) = \exp(i\omega t)(m_1\mathbf{e}_1 + m_2\mathbf{e}_2)$  and plug it into the LLG (3.4). By taking into account only the first order of  $m$ , we can focus on the first two components and solve by  $h_1$  and  $h_2$ , which results in a equation of the form:

$$\begin{pmatrix} h_1 \\ h_2 \end{pmatrix} = \overset{\leftrightarrow}{\chi}_{\text{P}}^{-1} \begin{pmatrix} m_1 \\ m_2 \end{pmatrix}.\quad (3.6)$$

Inverting the matrix  $\overset{\leftrightarrow}{\chi}_{\text{P}}^{-1}$  and multiplying  $M_{\text{sat}}$  for the right dimensions returns the Polder susceptibility, presented in (3.7), which was first derived in 1949 [57]:

$$\overset{\leftrightarrow}{\chi}_{\text{P}} = \frac{M_{\text{sat}}}{\text{Det}(\overset{\leftrightarrow}{\chi}_{\text{P}}^{-1})} \begin{pmatrix} A_{11} + \frac{i\omega\alpha}{\gamma\mu_0} & + \frac{i\omega}{\gamma\mu_0} \\ -\frac{i\omega}{\gamma\mu_0} & A_{22} + \frac{i\omega\alpha}{\gamma\mu_0} \end{pmatrix},\quad (3.7)$$

with

$$\begin{aligned}A_{11} &= H_{\text{ext}} + H_{\text{aniso}}(K_2 - K_3) + M_{\text{sat}}(N_2 - N_3) \\ A_{22} &= H_{\text{ext}} + H_{\text{aniso}}(K_1 - K_3) + M_{\text{sat}}(N_1 - N_3)\end{aligned}\quad (3.8)$$

such that

$$\begin{pmatrix} M_1 \\ M_2 \end{pmatrix} = \overset{\leftrightarrow}{\chi}_{\text{P}} \begin{pmatrix} h_1 \\ h_2 \end{pmatrix}.\quad (3.9)$$

It has to be mentioned, that the actual  $\overset{\leftrightarrow}{\chi}$  is a  $3 \times 3$  matrix, but all additional entries to those in Eq. (3.7) are zero. In the divergent case  $\text{Det}(\overset{\leftrightarrow}{\chi}_{\text{P}}^{-1}) = 0$  the resonance condition is met. By solving this condition and taking the real part, we obtain the resonance field:

$$\begin{aligned}H_{\text{res}} &= -\frac{1}{2}H_{\text{aniso}}(K_1 + K_2 - 2K_3) - \frac{1}{2}M_{\text{sat}}(N_1 + N_2 - 2N_3) + \\ &\quad \sqrt{\frac{h^2}{(\gamma\mu_0\mu_{\text{B}})^2}f^2 + (H_{\text{aniso}}(K_1 - K_2) + M_{\text{sat}}(N_1 - N_2))^2}\end{aligned}\quad (3.10)$$

with  $f = \omega/(2\pi)$ .

A detailed derivation can be found in [58–62]. Equation (3.10) describes the resonance condition for an ellipsoidal sample shape. It can be simplified for an infinitely extend thin film. Assuming that the film normal points into the z-direction the demagnetization tensor entries are  $N_x = 0, N_y = 0, N_z = 1$ . By neglecting in plane anisotropies and only considering the out of plane component, the same applies for the anisotropy tensor  $\mathbf{K}$ . We can distinguish two cases:

The in plane case (IP), where  $\mathbf{H}_{\text{eff}}$  is in the film plane ( $\mathbf{e}_x = \mathbf{e}_3, \mathbf{e}_y = \mathbf{e}_1, \mathbf{e}_z = \mathbf{e}_2$ ) and the out of plane case (OOP), where  $\mathbf{H}_{\text{eff}}$  points out of the FM plane ( $\mathbf{e}_x = \mathbf{e}_1, \mathbf{e}_y = \mathbf{e}_2, \mathbf{e}_z = \mathbf{e}_3$ ). In the first case, this leads to the IP-Kittel equation for thin films:

$$H_{\text{res}} = \sqrt{\frac{h^2}{(\gamma\mu_0\mu_B)^2} f^2 + \left(\frac{H_{\text{aniso}} + M_{\text{sat}}}{2}\right)^2} - \left(\frac{H_{\text{aniso}} + M_{\text{sat}}}{2}\right). \quad (3.11)$$

As we cannot distinguish between  $H_{\text{aniso}}$  and  $M_{\text{sat}}$  an effective magnetization  $M_{\text{eff}} = H_{\text{aniso}} + M_{\text{sat}}$  is introduced. For the second case (OOP), the resulting OOP-Kittel equation for thin films looks as follows:

$$H_{\text{res}} = M_{\text{eff}} + \frac{h}{(\gamma\mu_0\mu_B)} f. \quad (3.12)$$

When taking the imaginary part of the solution obtained from  $\text{Det}(\overset{\leftrightarrow}{\chi}^{-1}) \stackrel{!}{=} 0$  one can get insight into the damping by the linewidth:

$$\Delta H_{\text{HWHM}} = \frac{\alpha \omega}{\mu_0 \gamma}. \quad (3.13)$$

Thus one can calculate the phenomenological damping parameter  $\alpha$ , which accounts for every damping process which scales linearly with the frequency. Our fitting program takes the full-width-half-maximum value, such that a factor of two has to be multiplied to  $H_{\text{HWHM}}$ . Additionally an offset  $H_{\text{inh}}$  has to be taken into account as a finite y-intersect is found in our measurements. The final fitting function

$$\mu_0 \Delta H_{\text{FWHM}} = \mu_0 H_{\text{inh}} + 2 \cdot \frac{2\pi f \alpha}{\gamma} \quad (3.14)$$

is used to extract the Gilbert-damping for the samples and the offset  $H_{\text{inh}}$  can be taken as a rough indication for the sample's quality. For a perfect sample, the intersect should cross the origin, whereas inhomogeneities lead to broader linewidths. In addition to film inhomogeneities,  $H_{\text{inh}}$  can also be caused by any intrinsic relaxation process that is independent of frequency.

## 3.2 Spin Pumping

Considering our thin film heterostructure samples, an additional contribution to the intrinsic Gilbert-alpha of the ferromagnetic material has to be taken into account. Tserkovnyak and Brataas were the first to propose spin pumping as a mechanism for Gilbert damping in

normal-metal/FM heterostructures [63]. They found that the precession of the magnetization results in spin current injection into the normal metal. In turn, this transport of spin angular momentum from FM to NM relaxes the oscillatory motion of the magnetization, thus acting as an additional damping term. [63–71]. In 2004, Brataas, Tserkovnyak and Bauer [65] found the corresponding spin current at the interface to be

$$\mathbf{I}_s \approx \frac{\hbar}{4\pi} g_{\uparrow\downarrow} \mathbf{m} \times \frac{d\mathbf{m}}{dt}. \quad (3.15)$$

Note that we here only consider the real part of the spin mixing conductance  $g_{\uparrow\downarrow}$ , which is responsible for the enhancement of the Gilbert damping. The imaginary part of  $g_{\uparrow\downarrow}$  is generally much smaller and does not modify the magnetic damping. It is thus disregarded within this thesis. By comparison with the known LLG equation (3.4) one finds that the spin current in Eq. (3.15) leads to an enhancement of alpha with  $\alpha = \alpha_0 + \alpha_{\text{SP}}$ . Here,  $\alpha_0$  is the intrinsic Gilbert-alpha and the second part due to spin pumping equals

$$\alpha_{\text{SP}} = \frac{\gamma \hbar g_{\text{eff}}^{\uparrow\downarrow}}{4\pi M_s d} \quad (3.16)$$

as shown in [65].  $M_s$  represents the magnetization and  $d$  the thickness of the FM. The effective spin mixing conductance is given by  $g_{\text{eff}}^{\uparrow\downarrow} = \eta g_{\uparrow\downarrow}$  where  $\eta$  is a parameter between zero and one, depending on the spin current backflow [72]. At the interface, some of the spin current can be reflected, reducing the net outflow. Hence, this factor accounts for the reduction of spin current loss.  $\eta$  depends on the used material, including the electrical conductivity of the adjacent layer. In ferromagnets the spin current is mainly transported via magnetization dynamics. In the non-ferromagnetic metallic adjacent layer the spin current is carried by flowing electrons, such that a higher electric conductivity facilitates the spin pumping effect. This is also described by Weiler *et al.* [72], where the spin current backflow is given by

$$\eta = \left( 1 + 2g_{\uparrow\downarrow} \rho_{\text{NM}} \lambda_{\text{SD}} \frac{e^2}{\hbar} \coth\left(\frac{d_{\text{NM}}}{\lambda_{\text{SD}}}\right) \right)^{-1}. \quad (3.17)$$

Here,  $\rho_{\text{NM}}$  is the resistivity of the NM,  $\lambda_{\text{SD}}$  is the spin diffusion length of the NM,  $\frac{e^2}{\hbar}$  is the inverse Klitzing constant and  $d_{\text{NM}}$  is the layer thickness of the NM. An illustration of the spin pumping process is shown in Fig. 3.2, where the magnetization precession pumps spin current into the normal-metal layer. In this work the effective spin mixing conductances are calculated by plotting the measured Gilbert-alphas over the sample's FM-thickness, analogously to Schoen's work [74].

### 3.3 Experimental Technique and Setup

For our broadband FMR (bbFMR) experiments, a vector network analyzer (VNA) was used. In contrast to a scalar network analyzer, a VNA allows not only to determine amplitude, but also phase information [75]. Here, we use transmission measurements, where a microwave

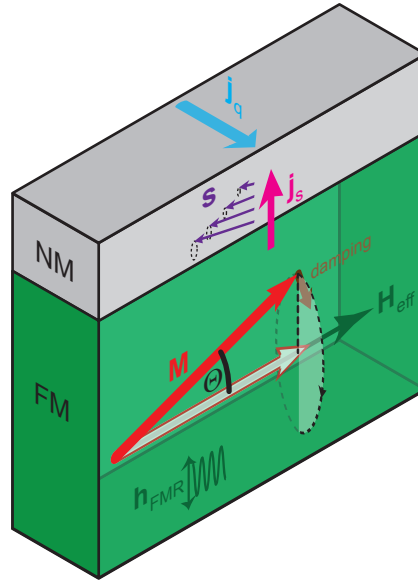


**Figure 3.2:** Illustration of the spin pumping mechanism. A driven magnetization vector (red) in a magnetically ordered material leaks spin angular momentum by pumping spin current (rosy) into the adjacent layer. This loss of momentum acts as a damping term to the precessional motion, increasing the Gilbert damping. Using material with high spin-Hall angles allows detection of transversal charge currents (blue). This schematic is taken from [73].

signal is generated at port 1 and detected at port 2. Our FMR setup consists of a small number of devices. It includes the external magnetic field source, the VNA itself and a coplanar waveguide (CPW). A schematic of the setup illustration can be seen in Fig. 3.3.

For the generation of the external static magnetic field an electromagnet was used. Depending on the geometry of the measurement (IP or OOP) the CPW was installed horizontally or vertically, respectively. The sample was simply placed on the CPW (IP) or additionally fixed with sticky tape (OOP). On both ends of the CPW, endlaunches are used to connect coaxial microwave cables which are then connected to port 1 and port 2 of the VNA.

The ac current through the center conductor (CC) induces the rf-magnetic field  $h_{\text{rf}}$  perpendicular to the external static field  $H_{\text{ext}}$ . As the CC is a thin strip the induced rf-field is approximately described by the Karlqvist equations calculated in 1954 [76]:

$$\begin{aligned} h_y(y,z) &= \frac{1}{\pi} h_0 \left( \arctan\left(\frac{y + w_{\text{cc}}/2}{z}\right) - \arctan\left(\frac{y - w_{\text{cc}}/2}{z}\right) \right) \\ h_z(y,z) &= \frac{1}{2\pi} h_0 \ln \left( \frac{(y + w_{\text{cc}}/2)^2 + z^2}{(y - w_{\text{cc}}/2)^2 + z^2} \right), \end{aligned} \quad (3.18)$$

where  $w_{\text{cc}}$  is the width of the CC and  $h_0$  is the field amplitude at  $(y,z) = (0,0)$  with  $h_0 = J_{\text{CPW}}/2 = I/2w_{\text{cc}}$ . For detection of the FMR, the relevant quantity is the induced

<sup>2</sup>Illustration adapted from Lukas Liensberger [55].

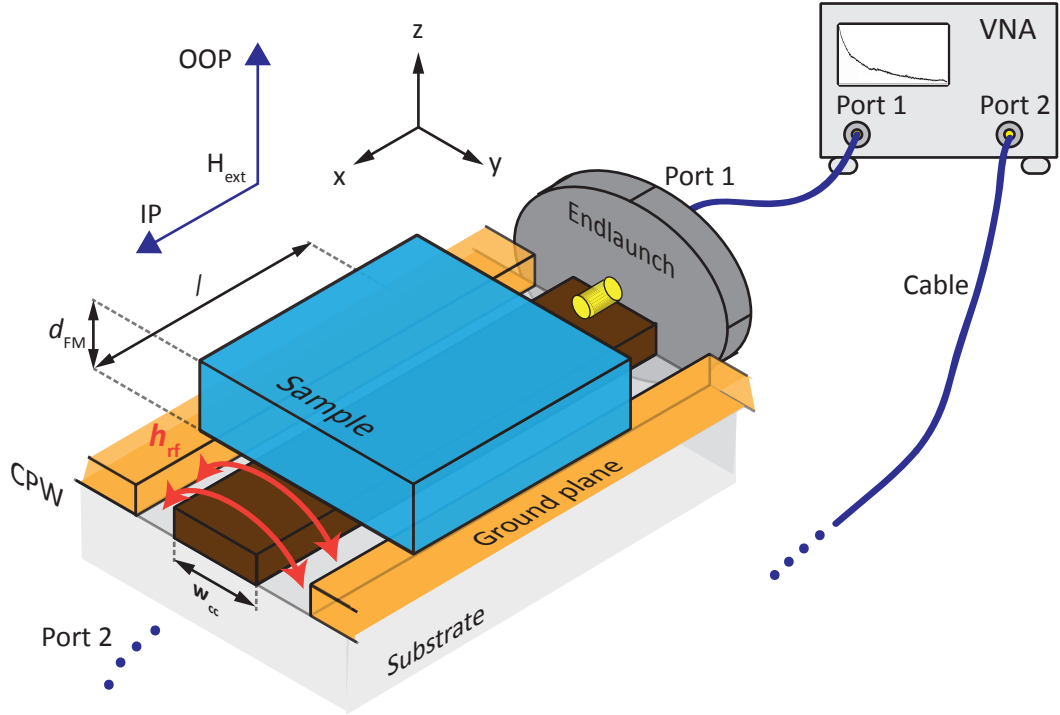


**Figure 3.3:** Sketch of the FMR setup. The CPW consists of a CC (brown) and two grounded planes (orange). This configuration corresponds to a coaxial cable in 2D. The endlaunches connect the CC with the high frequency cables installed at the ports from the VNA. The CPW is assembled in an electromagnet either in OOP or IP configuration. For the IP configuration it is important for the field lines to be parallel to the CC. The microwave signal from the VNA induces a radio-frequency magnetic field, which couples to the magnetization within the sample like indicated in 3.1 a)<sup>2</sup>.

voltage in the CPW by these dynamic fields:

$$V_{\text{ind}} = -\frac{\partial \Phi}{\partial t}. \quad (3.19)$$

Due to this formula, in this work, we can focus on the dynamic part of the flux  $\Phi$  only, which is given by

$$\begin{aligned} \Phi_{\text{dyn}} &= \frac{\mu_0}{I} \iiint_{\text{Volume}} \mathbf{h}(y,z) \cdot \vec{\chi} \cdot \mathbf{h}(y,z) dx dy dz \\ \Phi_{\text{dyn}} &= \frac{\mu_0}{I} \iiint_{\text{Volume}} \chi_{yy} h_y^2 + (\chi_{yz} + \chi_{zy}) h_y h_z + \chi_{zz} h_z^2 dx dy dz. \end{aligned} \quad (3.20)$$

Here,  $I$  stands for the current flowing through the CPW,  $\mathbf{h}(y,z)$  is the field described by Karlqvist (Eq. (3.18)) and  $h_y, h_z$  are its  $y$  and  $z$  component, respectively.  $\chi_{ij}$  are the respective entries in the susceptibility matrix. The middle term in the integral can be omitted due to symmetry reasons. We define the sample's dimensions  $d_{FM}$  for FM thickness,  $l$  for its length and  $b$  for its width. As  $d \ll w_{cc}$  we can take the limit  $h_{y,z}(y,0) = \lim_{z \rightarrow 0} h_{y,z}(y,z)$ .

Also, as  $b \gg w_{cc}$  we can approximate  $\int_{-b/2}^{b/2} h_{y,z}(y,z) dy$  by  $\int_{-\infty}^{\infty} h_{y,z}(y,z) dy$ . This leads to the result

$$\begin{aligned}\Phi_{\text{dyn}} &= \frac{\mu_0}{I} \cdot l \cdot d_{\text{FM}} \left( \chi_{yy} \int_{-\infty}^{\infty} h_y(y,0)^2 dy + \chi_{zz} \int_{-\infty}^{\infty} h_z(y,0)^2 dy \right) \\ &= \frac{\mu_0}{I} \cdot l \cdot d_{\text{FM}} \left( \chi_{yy} \frac{I^2}{4w_{cc}} + \chi_{zz} \frac{I^2}{4w_{cc}} \right) \\ &= \mu_0 I \frac{l \cdot d_{\text{FM}}}{4w_{cc}} (\chi_{yy} + \chi_{zz}).\end{aligned}\quad (3.21)$$

Using a harmonic ansatz  $I = I_0 \exp(-i\omega t)$  for the current through the CPW we obtain:

$$V_{\text{ind}} = i\mu_0\omega I_0 \frac{l \cdot d_{\text{FM}}}{4w_{cc}} (\chi_{yy} + \chi_{zz}).\quad (3.22)$$

This derivation is presented in a more detailed form in Philip Louis' master thesis [60].

The measured quantity is the complex transmission  $S_{21}$ , which represents the voltage ratio between the VNA output (port 1) and input (port 2). By replacing the current using Ohm's law  $I = V_{\text{CPW}}/Z_0$ , with impedance  $Z_0$  the signal from the magnetization dynamics can be written as:

$$\Delta S_{21}(H_{\text{ext}}) = i\mu_0\omega \frac{l \cdot d_{\text{FM}}}{8\omega Z_0} (\chi_{yy} + \chi_{zz}) \cdot S_{21}^0.\quad (3.23)$$

It is taken into account, that the induced voltage enters with a factor of 1/2, as this is the voltage between the CPW and port 2 and not between the two ports.  $S_{21}^0$  is the setup transmission far from resonance, such that the measured transmission at fixed frequency is as follows:

$$S_{21}(H_{\text{ext}})|_f = S_{21}^0 + \Delta S_{21}(H_{\text{ext}}),\quad (3.24)$$

analogous to Ref. [60]. It should be noted, that depending on the measurement geometry either both susceptibility components (IP) or only one (OOP) are relevant. In the IP case, assuming small linewidth ( $\Delta H_{\text{FWHM}} \ll H_{\text{ext}}, M_{\text{eff}}$ ),  $\chi_{yy}$  is connected to  $\chi_{zz}$  by the ellipticity with  $\chi_{yy} \cdot H_{\text{ext}} \approx \chi_{zz} \cdot (H_{\text{ext}} + M_{\text{eff}})$ . In the OOP case ( $\mathbf{e}_z = \mathbf{e}_3$ ),  $\chi_{zz}$  vanishes, leaving only one component of the susceptibility.

Using a VNA, two different approaches can be selected. Either the field is fixed and the frequency is swept to scan the resonance or vice versa. During this work the continuous wave mode (cw-mode) was chosen, i. e., setting a fixed frequency and sweeping the magnetic field. The magnetic field is measured twice for each point, once before the VNA readout and once afterwards, and averaged. To obtain a good signal to noise ratio (SNR) the IF-bandwidth (IFBW) is set to a few Hz, thus, excluding broadband noise. As lowering the bandwidth comes at the cost of increased measurement time, IFBW of 1 Hz, resulting in 1 s per measurement point was selected for most samples.

### 3.4 Data Processing

The obtained raw data resembles a complex Lorentzian function and was fitted using a home-built labview-routine [60]. Its fitting function for the FMR signal is implemented as

$$S_{21}(H)|_f = A + B \cdot H + Z \cdot e^{i\Phi} \times \frac{\left( H + \frac{\left(\frac{\omega}{\mu_0\gamma}\right)^2 - H_{\text{res}}^2}{H_{\text{res}}} - i \frac{\Delta H_{\text{FWHM}}}{2} \right)}{\left( H + \frac{\left(\frac{\omega}{\mu_0\gamma}\right)^2 - H_{\text{res}}^2}{H_{\text{res}}} - i \frac{\Delta H_{\text{FWHM}}}{2} \right) \left( H - i \frac{\Delta H_{\text{FWHM}}}{2} \right) - \left(\frac{\omega}{\mu_0\gamma}\right)^2} \quad (3.25)$$

and is derived in [60]. Here,  $S_{21}^0 = A + B \cdot H$  is introduced to account for the setup transmission outside of FMR conditions. The linear term is implemented to account for temporal drift of the background.  $Z$  represents the resonance amplitude and  $\Phi$  is the resonance phase. The fraction is the susceptibility component  $\chi_{yy}$  divided by  $M_{\text{sat}}$ . Having two variables ( $M_{\text{eff}}$  and  $g$ ) for the resonance field (see Eq. (3.11)) it is not possible to extract both values from one measurement at a single frequency. Yet, Nembach *et al.* showed in their work [77], that it is possible to extract the resonance field and the linewidth from a fit by fixing the Landè-factor, e. g. with  $g = 2$ , without influencing their values. With the frequency dependent data, one then can extract the respective g-factor.

For the IP and OOP measurements the shape is exactly the same but the amplitude of the signal has to be adapted. As a quantitative evaluation of the response strength was of no interest during this study, details on the amplitude change are omitted. An exemplary data set is shown in Fig. 3.4 a) and b) with its respective fit to Eq. (3.25).

From the fit, the resonance field and the linewidth are extracted for each frequency and plotted as a function of  $f$ . We then use the OOP-Kittel (Eq. (3.12)) or the IP-Kittel equation (Eq. (3.11)) to fit the resonance field as a function of frequency after solving these equations for  $H_{\text{res}}$  with the result

$$\mu_0 H_0 = -\mu_0 H_{\text{aniso,IP}} - \mu_0 M_{\text{eff}}/2 + \sqrt{\frac{f^2}{(g\mu_B/h)^2} + (\mu_0 M_{\text{eff}})^2/4} \quad (3.26)$$

for IP and

$$\mu_0 H_0 = f \cdot \frac{h}{g\mu_B} + \mu_0 M_{\text{eff}} \quad (3.27)$$

for the OOP configuration. Equation 3.14 was used for the linewidth, dependent on the frequency, and was implemented as

$$\mu_0 \Delta H = \frac{2\alpha h}{g\mu_B} \cdot f + \mu_0 H_{\text{inh}}. \quad (3.28)$$

From the Kittel-fit the g-factor and the effective magnetization are extracted and the linewidth allows for determination of the Gilbert-alpha and the inhomogeneous linewidth

broadening. The presented anisotropy field in Eq. (3.26) has no physical meaning in the realized experiments, as this contribution is only seen as a shift on the x-axes. To really extract the IP-anisotropy one would need to measure at different rotational angles.

## 3.5 Experimental Results

During this work, several sample series were produced. Each series is based on a certain material stack sequence, where the individual samples differ in the Co<sub>25</sub>Fe<sub>75</sub> thickness. As the idea was to optimize for low-damping in Co<sub>25</sub>Fe<sub>75</sub>, for e. g. spin-orbit torques phenomena, heterostructures are necessary, which inherit additional contributions like spin pumping. To extract this augmentation of Gilbert-damping, the data within a series is plotted over the reciprocal FM-thickness  $1/d$ . As spin pumping is an interface effect, its influence scales as  $1/d$ , such that it is possible to obtain the intrinsic Gilbert alpha from such a thickness series [8, 63]. Only those data belonging to a series and displaying a fairly linear behavior are plotted and some obtained background information to the respective series will be given. Afterwards, the results will be discussed and the series will be compared to each other.

### 3.5.1 Ta - Cu - Co<sub>25</sub>Fe<sub>75</sub> - Cu - Ta

We start with the sample series consisting of the sequence SiO<sub>2</sub>/Ta/Cu/Co<sub>25</sub>Fe<sub>75</sub>/Cu/Ta, where all deposited layers were sputtered with nominally 3 nm. The Co<sub>25</sub>Fe<sub>75</sub> layer thicknesses for the different samples varied from 1.6 nm to 9 nm. In the following this series is referred to as the "Schoen"-series, as the stack is copied from the recipe presented in Schoen's work [8]. Both, IP and OOP measurements were performed for this series allowing for deeper insight into the FM/NM interface properties. In Fig. 3.4 a) and b) exemplary raw data obtained from an IP VNA measurement at 30 GHz is shown, together with fits to Eq. (3.25). From these fits, the resonance position and the linewidth is extracted and plotted as a function of the frequency in Fig. 3.4 c) and d), respectively. By fitting the resonance field with the aforementioned IP-Kittel Eq. (3.26) and the linewidth with the linear behavior described in Eq. (3.28), the important parameters are extracted. Namely, the effective magnetization  $M_{\text{eff}}$ , the Landè-factor  $g$ , the Gilbert alpha  $\alpha$  and the inhomogeneous linewidth broadening  $H_{\text{inh}}$ . The data in Fig. 3.4 e) and f) are obtained from an OOP measurement. In this configuration, the thicker samples showed more than one resonance interleaved with each other. Thus, the data points which could not be fitted properly were left out. All the extracted quantities are presented in Fig. 3.5 and will be discussed in the following.

In Fig. 3.5 a) the effective magnetization vs. the reciprocal thickness is presented. A linear dependence is clearly visible for both, IP and OOP measurements. Analogously to [8], we assume the saturation magnetization to be the extrapolated bulk value, which coincide very well for both geometries. Its value is also presented and compared to other series in Fig. 3.12. The scaling with  $1/d$  indicates the presence of an interfacial anisotropy along the surface normal. In the anisotropy energy density  $E$  given by Ref. [79]

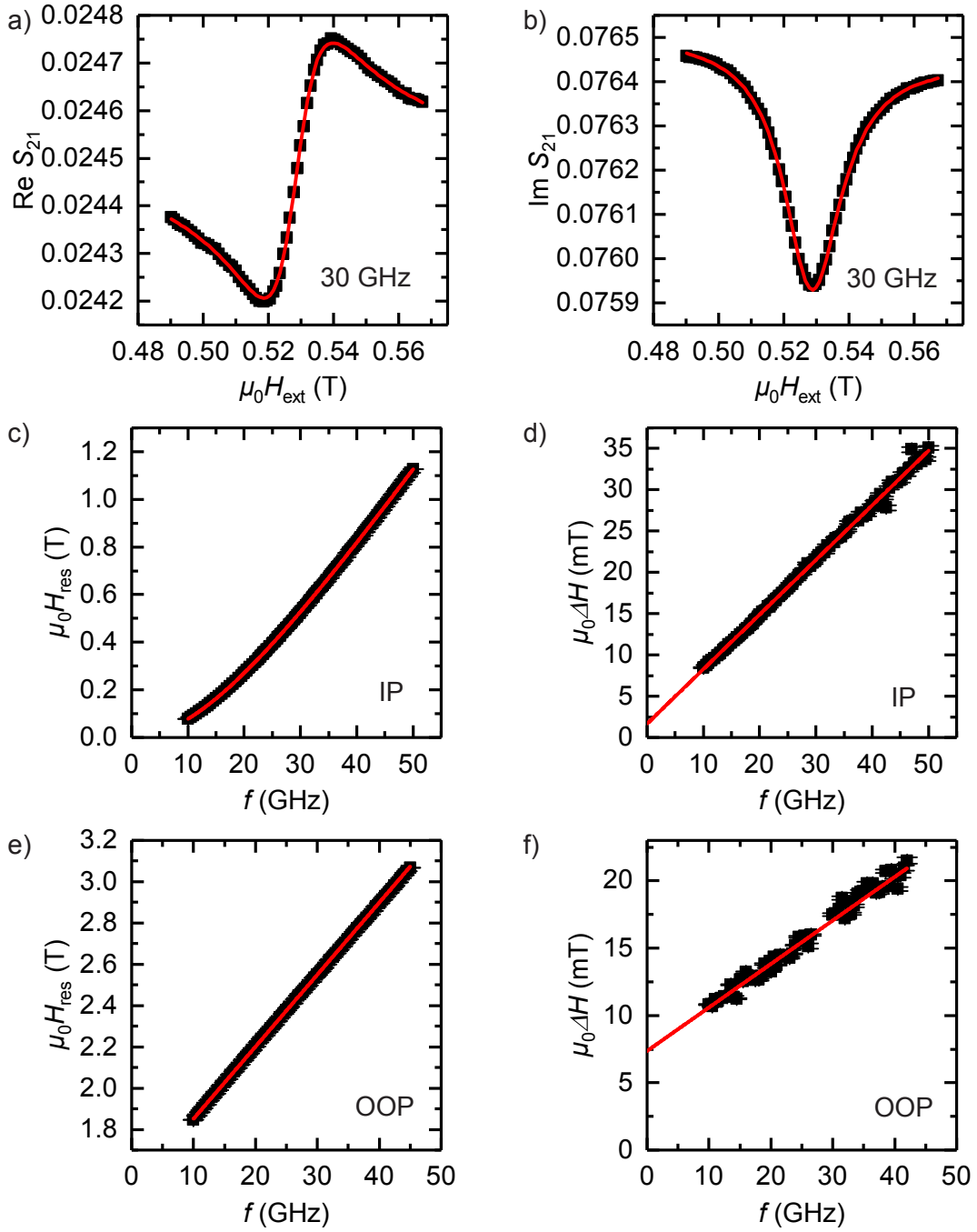


**Figure 3.4:** a) and b) show the raw data obtained from the IP VNA measurement of the sample "Schoen-007" (2.3 nm  $\text{Co}_{25}\text{Fe}_{75}$  layer) at 30 GHz. From the complex Lorentzian function, the resonance position and linewidth is extracted and plotted vs. the frequency resulting in c) and d), respectively. Corresponding OOP data was also acquired and is shown in the panels e) and f).

$$E = \frac{\mu_0 M_s^2}{2} \cos^2(\theta) - K_2 \cos^2(\theta) - \frac{K_4}{2} \cos^4(\theta), \quad (3.29)$$

we have the second-order and fourth-order perpendicular anisotropies. Here,  $\theta$  is the polar

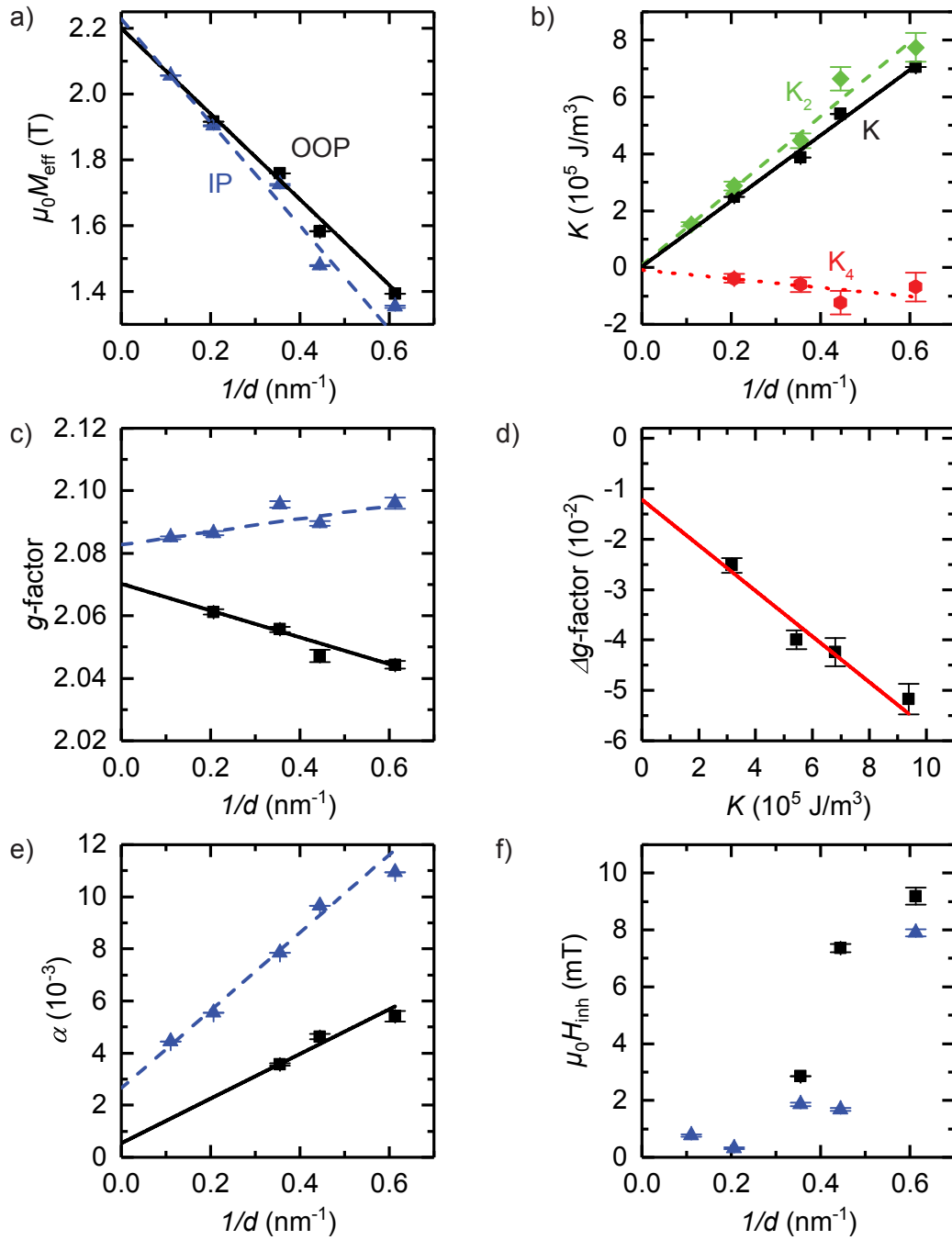


**Figure 3.5:** a) Effective magnetization of the "Schoen"-series. The extrapolated saturation magnetizations are  $\mu_0 M_s^{\text{IP}} = (2.23 \pm 0.04)$  T and  $\mu_0 M_s^{\text{OOP}} = (2.20 \pm 0.04)$  T. b) From a) the PMA is extracted and its higher order constants are plotted. c) The  $g$ -factor also scales linear with  $1/d$ , but also shows an asymmetry for both measurement geometries. This also results in a orbital moment asymmetry. d) relates the asymmetry with the PMA analogous to Ref. [78]. e) The Gilbert damping vs. the reciprocal thickness shows a linear behavior as expected from the spin pumping model. The bulk damping reaches  $\alpha_{0,\text{IP}} = (2.7 \pm 0.3) \times 10^{-3}$  and  $\alpha_{0,\text{OOP}} = (5.4 \pm 9.4) \times 10^{-4}$ . f) The inhomogeneous linewidth broadening increases by sputtering thinner FM layers.

angle relative to the surface normal. Analogously to Shaw *et al.* [78] we calculate these constants with

$$\begin{aligned} M_{\text{eff}}^{\text{OOP}} &= M_s - \frac{2(K_2 + K_4)}{\mu_0 M_s} = M_s - \frac{2K}{\mu_0 M_s} \\ M_{\text{eff}}^{\text{IP}} &= M_s - \frac{2K_2}{\mu_0 M_s}. \end{aligned} \quad (3.30)$$

The total perpendicular magnetic anisotropy (PMA) and their components are presented in Fig. 3.5 b). We see that the anisotropy increases with decreasing thickness. Thus, this quantity softens the hard OOP axis in the FM by opposing the shape anisotropy of the thin film. The slope of  $K$  accounts for the interface anisotropy, as discussed below. The vanishing y-axis intersect indicates the absence of further (volume) contributions to the anisotropy.

When investigating the  $g$ -factor, we observe a splitting for IP and OOP geometries. Such a behavior was already reported in 1949 by Kittel *et al.* [80, 81]. From their work, we know that the  $g$ -factor anisotropy is related to the ratio of orbital moment and spin moment. As Gimbert and Calmels argue in their work [82] that the spin moment in the saturated state is isotropic, the difference of  $g$  indicates a proportional orbital moment asymmetry. From Fig. 3.5 c) we also see a linear trend of this asymmetry, which is increasing with decreasing layer thickness. Our data is in agreement with the results from Shaw in Ref. [78]. The  $g$  factor in the IP configuration rises, whereas the OOP  $g$ -factor decreases with decreasing the layer thickness. In the bulk limit ( $1/d = 0$ ) we observe similar  $g$ -factors for OOP and IP configuration. Following the argument of Ref. [78], this is attributed to the perturbation of the electron orbit at the interface.

Shaw *et al.* also investigated on a linear relation between the PMA and the orbital moment asymmetry [78]. They refer to the tight binding perturbation theory from Bruno *et al.* [83], where  $K = A \cdot \Delta g$  depends linearly on the  $g$ -factor discrepancy. Here,  $A$  is a simplified factor. For multiple stack sequences, i. e., multiple layers grown repeatedly on top of each other, they find the model to agree with their results, where the asymmetry vanishes for zero anisotropy. For a simple FM between NM layers they find a negative slope and a non-negligible intersect of  $K = 0$  and conclude that the model does not work for a single alloy/NM stack. Their observation coincides very well with our finding in Fig. 3.5 d) even though they used a  $(\text{Co}_{90}\text{Fe}_{10})\text{Ni}$ -alloy. This may indicate that the physical relation between orbital moment asymmetry and PMA for a single FM layer is different to that of a FM/NM multilayer stack.

In contrast to the very well coinciding effective magnetizations, which were used for the discussion about the perpendicular anisotropy, the damping parameter differ significantly for the two measurement geometries. In Fig. 3.5 e) the damping of IP and OOP is shown. For the extrapolated bulk values this difference is probably due to two-magnon scattering, which is completely suppressed for the OOP configuration [84]. As the magnon-magnon scattering renders a relaxation path for the oscillating magnetization, damping increases in its existence. A possible additional contribution is an anisotropy of the Gilbert damping parameter, which will be discussed below. As the contribution to the linewidth is supposed

to be independent from the thickness [84, 85] this would lead to a parallel increase of IP and OOP. Clearly, however, the slope of  $\alpha$  vs.  $1/d$  is smaller for the OOP configuration. When calculating the effective spin mixing conductance by Eq. (3.16), this results in a higher value for the IP geometry (see Fig. 3.12). If the model of the spin pumping causing the linear increase with  $1/d$  is applicable to our samples, this indicates a more effective pumping for IP configurations. Very recently, Chen *et al.* reported on anisotropic Gilbert damping [86]. They investigated a single-crystalline FM/semiconductor interface and showed a change in  $\alpha$  depending on the direction of the applied magnetic field. Theory already predicted anisotropic damping for crystalline FMs [87–90] but in our case we have polycrystalline materials. Further investigation is needed to ascertain whether we indeed see an anisotropy of the damping or a change in spin pumping efficiency for IP and OOP configurations. Finally, the OOP Gilbert damping parameters that we obtain, are in close agreement to those published in Schoen's work [8] for the nominally identical stack sequence. Thus, also the value of the effective OOP spin mixing conductance, coincides with their data fairly well (see Fig. 3.12).

An additional trend obtained from the data is the increase of inhomogeneous linewidth broadening for thinner films. Even though the plot in Fig. 3.5 f) does not exhibit a linear increase with  $1/d$  we clearly see this trend. This shows, that by decreasing the FM thickness extrinsic damping due to inhomogeneities gains relevance.

### 3.5.2 Pt - Co<sub>25</sub>Fe<sub>75</sub> - Ta

Having in mind that by optimizing the Co<sub>25</sub>Fe<sub>75</sub> damping applications like spin-Hall nano-oscillators use spin transfer torque [7, 91, 92] a different sequence was tested in order to have more spin pumping. In this part we present a series grown as the following: SiO<sub>2</sub>/Pt/Co<sub>25</sub>Fe<sub>75</sub>/Ta. The seed and cap layer both were designed to be 3 nm thin and the FM varied between 1.9 nm to 8.3 nm. This series will be called "PCFT" due to the metals used. Unfortunately, only IP measurements could be realized for the PCFT samples. A representative data set from the sample "PCFT-018" is presented in Fig. 3.6. We see the typical IP-Kittel line and a very linear increase of the linewidth with frequency for all the samples presented in Fig. 3.7. As for the previous series, the effective magnetization scales linear with  $1/d$ , which again indicates the PMA (Fig. 3.7 b)). As we lack of OOP data, only the second order anisotropy can be determined. In Fig. 3.7 c) we see that also the  $g$ -factor does not show any clear dependence on the FM thickness, other than before. Apparently, the geometric confinement does not perturb the electron orbits at the interface in a significant way.

When looking at the Gilbert damping in Fig. 3.7 d), a linear increase with  $1/d$  is observed. This again suggests the expected spin pumping interface effect. Measuring in the IP configuration, we expect two-magnon scattering which also increases the offset of the line. By acquiring OOP data one could then extract its influence. The resulting effective spin mixing conductance is presented and discussed in Fig. 3.12 in the comparison section. The "PCFT" series also shows an increase of  $\mu_0 H_{\text{inh}}$  by sputtering thinner FM films. It is not possible to conclude a typical interface effect due to the lack of linearity in  $1/d$ , but the

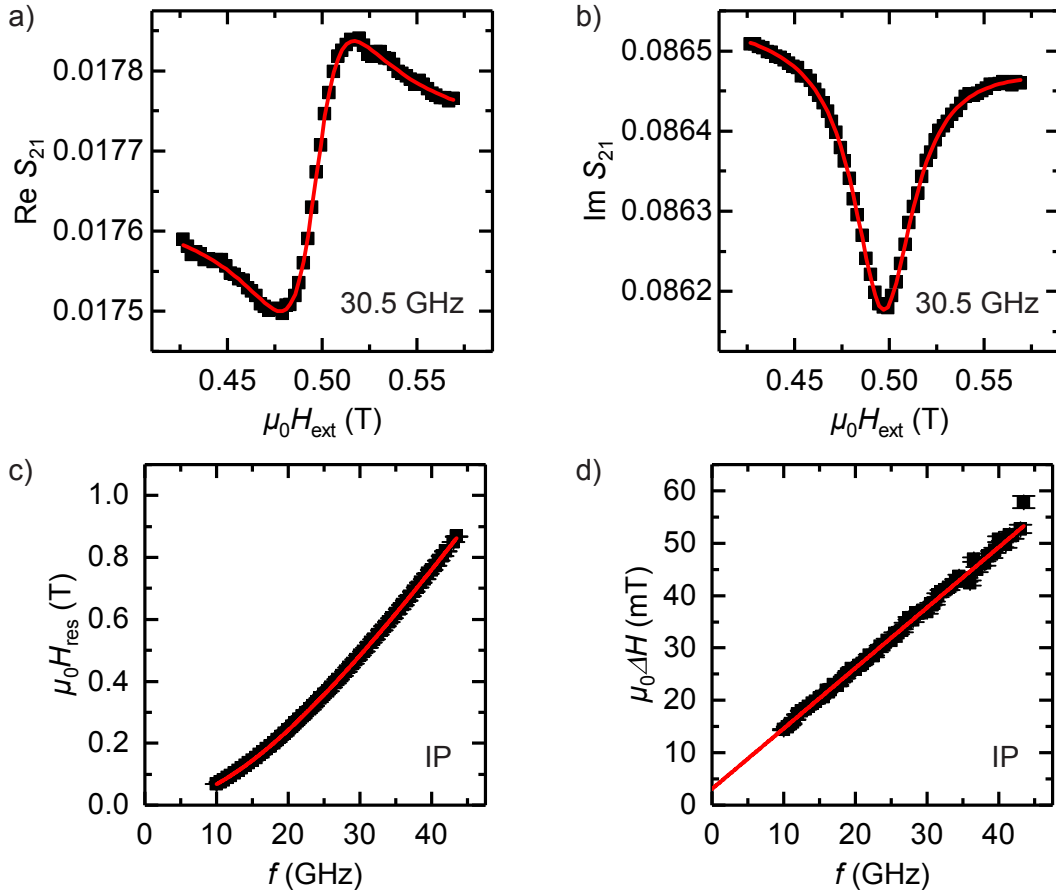


**Figure 3.6:** a) and b) show the transmission coefficient of the IP measurement for the "PCFT-018" (2 nm  $\text{Co}_{25}\text{Fe}_{75}$  layer) sample at 30.5 GHz. c) presents the frequency dependent resonance position matching perfectly with the IP-Kittel equation. d) shows the linear increase of linewidth with the frequency.

influence of roughness or inhomogeneities seems to gain significance at small thicknesses. By increasing  $d$ , the inhomogeneous linewidth broadening seems to approach 0 mT.

For the "PCFT"-series some more variations in the sample fabrication were realized to gain some insight to different aspects of the growth. When omitting the seed layer, i. e., sputtering  $\text{Co}_{25}\text{Fe}_{75}$  directly on the  $\text{SiO}_2$  substrate and only using a Ta cap layer, the damping jumps to significantly higher values. Furthermore the Gilbert parameter scatters when plotted vs.  $1/d$ , such that spin pumping can not be discussed. The growth on  $\text{SiO}_2$  seems to be unfortunate, such that we can conclude that a seed layer is indispensable.

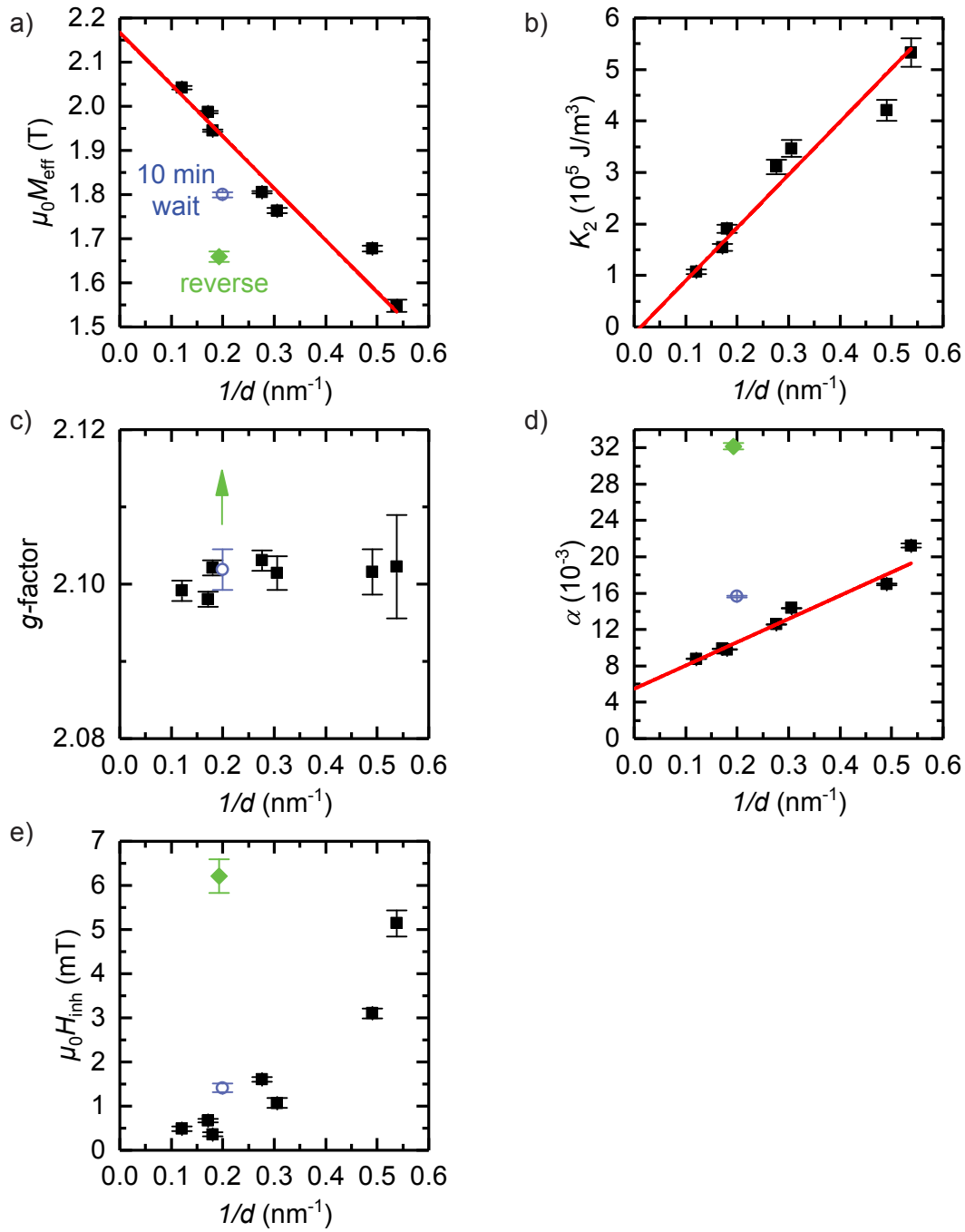


**Figure 3.7:** a) The effective magnetization for different samples exhibit a linear trend depending on the reciprocal thickness resulting in  $\mu_0 M_s = (2.17 \pm 0.03) \text{ T}$ . The blue circle indicates the sample which was sputtered with a waiting time of 10 min and the green diamond represents the sample with reversed stack sequence. b) Analogous to the linear dependence of the effective magnetization in a) caused by the PMA its second order value is presented. c) The Landè-factor stays constant for all thickness. d) shows the expected trend of the Gilbert damping parameter for spin pumping and a rather high extrapolated bulk value. This may be caused by two-magnon scattering. The bulk value reaches  $\alpha_0 = (5.5 \pm 0.5) \times 10^{-3}$ . e)  $H_{\text{inh}}$  decreases by increasing thickness and approaches zero for bulk thicknesses.

Another variation was applied to the sputtering time. One sample was prepared in one go whereas the second (nominally the same) was capped with Ta 10 minutes after the FM deposition. During this waiting time, the sputtering machine held all other parameters constant, analogous to a "normal" deposition. In Fig. 3.7 a) and d) we see that the result is a decrease of the effective magnetization and a significant increase of the magnetic damping. One idea for an explanation is that at operating sputtering pressures there is still sufficient oxygen which oxidizes the FM layer. Many metal-oxides tend to exhibit higher damping parameters [93, 94], which would explain the jump in Fig. 3.7 d). Also the lower effective magnetization fits to this idea. We see a small increase in the inhomogeneity too, whereas the  $g$ -factor stays the same.

The third variation was the reversal of the stack sequence to  $\text{SiO}_2/\text{Ta}/\text{Co}_{25}\text{Fe}_{75}/\text{Pt}$ . Considering only the spin pumping contribution, one would assume no significant change in the magnetic damping. Surprisingly, all parameters changed drastically (see Fig. 3.7). The  $g$ -factor increased to up to  $g = 2.278 \pm 0.006$ , such that including the point in graph 3.7 c) would render the other values to an almost flat line. Apparently, sputtering  $\text{Co}_{25}\text{Fe}_{75}$  on polycrystalline Ta leads to high inhomogeneities, such that only by the growth conditions the magnetic properties are changed drastically.

### 3.5.3 Pt - Cu - $\text{Co}_{25}\text{Fe}_{75}$ - Cu - Ta

As the intrinsic damping for the IP geometry increased by a factor of approximately two for the "PCFT"-series compared to the "Schoen"-series, the next modification was to use a Cu spacer layer. The sequence is called "PCFT-S" analogous to the series before but with the spacer. Except for the thinnest sample in OOP configuration, all transmission coefficients showed a single resonance. Figure 3.8 shows some exemplary IP and OOP data of the sample with 5.3 nm  $\text{Co}_{25}\text{Fe}_{75}$ . When applying the external field parallel to the sample surface, the linewidth of all samples was almost perfectly linear as seen in 3.8 d). For the OOP measurements only a limited frequency range is available. The upper limit is due to the maximum field we can apply, whereas on the lower side we begin to leave the range of fully aligned magnetization. In Fig. 3.8 e) we see this as the resonance position exhibits a small flexion. When looking at the linewidth, some samples showed an increase in damping at low frequencies and others scattered in a certain frequency range. Hence, for both quantities the fitting function is only applied in the areas where the linear behavior is observed.

In this series, the effective magnetization is almost identical for both measurement geometries, as can be seen in Fig. 3.9 a). By using Eq. (3.30) we can then extract the PMA, which is shown in panel b). Again, we see the same behavior as in Ref. [78], but different to their result and the data from the "Schoen" series the  $g$ -factor scales linearly only for the IP measurements. One would have assumed a linear, negative slope for the OOP  $g$ -factor vs.  $1/d$ , such that the orbital moment asymmetry rises with decreasing FM thickness. To this point, it is not clear why the behavior changes qualitatively by using a different measurement geometry.

In Panel d) of Fig. 3.9 we see the Gilbert damping parameter  $\alpha$ . As expected from

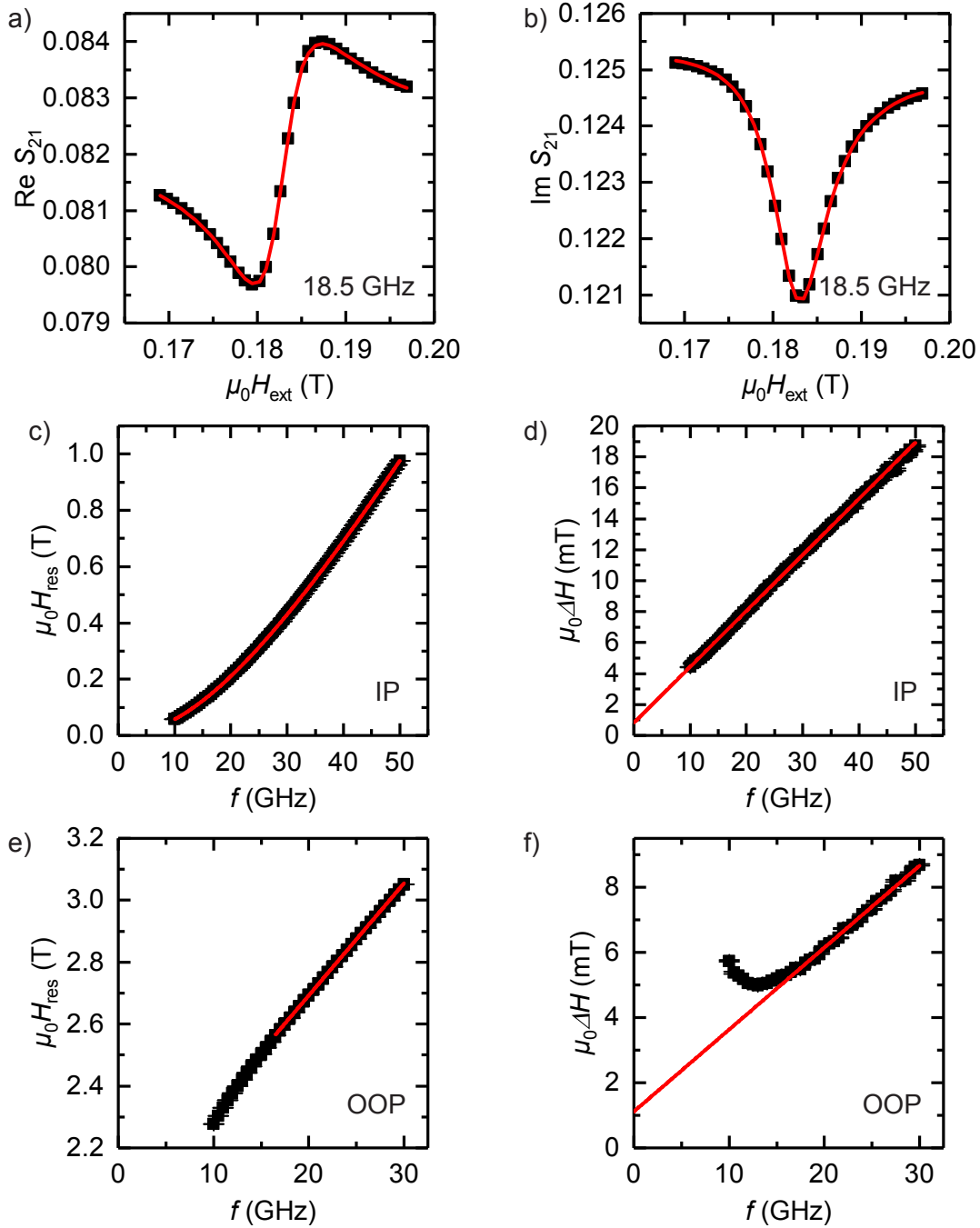


**Figure 3.8:** a) and b) show the single resonance data in IP geometry of the "PCFT-S-001" (5.3 nm  $\text{Co}_{25}\text{Fe}_{75}$  layer) at 18.5 GHz. In c) and d) one sees the resonance position and linewidth dependent the frequency for the IP configuration, whereas e) and f) show the same sample measured OOP. Both were only fitted to a frequency of 16.5 GHz as the linear behavior ends.

the spin pumping model, the damping rises linearly. We see an outlier for the thinnest sample in the OOP. As mentioned before, extracting the linewidth is rather delicate for this sample, also indicated by the large error bars. Again, this difference probably comes from the additional magnon-magnon scattering, occurring when going from OOP to IP [84].

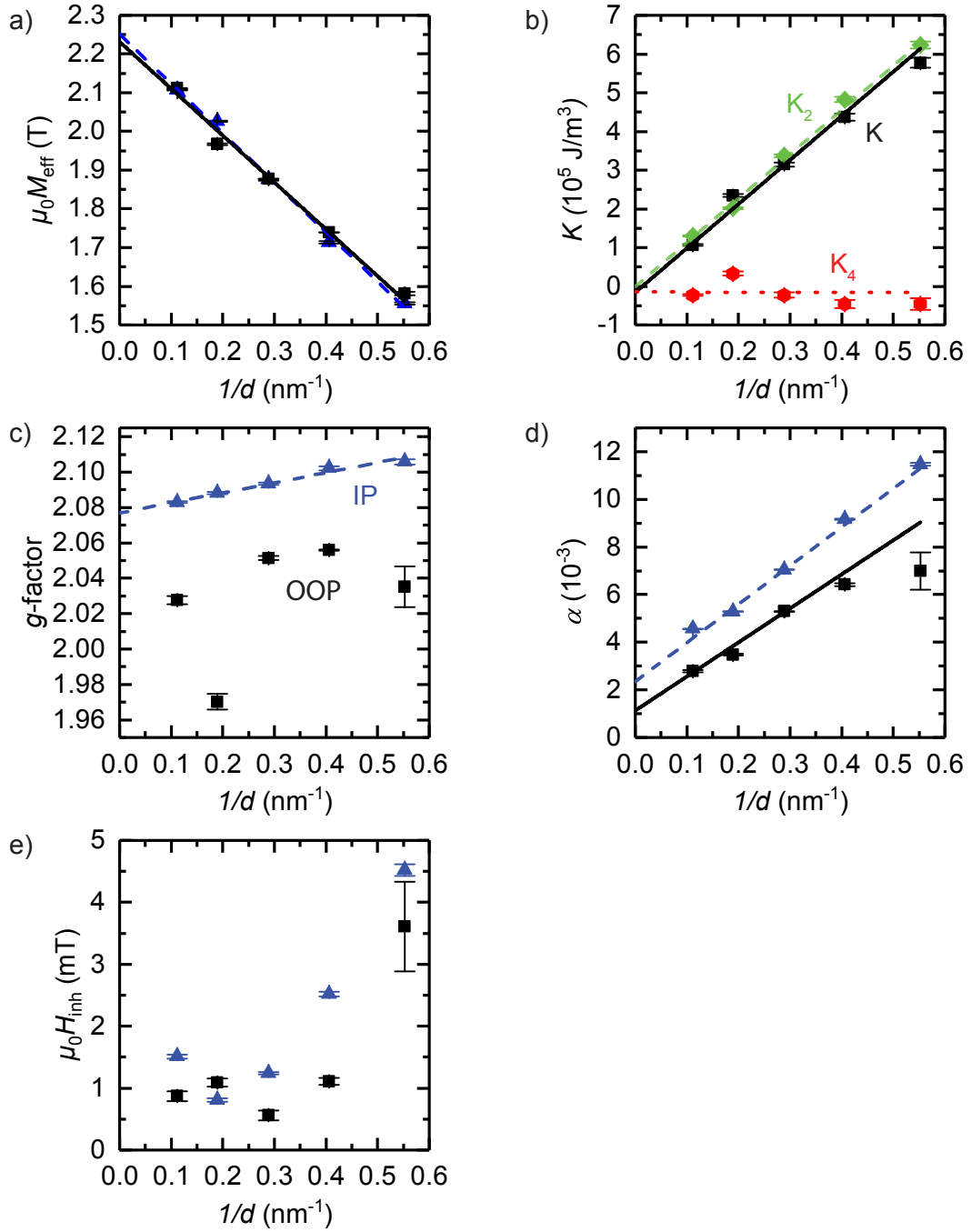


**Figure 3.9:** a) The effective magnetization vs.  $1/d$  returns a saturation magnetization  $\mu_0 M_{s,IP} = (2.25 \pm 0.01)$  T and  $\mu_0 M_{s,OOP} = (2.23 \pm 0.01)$  T for the "PCFT-S"-series. In b) the PMA extracted from the effective magnetization in a) is illustrated. The  $g$ -factor presented in c) shows a linear dependency on the reciprocal thickness for IP, whereas the OOP behavior is qualitatively different. In d) we acquire a bulk damping parameter of  $\alpha_{0,IP} = (2.4 \pm 0.3) \times 10^{-3}$  and  $\alpha_{0,OOP} = (1.1 \pm 0.5) \times 10^{-3}$ . e) presents  $H_{inh}$  of the five samples investigated.

As the slope for both configurations is identical within their uncertainty, we conclude that the effectiveness of spin pumping stays the same for both geometries.

When looking at  $\mu_0 H_{\text{inh}}$  in Fig. 3.9 e) we see the same trend as for the two series before, that by going to thinner FM layers inhomogeneities gain relevance. Unfortunately, this series still exhibits a Gilbert parameter more than twice as high in OOP geometry than the "Schoen" series. In the following the next modification in stack sequence will be discussed.

### 3.5.4 Ta - Al - Co<sub>25</sub>Fe<sub>75</sub> - Al - Ta

The two series containing Pt as a seed layer showed higher intrinsic damping than the series using Ta instead. Thus, the Ta seed layer is implemented again, but this time using Al as a spacer layer instead of Cu. Al also has a high spin diffusion length surpassing at least 350 nm at room temperature [95, 96], making it a valid spacer material. This series is referred to as the "Terminal"-series in the following and raises intriguing results for the magnetic Gilbert damping. In order to provide a traceable origin of the data leading to the ultra-low damping, all graphs used to extract the Gilbert damping parameter are presented in Fig. 3.10. Panels a) - d) show the linewidth vs. frequency for the four samples used to extrapolate the intrinsic damping. Even though not all graphs show a perfect line, a linear increase still seems a valid interpretation of the data. The thickest sample shown in panel e) exhibits an increase at low frequency. This feature can be described by the slow-relaxing impurity-relaxation mechanism described by Nembach *et al.* in Ref. [77]. To fit, the Eq. (13) and (15) of their work [77] are used. As we can see here, the interpretation of linear Gilbert damping is hardly possible due to the small frequency range limited by the magnetic field. Hence, the  $\alpha$  obtained from the 9.3 nm sample is not included in the linear spin pumping fit in Fig. 3.11. Regarding the resonance position, all samples allowed for extraction of the effective magnetization and the Landè-factor as indicated in Fig. 3.10 f).

As seen from the effective magnetization vs  $1/d$  in Fig. 3.11 a), the saturation magnetization is calculated to reach  $\mu_0 M_s = (2.30 \pm 0.16)$  T. The more interesting part is panel b), where we see the obtained Gilbert parameters from the samples presented before. When assuming spin pumping to be the responsible interface effect for the linear increase, we can extrapolate the intrinsic damping by using the four thinnest samples. The result is an astonishing value of  $\alpha_0 = (-1.6 \pm 3.4) \times 10^{-4}$ . Of course, values below zero are non-physical results, but within the error the maximum obtained damping does not even surpass  $\alpha_{\text{max}} = 0.2 \times 10^{-3}$ . When comparing these results with the recent publications concerning Co<sub>25</sub>Fe<sub>75</sub> [8, 97, 98], which all report of ultralow magnetic damping, our extrapolated  $\alpha_{\text{max}}$  still undercuts literature values. However, by using a Ti/Cu seed layer, Edwards *et al.* reduced spin pumping significantly and reports of a total damping parameter smaller than  $1.3 \times 10^{-3}$ . The lowest total  $\alpha$  we measured is a bit higher, yet the extrapolated, intrinsic damping of Edwards' thickness series is only slightly above  $1.0 \times 10^{-3}$  in polycrystalline Co<sub>25</sub>Fe<sub>75</sub> [97]. By fabrication of high quality epitaxially grown Co<sub>25</sub>Fe<sub>75</sub> (6.8 nm) on MgO, and thus minimizing impurities which increase the damping, Lee *et al.* report of  $\alpha = (7.1 \pm 0.6) \times 10^{-4}$  [98]. Indeed, theory predicts an intrinsic damping in the  $10^{-4}$  regime for Co<sub>25</sub>Fe<sub>75</sub> [11]. By smartly engineering the heterostructures containing Co<sub>25</sub>Fe<sub>75</sub>, metallic ferromagnets start to significantly gain relevance for spin transport applications.

When looking at the  $g$ -factor in Fig. 3.11 c), no linear trend is observed. But by comparing

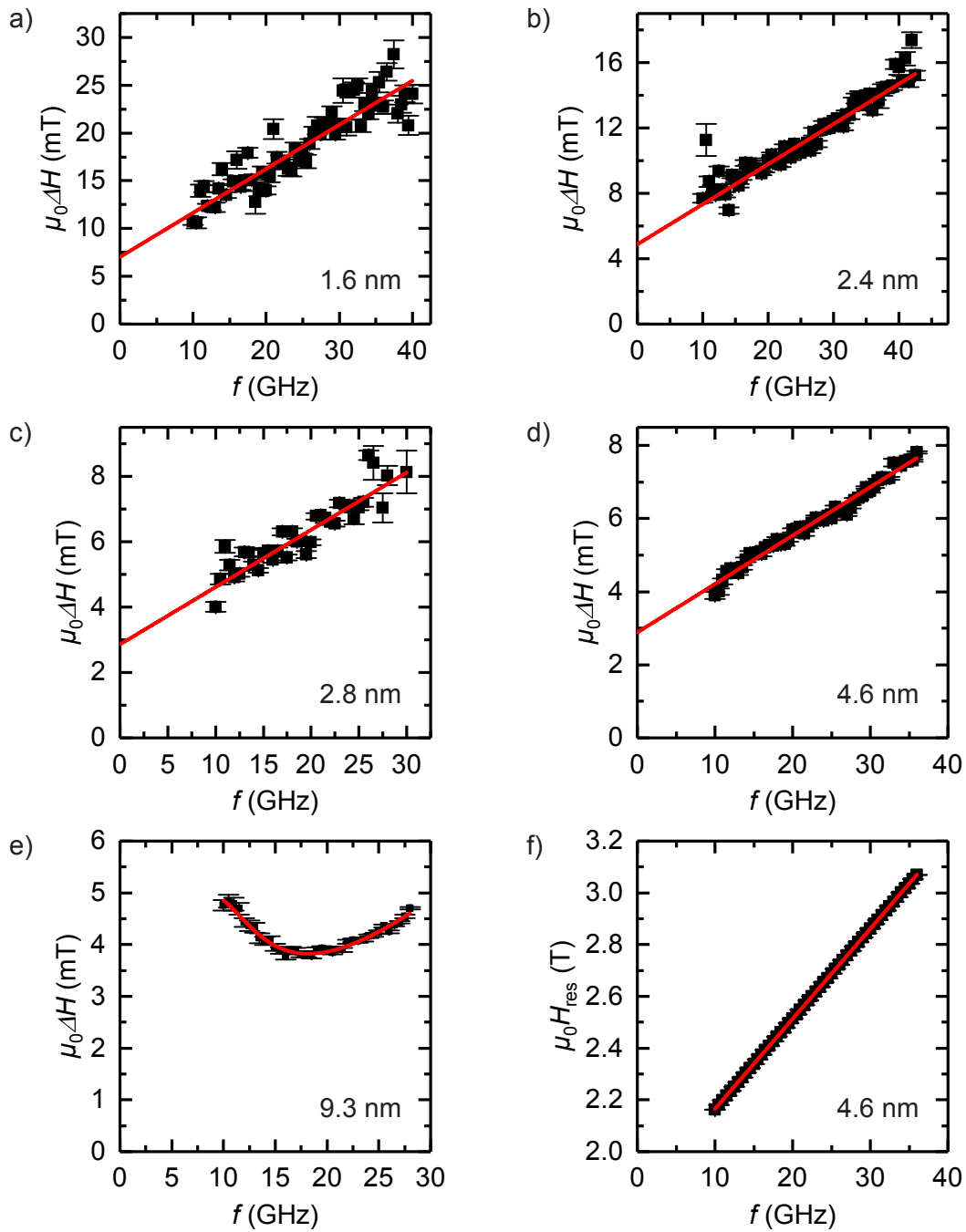


**Figure 3.10:** a) The resonance position vs. frequency in OOP configuration for the 4.6 nm  $\text{Co}_{25}\text{Fe}_{75}$  "Terminal"-sample. This behavior is representative for the other samples. b) - f) show the linewidth of the resonance for all five investigated samples. Even though scattering is observable for the thin samples, Gilbert damping can be assumed for the b) - e). In f) we see an increase which can be described by considering slow relaxing impurities.

it to the OOP data from the "PCFT-S" series, it seems to exhibit a similar behavior. Coming from thin FM layers the  $g$ -factor rises and then drops rather fast at some point. By systematic investigation of more samples and the Landè-factor one could find out, where

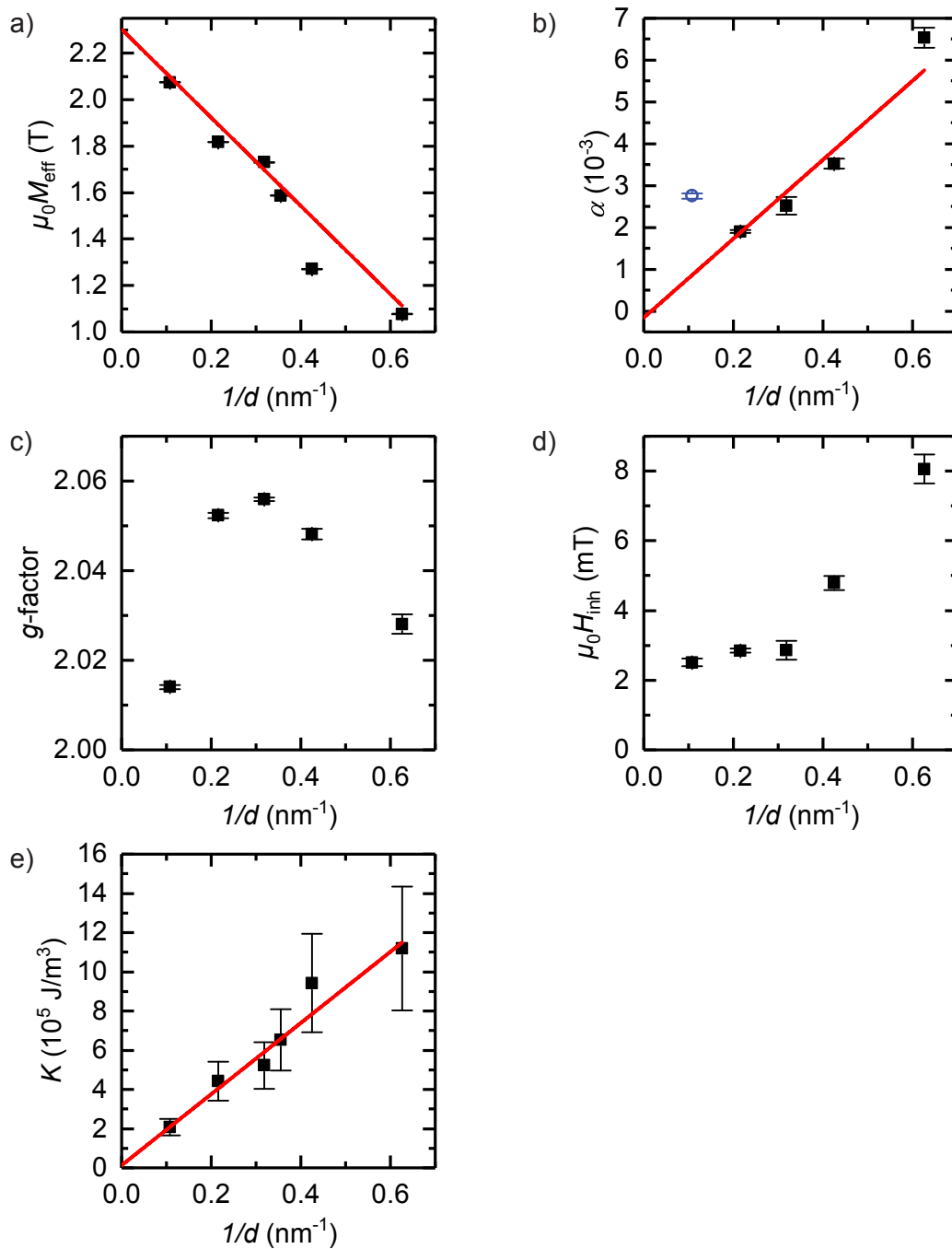


**Figure 3.11:** a) presents a  $M_s = (2.30 \pm 0.16)$  T for the "Terminal"-series. In b) the extrapolated damping parameter reaches an ultra-low value of  $\alpha_0 = -1.6 \pm 3.4 \times 10^{-4}$ . The blue point indicates the 9.3 nm sample, which was not considered for the linear fit. c) and d) present the  $g$ -factor and the inhomogeneous linewidth broadening vs.  $1/d$ , respectively. The PMA for the sample series is shown in panel e), where the high uncertainties originate from the rather high error in the saturation magnetization.

this behavior comes from. Regarding  $\mu_0 H_{\text{inh}}$  in panel d), we see the typical increase by depositing thinner FM layers. In panel e) the PMA is shown, where we see the linear

increase with  $1/d$ , yet have fairly high error bars. This uncertainty comes from the rather high uncertainty of the saturation magnetization.

### 3.5.5 Comparison

The magnetic properties and other behaviors crucially depend on the deposition condition and stack sequence as can be inferred from the presented data. The similarities and differences will be discussed in the following.

All through the different stack sequences we observed an increase for the inhomogeneous linewidth broadening, when fabricating thin FM layers. Even though no quantitative conclusions can be made from the data, we know that small linewidths in the resonance for FM layers within the presented stacks in the lower nm regime are hard to realize. This may come from the significant increase of influence of inhomogeneities when only having thin ferromagnetic layers.

Figure 3.12 a) shows another similarity. The extrapolated saturation magnetization stays within a small interval for all stack sequences. The highest value is reached for the "Terminal" series, but we also have to consider the high uncertainty, such that in good approximation the saturation magnetization is identical for all samples. It may be possible that the dead layer thickness varies a bit depending on the seed or cap layer, but this seems to be of - if any - minor importance. Where we do see a change, is the interfacial anisotropy of the PMA (Fig. 3.12 b)). The first three series coincide within their values, but the "Terminal" stack exhibits a higher PMA. This could be used when wanting not too thin FM layers without any favored magnetization direction. For the realization, the shape anisotropy has to be compensated by the PMA. It increases proportional to  $K_{\text{int}}/d$ , such that a high interfacial anisotropy allows for thicker FM layers, still compensating the shape anisotropy. In this case the critical thickness increases from 0.6 nm to 0.8 nm going from the first three to the last series.

When comparing the Landè-factor, we observe three qualitatively different behaviors. The sample series without any spacer layer exhibits a constant  $g$ -factor for all investigated thicknesses. The "Schoen" and the "PCFT-S" show a linear dependence of  $g$  in at least one measurement geometry. Shaw *et al.* mention a perturbation of the electron orbit by geometrical confinement, which can cause this behavior [78]. The third behavior is seen in the OOP configuration of the "PCFT-S" and the "Terminal" series. By increasing the FM thickness, the  $g$ -factor first increases and then drops rather fast. In the series containing the Pt seed layer we also see that  $g$  rises again. Assuming this to have a real physical background we could conclude a certain FM thickness were the  $g$ -factor becomes minimized. Unfortunately, at this point the reason for this behavior is not known to us.

In Fig. 3.12 c) the total effective spin mixing conductance of cap and seed layer interfaces merged together is shown for the different samples. We assume the cap and seed layer in the "Schoen"-samples to contribute equally to the spin pumping in order to extract the  $g_{\text{eff}}$  of the Ta/Cu/Co<sub>25</sub>Fe<sub>75</sub> interface. Even though the cap layer becomes oxidized and hence, the Ta cap layer is thinner than the seed layer this seems to be a valid approach. The seed layer has a thickness of about 3 nm, whereas the Ta in the cap layer is about 1.5 nm - 2 nm

thin. By using Eq. (3.17) and taking the important material parameters from Boone's work [99] we find that the difference in backflow is less than 10 % for the two interfaces. The result for a single interface is given for IP and OOP by the red, full diamond and the green, empty diamond, respectively. As the same interface is given in the "PCFT-S"-series, we can subtract the  $g_{\text{eff,Ta}}$  from the total effective spin mixing conductance to obtain  $g_{\text{eff}}$  for the Pt/Cu/Co<sub>25</sub>Fe<sub>75</sub> interface. Those are presented analogous to the Ta-interface but using triangles. As expected,  $g_{\text{eff}}$  is higher for Pt than for Ta. As both metals have rather small spin diffusion lengths, the difference originates mainly from the difference in electrical conductivity. Looking at Eq. (3.17), we see that a lower electrical resistivity leads to a higher efficiency factor, increasing the effective mixing conductance. Thus, Pt works as a "better" spin sink than Ta.

For the "Terminal"-series it is not possible to extract  $g_{\text{eff}}$  for a single interface as we found an intermixed layer of TaAl in the cap layer by XRD measurements, such that the approximation of equal seed and cap layer does not hold anymore. The samples without any spacer exhibit the highest spin mixing conductance. Even though Cu has a spin diffusion length higher than 100 nm [100], it apparently has a significant influence on the spin pumping. As "PCFT-S" and "PCFT" only differ by the Cu spacer layer and one would assume no influence on the spin current due to the high diffusion length in Cu, this huge difference between the two sample series seems surprising. Maybe the Cu we sputtered has a low spin diffusion length and thus a higher backflow rate than expected, which would explain the difference. For the IP configuration of the "Schoen" and the "PCFT-S" we see very little difference. This is also surprising, as Pt should absorb the spin current way better. This also hints toward some unexpected behavior of the sputtered Cu. The difference in the OOP configuration for those two samples then maybe does not come from the difference of backflow rate for Pt and Ta as expected, but mainly from the anisotropic efficiency of the spin pumping effect in the "Schoen" stack sequence. There is currently not much information about this anisotropic discrepancy. Chen *et al.* from the Back group recently published on the anisotropy of the Gilbert damping parameter of Fe on GaAs [86], as mentioned before. Some further investigation could be done to find out more about this anisotropy.

This directional dependence would also mean that the difference of the intrinsic damping for IP and OOP of the "Schoen"-series in Fig. 3.12 d) is not only due to two-magnon scattering but also due to this anisotropy. If the difference of the two geometries would come only from two-magnon scattering, we would assume to see the same difference for the "Schoen" and the "PCFT-S"-series in panel b) as this relaxation mechanism does not depend on the adjacent layers. Assuming no such anisotropy in the "PCFT-S"-series and expecting only magnon-magnon scattering and anisotropy for the difference of IP and OOP in the "Schoen"-series we can guess its influence on the damping parameter to reach approximately  $\Delta\alpha_{\text{aniso}} = 0.9 \times 10^{-3}$ , which is approximately a third of the total intrinsic damping.

For the "PCFT"-series the high damping parameter is also surprising. As the more efficient spin pumping seen in panel c) should have no influence on the extrapolated bulk value this high  $\alpha$  is not explainable with a spin current flowing out. A different explanation

is needed, which may come by considering growth conditions. As Edwards points out, magnetic 3d transition metals grow very well on Cu templates with good magnetodynamic properties [97]. It is thinkable that Pt as a seed layer does not provide the wanted growth conditions, leading to higher damping values.

Apparently, using Al instead of Cu as a seed layer does not have such bad influence on the resonance relaxation. By replacing the spacer we observed a record Gilbert damping parameter of  $\alpha_{\max} = 1.8 \times 10^{-4}$ . Some more samples with thickness variation should be fabricated in order to confirm this ultra-low intrinsic damping found.

Spintronic and magnonic applications benefit from low magnetic damping, but for such applications the multilayers have to be structured into mesas. Changing the shape to a micrometric scale can have a major impact on the magnetic properties as e.g. shape anisotropy becomes more relevant. Thus, some first proof of concept experiments with structured samples were realized during this work presented in the next chapter.

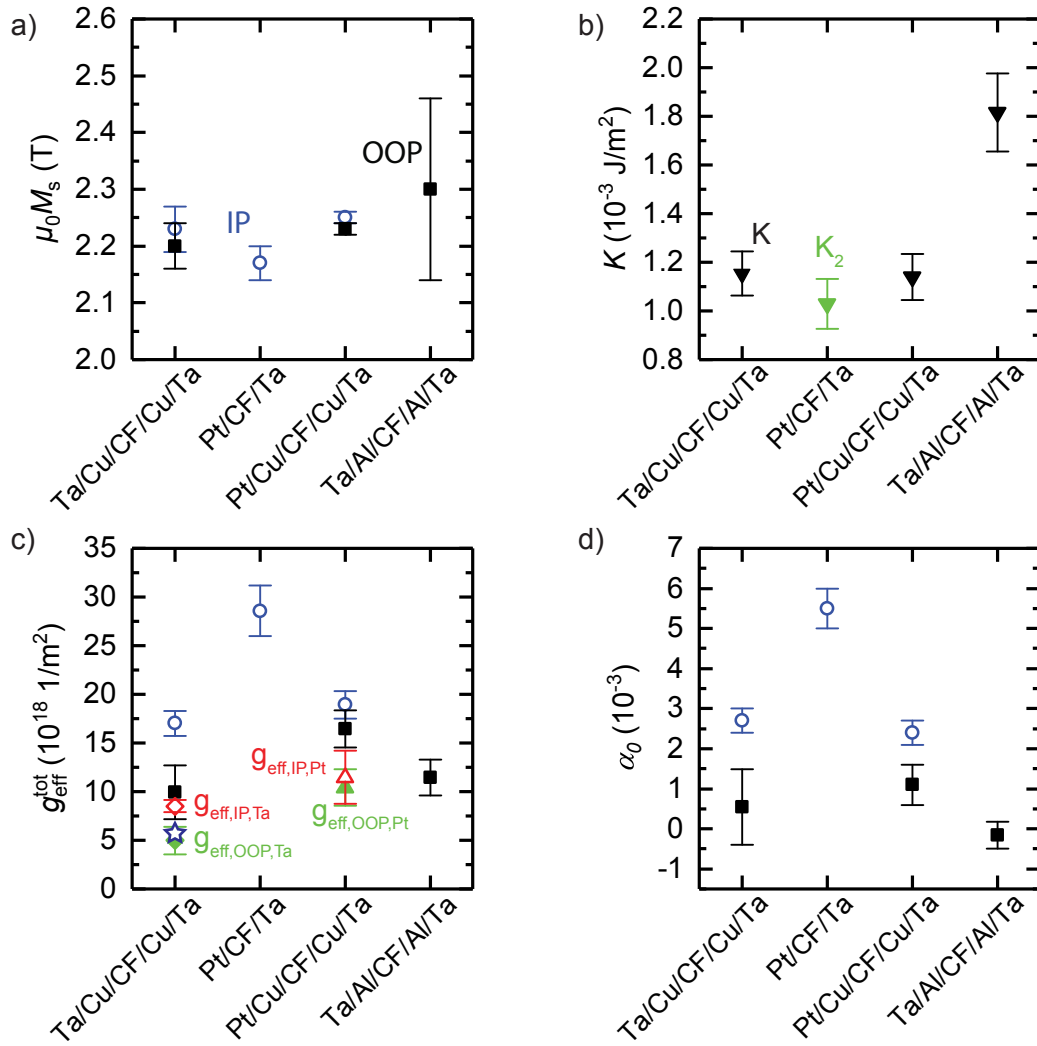


**Figure 3.12:** Comparison of the most important results of the four presented sample series. Here, the "CF" in the naming stands for  $\text{Co}_{25}\text{Fe}_{75}$ . a) presents the extrapolated saturation magnetization for the different stack sequences. Panel b) compares the PMA for the four series. As for Pt/ $\text{Co}_{25}\text{Fe}_{75}$ /Ta only IP data was measured only the second order constant could be extracted. c) Shows the total effective spin mixing conductance for seed and cap interfaces together. The single interface values for Ta/Cu/ $\text{Co}_{25}\text{Fe}_{75}$  and Pt/Cu/ $\text{Co}_{25}\text{Fe}_{75}$  are also shown. The open symbols represent IP and the closed ones OOP data. The star indicates the published value in Schoen's *et al.* work [74]. In d) the found Gilbert parameters are compared showing the record value of  $\alpha_{\text{max}} = 1.8 \times 10^{-4}$  for the Ta/Al/ $\text{Co}_{25}\text{Fe}_{75}$ /Al/Ta series.

## Chapter 4

# Magneto-Optical Detection of FMR and Spin Wave Propagation in Structured $\text{Co}_{25}\text{Fe}_{75}$

The application of low damping materials in spintronics requires structuring to define the device geometries. Therefore, the low Gilbert parameters obtained from the FMR measurements for blanket films have to be reproduced for geometries in the micrometer (or even nanometer) scale. The first step in this part of the work was investigating whether the structured material maintains its magnetic properties compared to the blanket film. As a second step, spin-wave propagation was measured. These experiments were realized with microfocused Brillouin light scattering (BLS). In the first part, the basic physics for the experiment will be explained and afterwards, the experimental setup will be presented. Finally, the obtained experimental results will be shown and discussed.

### 4.1 Fundamentals and Setup of BLS

Brillouin light scattering describes the scattering of photons with the quasiparticle excitations - such as phonons and magnons - of a solid. This measurement method was first described by L. Brillouin in 1992 [101]. In our case, the photons scatter off magnons, or spin waves. In the ground state of a ferromagnetic system, all spins are aligned parallel to each other. When going to non-zero temperature, the spin system becomes excited. We start with imagining the very first excited state as a single spin in our system flipped to an antiparallel configuration, raising the total energy within our magnetic structure and reducing our total magnetization by spin  $1/2 + 1/2 = 1$ . Yet, localization of this single flipped spin is energetically unfavorable due to exchange coupling, such that the spin flip is rather distributed among all spins by tilting each of them by a small angle. The result is a spin-chain with precessing magnetic moments with a fixed phase difference, as shown in Fig. 4.1 a). In the given example, the system oscillates and exhibits a wavelength of five lattice constants. This excitation is called a spin wave or magnon. When the group velocity of the spin wave is non-zero, we can describe this as a phase propagation of precessing moments. In the presence of dipolar interactions, the spin wave propagation is strongly anisotropic, and one distinguishes the two extreme cases where the wave vector and magnetization vectors are parallel (backward volume (BV) mode) or perpendicular (Damon-Eshbach (DE) mode) to each other, viz.  $\mathbf{k} \parallel \mathbf{M}$  and  $\mathbf{k} \perp \mathbf{M}$ . When trying to

observe spin wave propagation one typically chooses the DE configuration, as the group velocity is significantly higher than for BV and thus, the spin wave propagation length is longer [102]. In the quasi-particle picture, the magnons carry spin angular momentum and its transport is called spin current, making spin wave propagation an important element for spintronics [102]. Investigating and understanding the behavior of magnon transport in structured, magnetically ordered systems is therefor indispensable. Microfocused BLS is an efficient way of doing so.

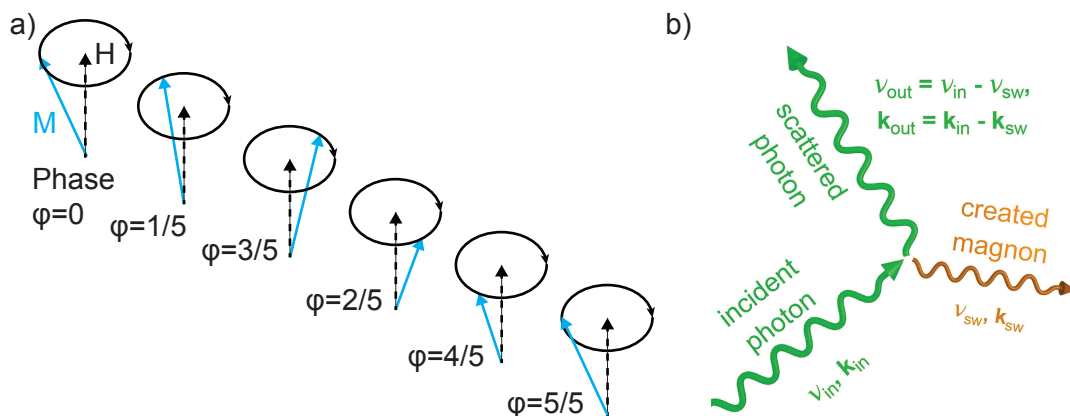


**Figure 4.1:** a) A schematic illustration of the spin wave, or magnon, with a wavelength of five lattice constants. The magnetic moments precess around their ground state alignment, leading to a reduction of the total magnetization. b) A Stokes scattering process. An incident photon scatters inelastically on a magnetically ordered system, losing some of its energy and momentum. The created magnon inherits the transferred quantities. The illustration of the scattering process is taken from [102].

Photons, which scatter off magnons of a magnetically ordered system can exchange energy and momentum with the constraint of total energy and momentum conservation. This results in creation (or annihilation) of magnons which inherit (or provide) the difference of energy and momentum of the incident and scattered photons as shown in Fig. 4.1 b). The important conservation laws are as follows:

$$\begin{aligned}\hbar\nu_{\text{out}} &= \hbar\nu_{\text{in}} \mp \hbar\nu_{\text{sw}} \\ \hbar\mathbf{k}_{\text{out}} &= \hbar\mathbf{k}_{\text{in}} \mp \hbar\mathbf{k}_{\text{sw}}\end{aligned}\quad (4.1)$$

The creation of quasi-particles by photon scattering is called Stokes scattering, whereas the annihilation is called anti-Stokes scattering. Angular momentum conservation also has to be taken into account, which results in a polarization rotation of the scattered photon by  $\pi/2$ . Magnons in FMs live in the GHz spectrum, such that the change in frequency for visible light (THz) is relatively small. It is thus necessary to have a very sensitive apparatus to detect the GHz changes on THz-photons. On the one hand, it requires a monochromatic light beam, which can be attained from a laser with a small linewidth. On the other hand, the demand for a high sensitivity can be achieved by smartly using etalons.

By changing their distance using piezo crystals one can then scan with sub-GHz resolution. The realization is presented in the following.

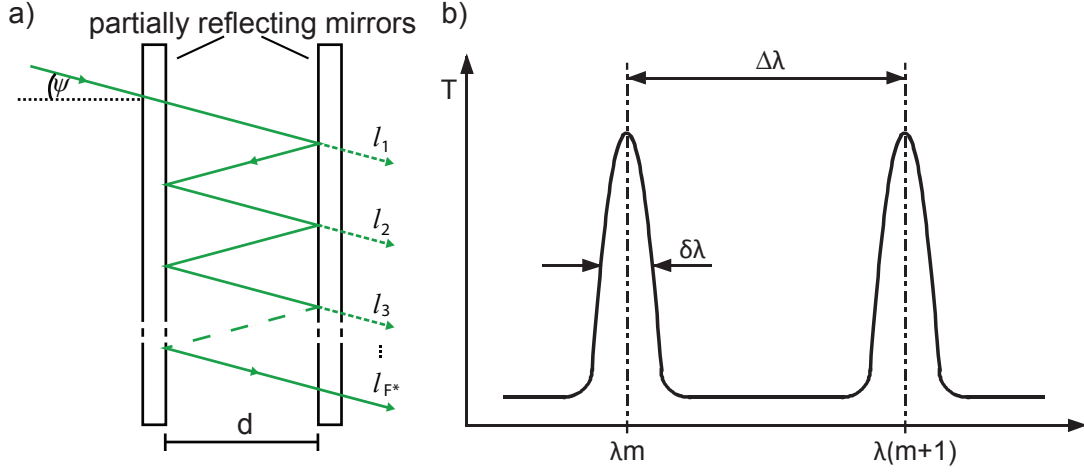


**Figure 4.2:** a) Light enters into a FP and is reflected back and forth by the two semipermeable mirrors. For the illustration a finite angle  $\Psi$  is shown, which is approximately zero in our case. Constructive interference of the leaving rays is reached when the difference in optical distance traveled is an integer multiple of the wavelength. b) The transmission plotted in dependence of the wavelength. The peaks appear, when the wavelength meets the condition for constructive interference. The distance between two peaks  $\Delta\lambda$  is called free spectral range and the width is presented by  $\delta\lambda$ . Their ratio determines the finesse of the mirrors. a) is taken from Clemens Mühlenhoff's master thesis [103] and b) is adapted from [104].

A Fabry-Perot-interferometer (FP) is used for this purpose. It allows transmission only for certain wavelengths. Two semi-transparent mirrors, which have to be accurately aligned with an optical distance  $d$ , form the interferometer. The entered light is reflected back and forth, such that almost all wavelengths are filtered out by destructive interference. An illustration is shown in Fig. 4.2 a). The transmission of a single Fabry Perot interferometer is given by

$$T = \frac{\tau_0}{1 + (4F^2/\pi^2) \sin^2(2\pi d/\lambda)} \quad (4.2)$$

as presented in [104] and plotted in Fig. 4.2 b). The condition of constructive interference, i. e., for transmission, is met when  $\sin^2(2\pi d/\lambda) = 0$  and hence,

$$\lambda = \frac{2d}{m}. \quad (4.3)$$

Here,  $\tau_0$  is the maximum possible transmission,  $F$  stands for the finesse of the mirrors and  $m$  is an integer value. The finesse describes the quality depending on reflectivity and flatness of the mirrors and determines the ratio  $F = \Delta\lambda/\delta\lambda$ , where  $\Delta\lambda$  is also called the free spectral range (FSR), and  $\delta\lambda$  is the linewidth. The FSR can be calculated by the difference

$$\Delta\lambda = \lambda_m - \lambda_{m+1} = \dots = \frac{\lambda_m \cdot \lambda_{m+1}}{2d}. \quad (4.4)$$

It becomes clear, that the FSR can be adjusted by the distance of the mirrors. But one has to have in mind that as linewidth and FSR are connected by the constant finesse, one then trades increased FSR with reduced resolution. In order to analyze the resonant magnetodynamics its frequency linewidth has to be higher than the linewidth given by  $\delta\nu = c/\delta\lambda$ , where  $c$  is the speed of light.

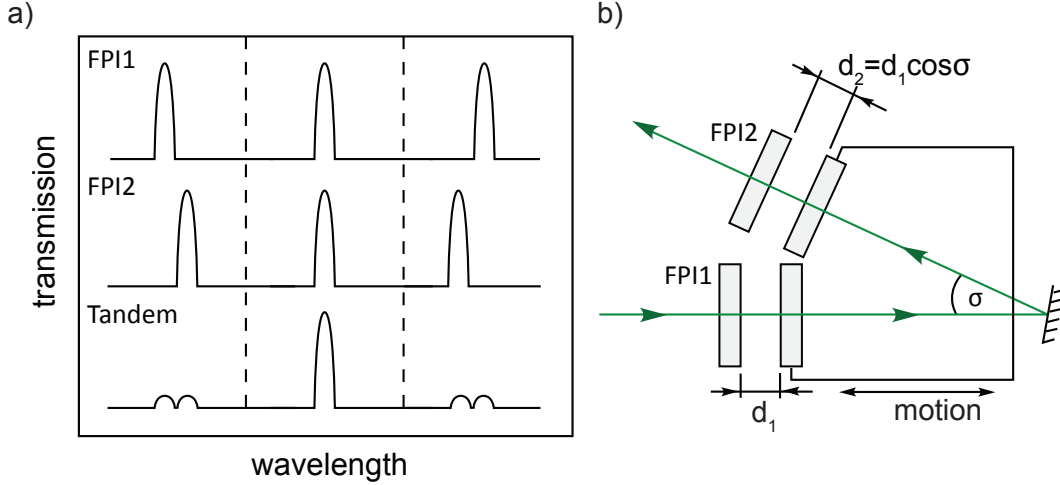


**Figure 4.3:** a) Folding of two FPs, resulting in a TFP. The neighboring peaks of one transmission wavelength become suppressed by the other FP. The FSP is enlarged significantly. b) Sketch of the Sandercock-type TFP. The light beam enters one FP and is reflected by a mirror to a second etalon. One mirror of each pair is placed on a movable stage, such that the distance ratio of both FPs stays the same for every position. The pictures are taken and adapted from [103, 104].

One option to increase the FSR and simultaneously maintaining the resolution is achieved by using a so called tandem-Fabry-Perot interferometer (TFP) [104]. In this approach, the light passes through two FPs (FP1 and FP2) with slightly different mirror distances. Due to Eq. (4.4) we know that the FSRs of FP1 and FP2 do not match. The transmitted wavelength then has to fulfill two conditions, one for  $d_1$  ( $\lambda_p$ ) and one for  $d_2$  ( $\lambda_q$ ), as shown in Fig. 4.3 a). Both wavelengths have to be equal and we can write

$$\frac{2d_1}{p} = \frac{2d_2}{q}. \quad (4.5)$$

This results in a fixed relation between  $d_1$  and  $d_2$ . Neighbouring transmission peaks of each FP are suppressed. Due to Eq. (4.5), we can easily see that the ratio of the distances mustn't change, when scanning through different frequency by moving the mirror distances  $d_1$  and  $d_2$ . The Sandercock-TFP solves this condition by only moving one mirror of each FP. The schematic setup is shown in Fig. 4.3 b), where the light is reflected with an angle  $\sigma$  and sent through the second FP. By moving the stage, the distances change but their ratio stays the same with  $d_1/d_2 = 1/\cos(\sigma)$ . The sensitivity is increased by implementing more mirrors before and after the FPs, such that the light beam passes each etalon three times. Thus, the transmission line is a sixfold folding of the transmission given in Eq. (4.2).

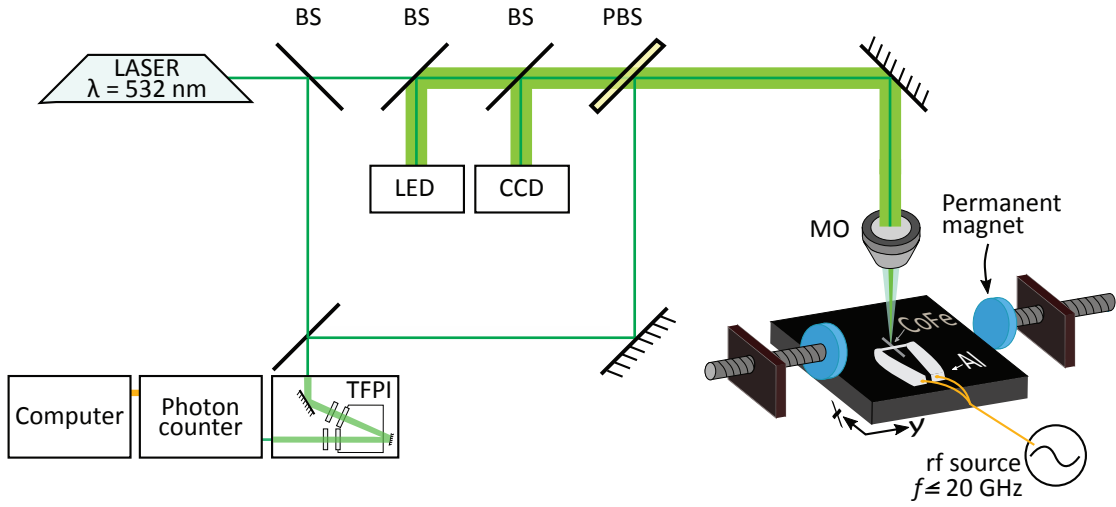


**Figure 4.4:** Experimental Setup. A monochromatic laser is used, whose beam is split right at the beginning. A part is used to stabilize the TFP and to avoid drift. A LED adds light for a camera and the whole light bundle is polarized by a PBS. A microscope objective focused the beam on the sample and also collects the reflected and scattered light. The PBS then filters the photons which scattered on magnons due to a phase shift. The rest of the light is sent to the camera to visualize the sample and the laser spot position. The scattered photons are sent through the TFP, which scans for different frequencies by moving the mirror stage with some piezo crystals. A photon counter collects the corresponding light particles and a computer processes the data. The sketch is adapted from [103].

The employed experimental setup is sketched in Fig. 4.4 and will be explained in the following. A monochromatic laser with a wavelength of  $\lambda = 532 \text{ nm}$  with a linewidth smaller than  $10 \text{ MHz}$  is used as a photon source. The first beam splitter (BS) feeds an undisturbed part of the light into the TFP, which acts as a reference signal for stabilization. The light is then polarized by a polarizing beam splitter (PBS) and sent through a microscope objective with a numerical aperture (NA) of 0.75. Thus, the spatial resolution of our micro focused BLS spectrometer is

$$\Delta x = \frac{0.61\lambda}{NA} = 433 \text{ nm}. \quad (4.6)$$

The momentum component parallel to the surface has to be conserved during the scattering event. Hence, the maximum magnon  $k$ -vector is restricted by two times the maximum  $k$ -vector of the incident light, which depends on the objective used. In our case it is  $k_{\text{magnon,max}} = 4\pi NA/\lambda \approx 24 \mu\text{m}^{-1}$  [103]. Spin waves with  $|k_{\text{magnon}}| < |k_{\text{magnon,max}}|$  can be detected by microfocused BLS, but the setup is otherwise not sensitive to the magnon wave vector. Light that is scattered by magnons undergoes a polarization rotation of  $\pi/2$  due to angular momentum conservation. The reflected and backscattered passes through the lens again and is separated by the PBS. Only the scattered photons (which experienced the polarization rotation) are sent towards the TFP. An additional LED and a CCD camera are installed to observe the laser spot on the sample. The TFP is of Sandercock type described above, with additional mirrors to increase sensitivity by multiple passing through the TFP. The finesse of the installed mirrors lies between  $F = 80$  and  $F = 120$ . Directly

behind the TFP, a photon counter is installed and connected to a computer to process the data. With the employed configuration for our BLS setup we can spatially resolve the spin wave intensities but not their phase. The sample itself is mounted on a movable stage, which is controlled by piezo actuators. The total movable area covers a  $100 \times 100 \mu\text{m}^2$  field. By the visible feedback of the camera, the laser spot can be placed on the desired position on the sample. The external magnetic field is applied by two permanent magnets fixed to a stepper motor. The field strength depends on the distance of the magnets and is calibrated with a Hall probe. Field sweeps can then be realized by adjusting the separation of the permanent magnets.

## 4.2 Experimental Results

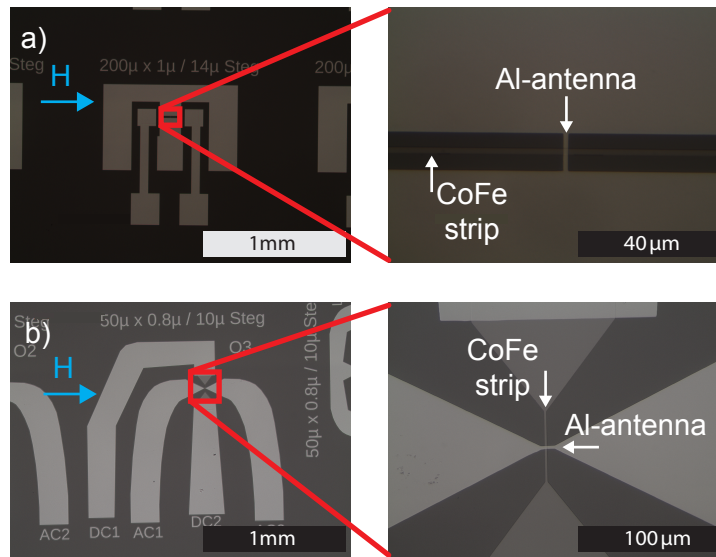


**Figure 4.5:** Micrographs of the two investigated BLS samples. a) shows the first structure with a  $2 \mu\text{m}$  wide  $\text{Co}_{25}\text{Fe}_{75}$  strip in a "PCFT-S-001"-like ( $5 \text{ nm } \text{Co}_{25}\text{Fe}_{75}$ ) multilayer and its closeup. The  $50 \text{ nm}$  thick Al antenna and contact pads are deposited on top of the strip. We have three ac-contact pads for the antenna and two dc-contact pads for a possible bias current in the strip. During this work only ac current was applied. This sample was used to see whether we can reproduce the magnetic properties from our blanket film FMR measurements. The picture in b) shows the second sample which has the same multilayer sequence but a nominally  $10 \text{ nm}$  thick FM layer and the inset presents a closeup. The contact pads were optimized for the microwave transport and the geometry was changed, such that the magnetic field now is perpendicular to the magnetic strip (Damon-Eshbach configuration). This geometry was chosen for the spin wave propagation experiment.

The investigated samples were fabricated using the optical lithography and sputter deposition steps described in Chapter 2. A micrograph of the first sample is seen in Fig. 4.5 a). The two outer and the inner contact pads are for the Al antenna, whereas the longer contact pads were added for possible dc-bias current in the  $\text{Co}_{25}\text{Fe}_{75}$ -strip. The measurements realized in this work were performed without any dc-current, such that the corresponding contact pads are of no relevance here. The closeup in a) shows the  $2 \mu\text{m}$

wide  $\text{Co}_{25}\text{Fe}_{75}$ -strip. For this sample, the deposited stack sequence was configured to have  $3\text{Pt}/3\text{Cu}/5\text{Co}_{25}\text{Fe}_{75}/3\text{Cu}/3\text{Ta}$ , i. e., analogous to the "PCFT-S-001" sample presented in Fig. 3.8. On top of the multilayer strip, we deposited 50 nm Al for the antenna and the contact pads. The magnetic field lies IP in the direction of the strip. This corresponds for the backward volume (BV) mode of dipolar spin waves propagating along the  $\text{Co}_{25}\text{Fe}_{75}$  strip. These spin waves have rather small group velocities, such that we dominantly observe the FMR signal excited by the antenna. The microwave magnetic field induced by the ac current in the antenna decays with a lengthscale comparable to the antennas width (see Eq. (3.18)), such that the laser spot was placed on the  $\text{Co}_{25}\text{Fe}_{75}$  strip, in direct vicinity to the antenna.

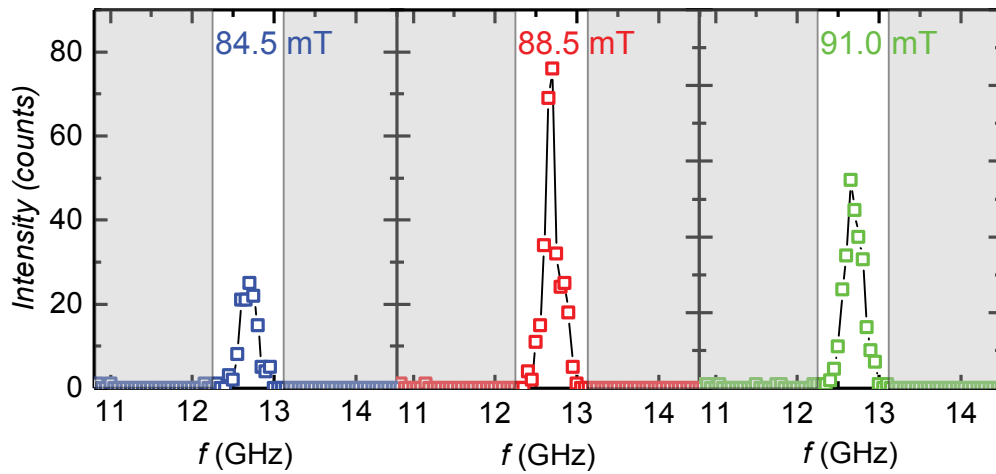


**Figure 4.6:** The BLS intensity for the "PCFT-S-001"-like sample for three different magnetic fields and a microwave frequency of 13 GHz. The peak seen is not perfectly centered over 13 GHz due to unavoidable calibration uncertainties of the BLS setup. Photons which scatter at magnons and absorb their energy experience a positive shift in frequency corresponding to the magnon frequency. When coming close to the resonance condition, the antenna drives the FMR signal providing magnons for the scattering, which leads to an increased BLS peak height. The resonance magnetic field is identified by the highest BLS signal.

The light scattered from the  $\text{Co}_{25}\text{Fe}_{75}$  strip enters the TFP. By counting the photons incident on the photodetector (see Fig. 4.4) as a function of the TFP mirror separation we obtain Data shown as in Fig. 4.6. Here, the ac-current was set to a frequency of 13 GHz, such that we see the expected anti-Stokes peak in the indicated region of interest (ROI) of the figure. For fixed frequency, we swept the magnetic field and extracted the total sum of counts in the corresponding ROI. To extract the resonance position this data is fit to a Lorentzian-shaped peak which is shown in Fig. 4.7.

Similar field sweeps were carried out for several ac-frequencies ranging from 13 - 7.2 GHz. The resulting resonance parameters for our structured "PCFT-S"-like are shown in Fig. 4.8 together with in-plane FMR data obtained from a nominally identical blanket film. The IP-Kittel behavior is reproduced and matches the blanket film results almost perfectly (see

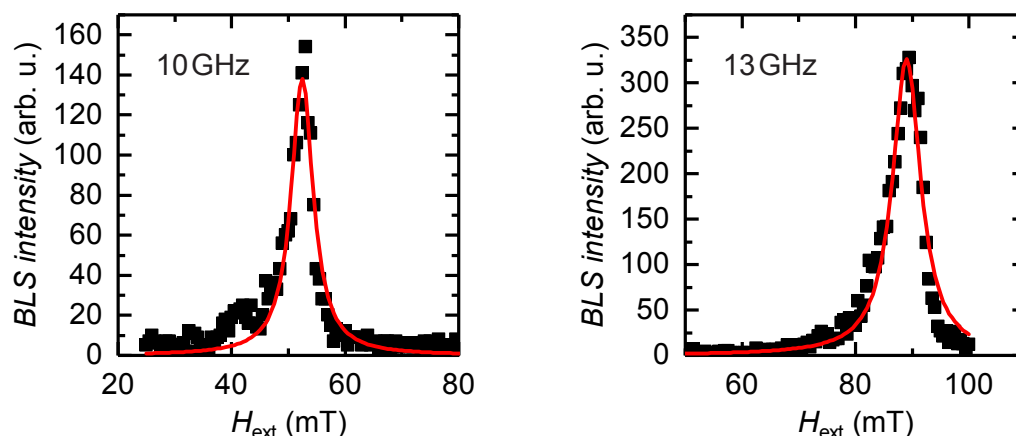


**Figure 4.7:** The sum of the anit-Stokes peak counts from Fig. 4.6 is plotted vs. the applied magnetic field. The field sweeps were performed at different frequencies, such that each corresponding resonance field and linewidth were extracted from a Lorentzian fit. The frequency dependency is shown in Fig. 4.8.

panel a)), indicating that the patterning only results in weak in-plane shape anisotropy. Moreover, the linewidth extracted from the BLS measurement also agrees well with the FMR data, such that the total damping of our blanket films and structured samples coincides very well for the investigated frequency range. Hence, we can successfully structure our samples with optical lithography without altering their relevant magnetic properties. In the following, we discuss the spin wave propagation in patterned  $\text{Co}_{25}\text{Fe}_{75}$  devices.

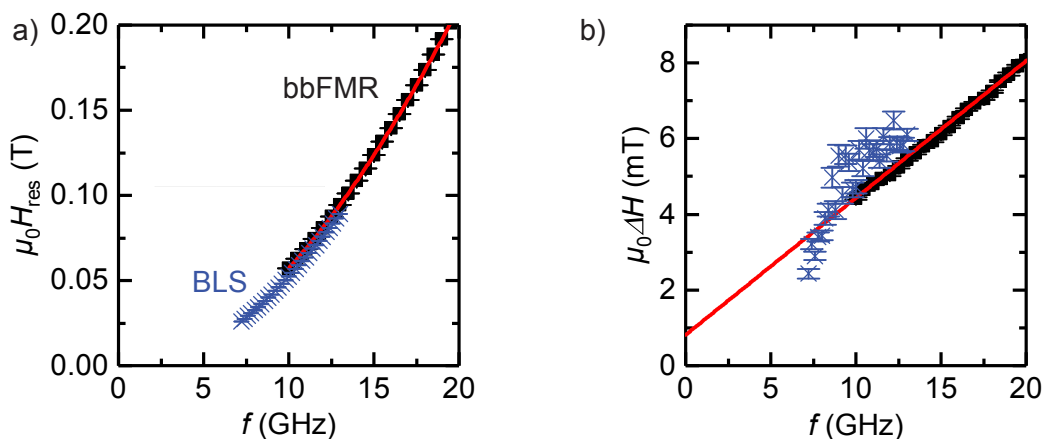


**Figure 4.8:** Comparison of the blanket film FMR data ("PCFT-S-001") and the obtained results from the corresponding structured sample in the BLS experiment. In a) the resonance position can be seen, which matches almost perfectly the blanket film results. The linewidth in b) is also very close to the blanket film values, even though a linear behavior is not extractable. The coinciding values of the saturation magnetization and the total damping show, that we can assume the same magnetic properties for structured samples as for blanket films.

For the propagation measurement, we optimized the sample, geometry and FM thickness. In order to reduce the damping, we increased the FM layer from 5 nm to nominally

10 nm (the blanket film magnetic properties can be seen in Fig. 3.9). We again structured a  $\text{Co}_{25}\text{Fe}_{75}$ -strip with the "PCFT-S" multilayer, and adapted the Al contact pads. Figure 4.5 b) and its closeup show the contact pads and the strip with the antenna on top, respectively.

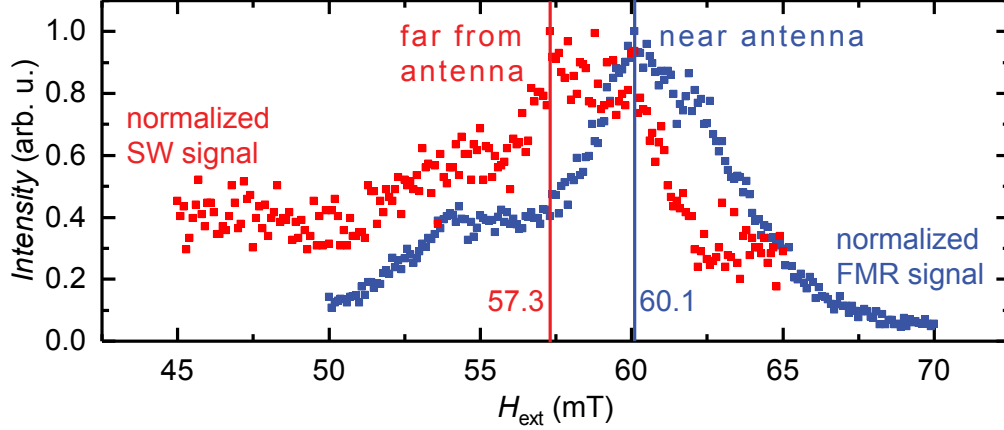


**Figure 4.9:** The magnetic resonance field shifts to lower values when increasing the k-vector. At  $k = 0$ , i. e., the FMR signal, we see a maximum intensity at 60.1 mT at a microwave excitation frequency of 10 GHz. When performing the magnetic field sweep about  $8 \mu\text{m}$  away from the antenna we only detect spin waves. The SW resonance field was chosen to be the maximum intensity value and the furthest away from the FMR signal resulting in 57.3 mT. Thus, when scanning over the strip near the antenna, the FMR signal contribution is as low as possible.

As we want to observe spin wave (SW) propagation, we take advantage of the high group velocities in the Damon-Eshbach configuration, i. e., IP magnetic field perpendicular to the strip direction. In order to excite traveling SWs, we fixed the microwave excitation frequency at 10 GHz and set the laser spot about  $8 \mu\text{m}$  away from the antenna. At this distance to the antenna, the FMR signal due to far-field excitation by the antenna is below our sensitivity limit. A magnetic field sweep was performed to find the resonance condition for SW excitation. In Fig. 4.9 the normalized BLS Intensity for two magnetic field sweeps near and far from the antenna are depicted. At the SW resonance magnetic field, we then scanned the laser spot over the  $\text{Co}_{25}\text{Fe}_{75}$  strip to record the BLS intensity as a function of x and y coordinates. The SW resonance field was chosen to be the maximum intensity the furthest away from the FMR peak. Thus, by scanning over the strip near the antenna the FMR signal is lowered. For each laser spot position the photon counts in the Anti-stokes peak were summed and are presented in Fig. 4.10 a). Here, the antenna crosses the strip at  $y = 0$ .

We detect spin waves up to  $15 \mu\text{m}$  away from the antenna. Even though our antenna excites magnons with many different k vectors (sinc function in k-space) an overall attenuation length scale  $\lambda_{\text{prop}}$  can be approximated. To extract the spin wave propagation length, we integrate data in Fig. 4.10 a) along the x-direction. The resulting integrated BLS signal is shown in Fig. 4.10 b). The data is fitted to an exponential equation

$$I \propto \exp(-2y/\lambda_{\text{prop}}) \quad (4.7)$$

for spin waves propagating to the left/right of the antenna, analogous to Ref. [105]. Here,  $I$  accounts for the signal intensity and  $\lambda_{\text{prop}}$  represents the attenuation length scale. In panel b) we see that the decay is not perfectly exponential. We assume that this stems from spin wave interference due to the excitation of spin waves with a range of k-vectors by our microstrip antenna. The extracted attenuation length scale is  $\lambda_{\text{prop}} \approx (5.67 \pm 0.2) \mu\text{m}$ . In order to achieve a more linear decay on the logarithmic scale in future experiments it is possible to modify the antenna. The sinc function could be partly imitated by the antenna in real space, making one central antenna line, and thinner antenna lines on each side. In k-space we thus would excite magnons with a more defined k-vector. Another observation made by the presented data is the non-reciprocity of the signal intensity on both sides of the antenna. One idea to explain this behavior is the influence of the Dzyaloshinskii-Moriya interaction, which favors one propagation direction and was investigated by Nembach *et al.* in 2015 [106]. Bailleul *et al.* present an alternative explanation for the non-reciprocal feature. They argue that the DE wave is a surface wave located either on the upper or down side of the strip. As the antenna is on top of the strip, depending on the relative direction of the magnetic field one polarity is favored for the excitation [107].

We compare the Gilbert-damping obtained from the blanket film measurement and the resulting, expected attenuation length scale with the BLS data by using the spin dispersion relation described by Kalinikos and Slavin [108], and simplifying it as in Ref. [109]:

$$\omega_{\text{res}} = \gamma\mu_0 \sqrt{\left(H_{\text{ext}} + Jk^2 + M_s \left(1 - \frac{kd}{2}\right)\right) \cdot \left(H_{\text{ext}} + Jk^2 + \frac{M_s kd}{2}\right)}. \quad (4.8)$$

Here,  $J = 2A/\mu_0 M_s$  with the exchange stiffness constant  $A$ , the k-vector  $k$  and the FM-layer thickness  $d$ . According to the rectangular shape of our antenna the Fourier transform returns a dominant k-vector of the excited magnons of  $k = \pi/w \approx 1.6 \mu\text{m}^{-1}$ , where the antenna width is  $w = 2 \mu\text{m}$ . This small wave vector allows us to neglect exchange interactions [109], hence we set  $A = 0$  to simplify Eq. (4.8). From this dispersion relation we can extract the group velocity by

$$v_g = \frac{\partial \omega_{\text{res}}}{\partial k} = (\gamma\mu_0)^2 \frac{M_s^2 d \cdot (dk - 1)}{4\omega_{\text{res}}}, \quad (4.9)$$

evaluated at 10 GHz and the calculated k-vector. The needed magnetic parameters are taken from the FMR blanket film experiment (see Fig. 3.9). We obtain a group velocity of roughly 4.6 km/s, which is close to the velocity in single crystal iron films [110] and more than twice as high as in Permalloy [111]. By using two simple relations,  $\tau = 1/(\omega\alpha)$ , with life time  $\tau$  and  $\lambda_{\text{prop}} = v_g \cdot \tau$  we estimate the expected  $\lambda_{\text{prop}}$  from our blanket film. Using  $\alpha = 4.6 \times 10^{-3}$ , we obtain  $\lambda_{\text{prop}} \approx 16 \mu\text{m}$ , which is almost a factor three higher than our BLS-results. Even when we take the effective Gilbert parameter, i. e., assuming no inhomogeneous linewidth broadening, our  $\alpha_{\text{eff}} = 6.5 \times 10^{-3}$  results in  $\lambda_{\text{prop}} \approx 11.3 \mu\text{m}$ , which is two times higher than our measurement result. From our data in Fig. 4.10 b) we see small areas, where our slope is smaller, i. e., the attenuation length scale is higher, than the indicated fit shows. As we excite a range of k-vectors with our antenna geometry it is desirable to improve the antenna in order to excite only certain k-vectors. The small

areas with a higher attenuation scale hint towards the existence of k-vectors where the damping is lower. A similar variation can be seen in Körner's *et al.* work, where they investigated a 10 nm  $\text{Co}_{25}\text{Fe}_{75}$  strip with a time-resolved MOKE experiment [112]. It returns comparable attenuation length scales of  $5\ \mu\text{m} - 8\ \mu\text{m}$ . The authors also found slightly varying  $\lambda_{\text{prop}}$ , by applying different microwave excitation frequencies. Comparing FMR and MOKE experiment they report of a discrepancy of a factor 2.5 for the damping, which is comparable to our difference factor in the attenuation length scale. It is surprising though, that we observe a comparable  $\lambda_{\text{prop}}$  because we use a Pt and Ta seed and cap layer respectively. In their work [112], Körner *et al.* fabricated  $\text{Co}_{25}\text{Fe}_{75}$  on a MgO seed layer, omitting spin pumping. Thus, further investigations on our  $\text{Co}_{25}\text{Fe}_{75}$  multilayers are necessary as our data indicate the possibility to obtain even higher attenuation length scales, even though spin pumping is present.

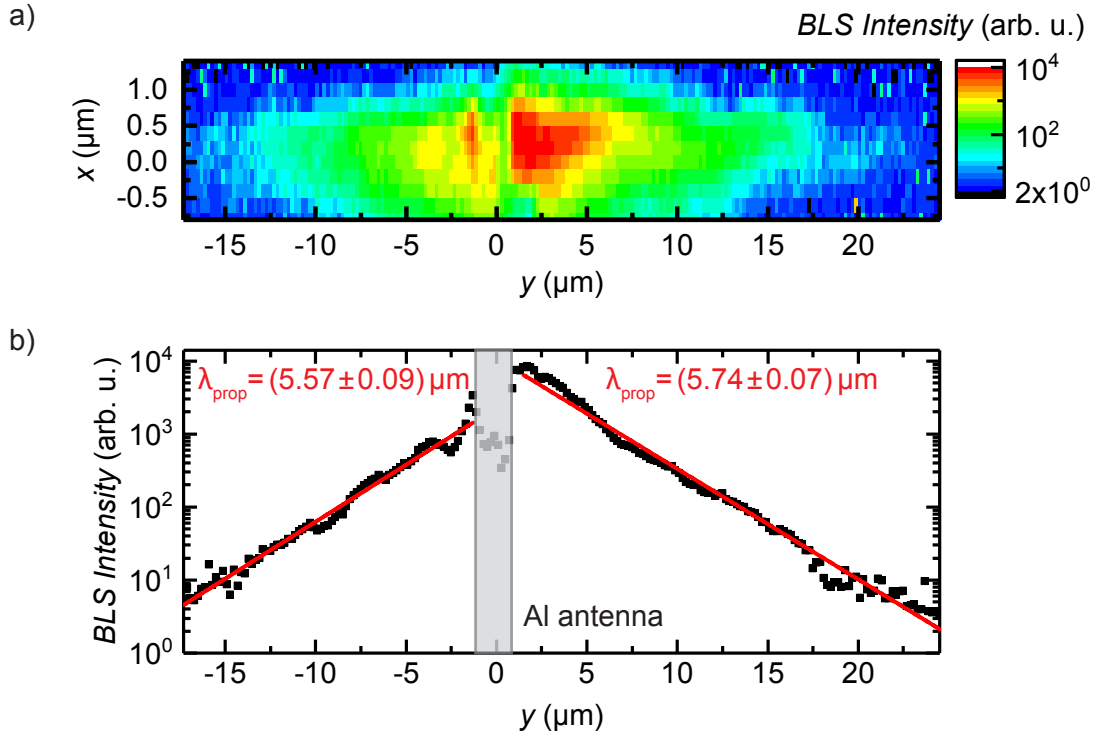


**Figure 4.10:** a) 2D-Scan of the  $\text{Co}_{25}\text{Fe}_{75}$  strip showing the spin wave intensity vs. the position on the strip. b) shows a linear cut through the x-axis averaging between  $x = 0\ \mu\text{m}$  and  $x = 0.6\ \mu\text{m}$ . By fitting the exponential decay we obtain the presented attenuation length scales on the left and right, respectively.



# Chapter 5

## Summary and Outlook

During this thesis, the fabrication and characterization of thin-film heterostructures based on ferromagnetic  $\text{Co}_{25}\text{Fe}_{75}$  was realized. The first part concentrated on the deposition of blanket film multilayers and their characterization by broadband FMR. As a second step, structured samples were fabricated and analyzed with BLS. Herefore, a spin coating process and an exposure series for the new laser writing machine was elaborated. The most important results are recapitulated in the following.

**Blanket Films Characterized with FMR** The obtained sputtering cluster at WMI allows fast fabrication of samples embedding a variety of materials. Due to the ultra-low, intrinsic magnetic damping in  $\text{Co}_{25}\text{Fe}_{75}$  [8], this work focused on systematically depositing  $\text{Co}_{25}\text{Fe}_{75}$  layers in different heterostructures. We fabricated a large number of samples with varying thickness of the FM layer and the adjacent materials. The systematic characterization via broadband FMR acquired some new and interesting insights. The record low damping parameter of  $\alpha_{\text{max}} = 1.8 \times 10^{-4}$  for metallic ferromagnets in our  $\text{Co}_{25}\text{Fe}_{75}$  samples renders this alloy into a highly interesting material for magnonic applications. This value breaks the recent damping records for ferromagnetic metals [8, 97, 98]. As the extrapolated Gilbert parameter in bulk material varies for the different stack sequences, we conclude a major influence of the growth condition introduced by the seed layers on the magnetodynamic relaxation.

We investigated the magnetic anisotropies for the different interfaces. The results indicate the possibility to obtain PMA in  $\text{Co}_{25}\text{Fe}_{75}$ , which is relevant for the creation of skyrmions. Unpublished internal experiments by Matthias Althammer proved this conclusion to be correct. Further research at the WMI will concentrate on investigating this interfacial PMA and the creation of skyrmions in a low damping material.

The extrapolated saturation magnetization in our samples reaches the expected bulk values. As the values stay fairly constant, the data show that the FM magnetization is robust against any effects introduced by the adjacent layers. The anisotropy of the  $g$ -factor in our Ta/Cu/ $\text{Co}_{25}\text{Fe}_{75}$ /Cu/Ta series returns the same qualitative results as literature [78]. Together these two parameters, which behave as expected hint towards an excellent sample quality.

We measured the spin-pumping effect and quantified the effective spin mixing conductance for our four sample series. Again the obtained values are comparable to established literature results, confirming the good interfacial quality of our samples. The spin pumping effect was

shown to be geometry dependent in the Ta/Cu/Co<sub>25</sub>Fe<sub>75</sub>/Cu/Ta series. Up to now, this dependency has not been observed in literature and thus encourages further investigation. The high spin-pumping contribution by using Pt as an adjacent metal renders these heterostructures fairly compelling for spintronic applications like, e. g. spin-orbit torques.

**Structured Samples Studied with BLS** In real spintronic and magnonic devices the samples have to be structured in the micron or even sub-micron range. The new laser writing machine in the clean room enables us to easily fabricate structured samples, as no masks nor vacuum is needed. For this optical lithography, a new spin coating process and an exposure recipe was developed systematically within this thesis.

We checked whether our Co<sub>25</sub>Fe<sub>75</sub> stacks maintain their magnetic properties by micropatterning using optical FMR and the obtained data show that indeed the quality of the samples is not influenced by the patterning process. The high saturation magnetization of Co<sub>25</sub>Fe<sub>75</sub> leads to high magnon group velocities and thus, makes it an ideal material system for magnonic applications. For the first time, we investigated the spin wave propagation length with BLS and obtained values above 5.5  $\mu\text{m}$ . These intriguing properties extracted from our measurements proof for the first time that Co<sub>25</sub>Fe<sub>75</sub> thin films are an ideal candidate for future and pave the way for novel functionalities.

**Outlook** For magnonic and spintronic devices the magnetodynamic damping is a crucial parameter determining whether these technologies are competitive to already established, electronic based technologies [113]. Most relevant applications are directly connected to the transport of information via spin waves or spin currents. Not only the life time of a spin wave, which is enhanced for low magnetodynamic damping, but also the group velocity of the magnons determine their propagation length. A large group velocity is achieved by using materials with high saturation magnetizations like Co<sub>25</sub>Fe<sub>75</sub>. By reaching several, or one day even tens of, micrometers of length scales, maybe one day we see magnonic integrated circuits, which process and transport information on the circuit using magnetic signals. That way Joule heating is reduced significantly, reducing power consumption on a high level. Cooling devices and the huge space needed for heat transport would be diminished drastically. By using e. g. spin pumping and the spin-Hall effect one could then transport the processed data over larger lengthscales. The microwave magnetodynamic signals can be excited with different approaches. One example would be using spin-Hall nano-oscillators (SHNO).

A dc current in a material with a high spin-Hall angle injects a spin current into an adjacent magnetic layer. By spin-orbit torques (SOT) or/and spin transfer torque (STT), the spin system can be excited resulting in magnetic auto-oscillations. Up to now, the needed current densities are very high, i. e., in the order of  $\approx 10^8 \text{ Acm}^{-1}$  [7, 9, 91]. In these systems, the damping term has to be compensated by SOT or STT. When the damping is reduced, we benefit from lower electric current densities, which increase the life time and the power consumption of the devices. Using Py as a FM, nanoconstrictions are fabricated to obtain such high current densities. It happens very easily that the constriction is melt down by the Joule heating during an experiment, making large scale industrial applications

---

rather difficult. The situation changes when we can fabricate ultra-low damping materials on large scales. As the deposition method, presented in this thesis, is a very uncomplicated fast way of sample fabrication, and we are able to observe very low damping, we are approaching the idea of technological employment. The results from this work encourage to realize SHNO experiments, as we presented an uncomplicated fabrication of polycrystalline  $\text{Co}_{25}\text{Fe}_{75}$  with promising magnetic properties. Also phase locking experiments coupling several oscillators to each other in order to increase the microwave power as investigated by Awad *et al.* [114] are thinkable.

As the FMR experiments indicate, by growing thin  $\text{Co}_{25}\text{Fe}_{75}$  layers, the PMA can compensate the shape anisotropy. FM layers with adjacent heavy metals have been shown to exhibit skyrmion formation even at room temperature [115]. As the two anisotropies compensate, the Dzyaloshinskii-Moriya interaction can become nearly as large as the Heisenberg exchange. Indeed, internal unpublished experiments from Matthias Althammer show, that we can grow  $\text{Co}_{25}\text{Fe}_{75}$  heterostructures fulfilling the given conditions. Skyrmions are spin textures, which are highly interesting due to possible application in data storage and processing. Most important, the spin vortices behave like particles [116] and are topologically stable, which allows them to exist as solitons. As this work proposes,  $\text{Co}_{25}\text{Fe}_{75}$  can become a technologically relevant FM, and the creation and properties of skyrmions at  $\text{Co}_{25}\text{Fe}_{75}$ /heavy metal interfaces should be investigated. To go even a step further, skyrmion dynamics can be investigated in these materials. Coupling of ferromagnetic dynamics with skyrmion dynamics could be exploited, which is currently only poorly investigated. Using our fabrication techniques, this can be realized using the low damping metal  $\text{Co}_{25}\text{Fe}_{75}$  as ferromagnet and quite possibly also the skyrmionic material by carefully tuning the growth conditions.

In conclusion, this work shows that  $\text{Co}_{25}\text{Fe}_{75}$  thin-films are an intriguing material system. Its properties directly enable studies of current interest in the field of spintronics and magnonics. Thus, this thesis may be understood as a starting point for upcoming exciting results obtained with  $\text{Co}_{25}\text{Fe}_{75}$  thin films.



# Appendix A

## Sputter Deposition Parameters

This appendix will present the used sputter parameters for the sample fabrication. Table A.1 lists blanket films for FMR measurements and table A.2 lists lithographically structured samples.

**Table A.1:** Deposition parameters for blanket film samples used for FMR measurements. The substrate was SiO<sub>2</sub><sup>1</sup>. Deposition was performed at room temperature.

Name	Material	Pressure (10 <sup>-3</sup> mbar)	Power (W)	Rate (Å/s)	Time (s)
1	Ta	1.3	30	1	50
	CoFe	0.6	70	2	75
	Ta	0.8	30	1	50
7	Ta	1.3	30	1	50
	CoFe	0.6	70	2	50
	Ta	1.3	30	1	50
Goldfinger	Ta	1.3	30	0.9	56
	CoFe	0.6	70	1.9	27
	Ta	1.3	30	0.9	56
MI 6	Ta	1.3	30	1	50
	CoFe	0.6	70	2	10
	Ta	1.3	30	1	50
PCT 270717	Pt	1.3	30	1	50
	Co	1	70	0.5	24
	Ta	1.3	30	1	50
PCT 280717	Pt	1.3	30	1	50
	Co	1.3	70	0.5	40
	Ta	1.3	30	1	50
PCT 310717	Pt	1.3	30	0.98	51
	Co	1	70	0.5	16
	Ta	1.3	30	1	50

<sup>1</sup>Except for "MCFT" samples. Here, MgO substrates instead of SiO<sub>2</sub> were used. The "cold" sample was deposited at room temperature, whereas "hot" was sputtered at 200°C.

Name	Material	Pressure (10 <sup>-3</sup> mbar)	Power (W)	Rate (Å/s)	Time (s)
MCFT cold	CoFe	0.6	70	2	100
	Ta	1.3	30	1	25
MCFT hot	CoFe	0.6	70	2	100
	Ta	1.3	30	1	25
CoFe-Al	CoFe	1	70	2	25
	Al	5	30	1.5	27
SiCoFA 001	CoFe	1	70	2	50
	Al	5	30	1.5	27
SiCoFA 002	CoFe	1	70	2	35
	Al	5	30	1.5	27
SiCoFA 003	CoFe	1	70	2	25
	Al	5	30	1.5	27
SiCoFA 004	CoFe	1	70	2	15
	Al	5	30	1.5	27
SiCoFA 005	CoFe	1	30	0.95	74
	Al	5	30	1.5	27
SiCoFA 006	CoFe	1	30	0.95	53
	Al	5	30	1.5	27
PCFT 001	Pt	5	30	1	50
	CoFe	5	30	0.89	40
	Ta	5	30	1	35
PCFT 002	Pt	5	30	1	50
	CoFe	5	30	0.89	40
	Ta	5	30	1	35
PCFT 003	Pt	5	30	1	30
	CoFe	5	30	0.89	28
	Ta	5	30	1	30
PCFT 004	Pt	5	30	1	30
	CoFe	5	30	0.89	23
	Ta	5	30	1	30
PCFT 005	Pt	5	30	2	30
	CoFe	5	30	0.89	11
	Ta	5	30	1	30
PCFT 006	Pt	5	30	1	30
	CoFe	5	30	0.89	22
	Ta	5	30	1	30

Name	Material	Pressure (10 <sup>-3</sup> mbar)	Power (W)	Rate (Å/s)	Time (s)
PCFT 007	Pt	5	30	1	30
	CoFe	5	30	0.89	22
	Ta	5	30	1	30
PCFT 008	Pt	5	30	1	30
	CoFe	5	25	0.4	75
	Ta	5	30	1	30
PCFT 009	Pt	5	30	1	30
	CoFe	5	25	0.4	125
	Ta	5	30	1	30
PCFT 010	Pt	5	30	1	30
	CoFe	5	25	0.4	250
	Ta	5	30	1	30
PCFT 011	Pt	5	30	1	10
	CoFe	5	25	0.4	125
	Ta	5	30	1	30
PCFT 012	Pt	5	30	1	10
	CoFe	5	25	0.4	75
	Ta	5	30	1	30
PCFT 013	Pt	5	30	1	10
	CoFe	5	25	0.4	50
	Ta	5	30	1	30
PCFT 014	Pt	5	-	0	10
	CoFe	5	25	0.4	125
	Ta	5	30	1	30
PCFT 015	Pt	5	-	0	10
	CoFe	5	25	0.4	75
	Ta	5	30	1	30
PCFT 016	Pt	5	-	0	10
	CoFe	5	25	0.4	50
	Ta	5	30	1	30
PCFT 017	Pt	5	30	1	30
	CoFe	5	25	0.4	50
	Ta	5	30	1	30
PCFT 018	Pt	5	30	1	30
	CoFe	5	25	0.4	63
	Ta	5	30	1	30
PCFT 019	Pt	5	30	1	30
	CoFe	5	25	0.4	93
	Pt	5	30	1	30

Name	Material	Pressure (10 <sup>-3</sup> mbar)	Power (W)	Rate (Å/s)	Time (s)
PCFT 020	Pt	5	30	1	30
	CoFe	5	25	0.4	93
	Ta	5	30	1	30
PCFT 021	Pt	5	30	1	30
	CoFe	5	25	0.4	188
	Ta	5	30	1	30
PCFT 022	Pt	5	30	1	30
	CoFe	5	25	0.4	125
	Ta	5	30	1	30
PCFT 023	Pt	5	30	1	30
	CoFe	5	25	0.4	125
	Ta	5	30	1	30
PCFT 024	Al	5	30	1	30
	CoFe	5	25	0.4	125
	Ta	5	30	1	30
PCFT 025	Pt	5	30	1	30
	CoFe	5	25	0.4	125
	Al	5	30	1	30
PCFT 026	Al	5	30	1	30
	CoFe	5	25	0.4	125
	Al	5	30	1	30
PCFT 027	Ta	5	30	1	30
	CoFe	5	25	0.4	125
	Pt	5	30	1	30
Schoen 001	Ta	5	30	1	30
	Al	5	30	1	30
	CoFe	5	25	0.4	250
	Al	5	30	1	30
	Ta	5	30	1	30
Schoen 002	Ta	5	30	1	30
	Al	5	30	1	30
	CoFe	5	25	0.4	125
	Al	5	30	1	30
	Ta	5	30	1	30
Schoen 003	Ta	5	30	1	30
	Al	5	30	1	30
	CoFe	5	25	0.4	75
	Al	5	30	1	30
	Ta	5	30	1	30

Name	Material	Pressure (10 <sup>-3</sup> mbar)	Power (W)	Rate (Å/s)	Time (s)
Schoen 004	Ta	5	30	1	30
	Cu	5	25	2	15
	CoFe	5	25	0.4	250
	Cu	5	25	2	15
	Ta	5	30	1	30
Schoen 005	Ta	5	30	1	30
	Cu	5	25	2	15
	CoFe	5	25	0.4	125
	Cu	5	25	2	15
	Ta	5	30	1	30
Schoen 006	Ta	5	30	1	30
	Cu	5	25	2	15
	CoFe	5	25	0.4	83
	Cu	5	25	2	15
	Ta	5	30	1	30
Schoen 007	Ta	5	30	1	30
	Cu	5	25	2	15
	CoFe	5	25	0.4	63
	Cu	5	25	2	15
	Ta	5	30	1	30
Schoen 008	Ta	5	30	1	30
	Cu	5	25	2	15
	CoFe	5	25	0.4	50
	Cu	5	25	2	15
	Ta	5	30	1	30
PCFT-S-001	Pt	5	30	1	30
	Cu	5	25	2	15
	CoFe	5	25	0.4	125
	Cu	5	25	2	15
	Ta	5	30	1	30
PCFT-S-002	Pt	5	30	1	30
	Cu	5	25	2	15
	CoFe	5	25	0.4	50
	Cu	5	25	2	15
	Ta	5	30	1	30
PCFT-S-003	Pt	5	30	1	30
	Cu	5	25	2	15
	CoFe	5	25	0.4	63
	Cu	5	25	2	15
	Ta	5	30	1	30

Name	Material	Pressure (10 <sup>-3</sup> mbar)	Power (W)	Rate (Å/s)	Time (s)
PCFT-S-004	Pt	5	30	1	30
	Cu	5	25	2	15
	CoFe	5	25	0.4	83
	Cu	5	25	2	15
	Ta	5	30	1	30
PCFT-S-005	Pt	5	30	1	30
	Cu	5	25	2	15
	CoFe	5	25	0.4	250
	Cu	5	25	2	15
	Ta	5	30	1	30
Aloop 001	Ta	5	30	1	30
	Pt	5	30	1	30
	CoFe	5	25	0.4	15
	Al	5	30	0.8	25
PCFT-S Pumping Sink	Pt	5	30	1	100
	Cu	5	25	2	15
	CoFe	5	25	0.4	125
	Cu	5	25	2	15
	Ta	5	30	1	100
PCFT-S Pumping Mirror	Pt	5	30	1	15
	Cu	5	25	2	15
	CoFe	5	25	0.4	125
	Cu	5	25	2	15
	Ta	5	30	1.1	25
TCuCFCuP-001	Ta	5	30	1.07	28
	Cu	5	25	2.01	15
	CoFe	5	25	0.42	119
	Cu	5	25	2.01	15
	Pt	5	30	1.03	29
TCuCFCuP-002	Ta	5	30	1.07	28
	Cu	5	25	2.01	15
	CoFe	5	25	0.42	119
	Cu	5	25	2.01	15
	Pt	5	30	1.03	29
TCuCFP	Ta	5	30	1.06	29
	Cu	5	25	2.01	15
	CoFe	5	25	0.42	119
	Pt	5	30	1.03	29
TCuCFT	Ta	5	30	1.06	29
	Cu	5	25	2.01	15
	CoFe	5	25	0.42	119
	Ta	5	30	1.06	29

Name	Material	Pressure (10 <sup>-3</sup> mbar)	Power (W)	Rate (Å/s)	Time (s)
Schoen-oR- slow	Ta	5	30	1.07	28
	Cu	5	30	1.71	18
	CoFe	5	25	0.44	114
	Cu	5	30	1.71	18
	Ta	5	30	1.07	28
Schoen-oR-001	Ta	5	30	2.09	15
	Cu	5	30	1.71	18
	CoFe	5	25	2.28	44
	Cu	5	30	1.71	18
	Ta	5	30	2.09	15
Schoen-oR-002	Ta	5	30	2.09	15
	Cu	5	30	1.71	18
	CoFe	5	25	2.28	22
	Cu	5	30	1.71	18
	Ta	5	30	2.09	15
Schoen-oR-003	Ta	5	30	2.09	15
	Cu	5	30	1.71	18
	CoFe	5	25	2.28	15
	Cu	5	30	1.71	18
	Ta	5	30	2.09	15
Schoen-oR-004	Ta	5	30	2.09	15
	Cu	5	30	1.71	18
	CoFe	5	25	2.28	11
	Cu	5	30	1.71	18
	Ta	5	30	2.09	15
Schoen-oR-005	Ta	5	30	2.09	15
	Cu	5	30	1.71	18
	CoFe	5	25	2.28	9
	Cu	5	30	1.71	18
	Ta	5	30	2.09	15
Terminal 001	Ta	5	30	2.09	15
	Al	5	50	1.3	23
	CoFe	5	25	2.28	22
	Al	5	50	1.3	23
	Ta	5	30	2.09	15
Terminal 002	Ta	5	30	2.09	15
	Al	5	50	1.3	23
	CoFe	5	25	2.28	44
	Al	5	50	1.3	23
	Ta	5	30	2.09	15

Name	Material	Pressure (10 <sup>-3</sup> mbar)	Power (W)	Rate (Å/s)	Time (s)
Terminal 003	Ta	5	30	2.09	15
	Al	5	50	1.3	23
	CoFe	5	25	2.28	15
	Al	5	50	1.3	23
	Ta	5	30	2.09	15
Terminal 003 30W	Ta	5	30	2.09	15
	Al	5	50	1.3	23
	CoFe	5	25	2.28	11
	Al	5	50	1.3	23
	Ta	5	30	2.09	15
Terminal 004	Ta	5	30	2.09	15
	Al	5	50	1.3	23
	CoFe	5	25	2.28	9
	Al	5	50	1.3	23
	Ta	5	30	2.09	15
Terminal 005	Ta	5	30	2.09	15
	Al	5	50	1.3	23
	CoFe	5	25	2.28	15
	Al	5	50	1.3	23
	Ta	5	30	2.09	15
inception copy	Ta	5	30	2.09	15
	Al	5	50	1.3	23
	CoFe	5	25	2.28	44
	Al	5	50	1.3	23
	Ta	5	30	2.09	15

**Table A.2:** Deposition parameters for structured samples. The process pressure was  $5 \times 10^{-3}$  mbar for all samples, except for "SSO12-27" ( $6 \times 10^{-3}$  mbar). All depositions were performed at room temperature.

Name	Date	Material	Power (W)	Rate (A/s)	Time (s)
SSO12-01	19.10.17	Pt	30	1	30
		CoFe	30	0.89	22
		Ta	30	1	30
SSO12-02	19.10.17	Pt	30	1	30
		CoFe	30	0.89	22
		Ta	30	1	30
SSO12-03	26.10.17	Pt	30	1	30
		CoFe	30	0.89	125
		Ta	30	1	30
SSO12-13	3.11.17	Pt	30	1	30
		CoFe	25	0.4	125
		Ta	30	1	30
SSO12-14	3.11.17	Pt	30	1	30
		CoFe	25	0.4	125
		Pt	30	1	30
SSO12-15	3.11.17	Pt	30	1	30
		CoFe	25	0.4	125
		Pt	30	1	30
SSO12-16	16.11.17	Al	30	1	30
		CoFe	25	0.4	125
		Pt	30	1	30
SSO12-17	16.11.17	Pt	30	1	30
		CoFe	25	0.4	125
		Pt	30	1	30
SSO12-08	16.11.17	Pt	30	1	30
		CoFe	25	0.4	125
		Pt	30	1	30
SSO12-25	1.12.17	Pt	30	1	100
	4.12.17	Pt	30	1	30
		CoFe	25	0.4	125
		Ta	30	1	30
SSO12-26	1.12.17	Pt	30	1	100
	4.12.17	Pt	30	1	30
		CoFe	25	0.4	125
		Ta	30	1	30
SSO12-27	1.12.17	Pt	30	1	100
	4.12.17	Pt	30	1	30
		CoFe	25	0.4	50
		Ta	30	1	30

Name	Date	Material	Power (W)	Rate (Å/s)	Time (s)
Marker-D 3	12.12.17	Pt	30	1	30
		CoFe	25	0.4	20
		Ta	30	1	30
Marker-D 4	14.12.17	Pt	30	1	30
	18.12.17	Ta	30	1	30
		Cu	25	2	15
		CoFe	25	0.4	125
		Cu	25	2	15
		Ta	30	1	30
Marker-D 5	14.12.17	Pt	30	1	30
	18.12.17	Ta	30	1	30
		Cu	25	2	15
		CoFe	25	0.4	125
		Cu	25	2	15
		Ta	30	1	30
Marker-D 6	14.12.17	Pt	30	1	30
	18.12.17	Ta	30	1	30
		Pt	30	1	30
		CoFe	25	0.4	15
		Al	30	0.8	25
Marker-D 10	19.12.17	Pt	30	1	100
	21.12.17	Pt	30	1	30
		Cu	25	2	15
		CoFe	25	0.4	125
		Cu	25	2	15
		Ta	30	1	30
		Al	30	0.8	625
Marker-D 11	19.12.17	Pt	30	1	100
	16.1.18	Pt	30	1	25
		Cu	25	2	15
		CoFe	25	0.4	125
		Cu	25	2	15
		Ta	30	1	25
		Al	30	0.8	625
Marker-D 12	19.12.17	Pt	30	1	100
	2.2.18	Pt	30	1.02	29
		Cu	25	2.02	15
		CoFe	25	0.42	238
		Cu	25	2.02	15
		Ta	30	1.06	29
		Al	30	2.7	170
9.2.18	Al	30	2.7	170	

Name	Date	Material	Power (W)	Rate (Å/s)	Time (s)
SSO12-31	10.1.18	Pt	30	1	100
SSO12-32	10.1.18	Pt	30	1	100
SSO12-33	10.1.18	Pt	30	1	100
SSO12-34	18.1.18	Pt	30	1	100
SSO12-35	18.1.18	Pt	30	1	100
SSO12-36	18.1.18	Pt	30	1	100
Hallbar Alti 02	30.1.18	Pt	30	1.05	29
		CoFe	25	0.43	14
		Ta	30	1.06	14
Hallbar Alti 03	30.1.18	Ta	30	1.07	28
		Pt	30	1.03	29
		CoFe	25	0.42	14
		Al	30	0.74	14
inception 1	2.2.18	Pt	30	1	100
	14.2.18	Pt	30	2.45	13
		CoFe	25	2.28	13
		Ta	30	2.09	15
	14.2.18	Al	30	0.8	625
inception 2	2.2.18	Pt	30	1	100
	28.2.18	Ta	30	2.09	15
		Al	50	1.3	23
		CoFe	25	2.28	44
		Al	50	1.3	23
		Ta	30	2.09	15
	1.3.18	Al	50	1.3	390
inception 3	2.2.18	Pt	30	1	100
Bones Fine 01	6.2.18	Pt	30	1	100
Bones Fine 01	7.2.18	Pt	30	1	100
Bones Fine 03	7.2.18	Pt	30	1	100



# Appendix B

## Magnetic Properties for Blanket Films

The following table lists the obtained results from XRD and FMR measurements for the blanket film samples. Table B.1 contains the in plane data, whereas table B.2 contains the out of plane data.

**Table B.1:** In plane FMR results. Empty entries imply that no FMR signal was found.

Name	FM thickness (nm)	g-factor	$\mu_0 M_{\text{eff}}$ (T)	$\alpha_G$ ( $1 \times 10^{-3}$ )	$\mu_0 \Delta H$ (mT)
1	13.4	2.01923	2.458	2.88	42.6
7	8.9	2.14576	2.057	13.32	13.9
Goldfinger	5	2.10734	2.057	12.15	5.1
MI 6	1.7	-	-	-	-
PCT 270717	1.4	-	-	-	-
PCT 280717	2	-	-	-	-
PCT 310717	1.1	-	-	-	-
MCFT cold	18.3	2.06624	2.406	4.57	18.1
MCFT hot	17.2	2.07744	2.2	-	-
CoFe-Al	4.4	2.13419	2.17	13.97	14.7
SiCoFA 001	8.7	2.18119	2.206	13.4	9.3
SiCoFA 002	6	2.15025	2.237	10.68	10.1
SiCoFA 003	4.3	2.15837	2.07	14.12	6.4
SiCoFA 004	2.5	2.08739	1.462	6.5	4
SiCoFA 005	6.4	2.17009	2.201	14.62	9.4
SiCoFA 006	4.5	2.1783	2.083	16.64	8.6

Name	FM thickness (nm)	g-factor	$\mu_0 M_{\text{eff}}$ (T)	$\alpha_G$ (1x10-3)	$\mu_0 \Delta H$ (mT)
PCFT 001	3.4	2.11081	1.63091	13	1.4
PCFT 002	3.3	2.11082	1.61465	13.33	3
PCFT 003	2.1	2.11349	1.39914	14.49	5
PCFT 004	2.9	2.11586	1.20475	17.84	7.3
PCFT 005	1.6	-	-	-	-
PCFT 006	2.2	2.12821	1.35194	22.22	6.2
PCFT 007	1.9	2.11414	1.46525	19.98	6.7
PCFT 008	3.3	2.10144	1.76349	14.35	1.1
PCFT 009	5.5	2.10211	1.94464	9.81	0.4
PCFT 010	5.8	2.09806	1.98673	9.89	0.7
PCFT 011	5	2.10255	1.80736	10.63	0.3
PCFT 012	2.8	2.10065	1.63576	13.52	2.2
PCFT 013	1.4	2.11455	1.31542	20.98	5.2
PCFT 014	5.2	2.14804	1.91954	21.45	22.1
PCFT 015	2.5	2.12599	1.5699	15.79	18.4
PCFT 016	2.4	2.13868	0.83999	25.51	28.8
PCFT 017	1.9	2.10225	1.54796	21.25	5.1
PCFT 018	2	2.10156	1.67721	16.97	3.1
PCFT 019	3.4	2.09644	1.7175	18.92	2.2
PCFT 020	3.6	2.10305	1.80506	12.57	1.6
PCFT 021	8.3	2.09915	2.04189	8.78	0.5
PCFT 022	5	2.10189	1.79445	15.64	1.4
PCFT 023	5*	-	-	-	-
PCFT 024	4.3	2.105	1.32468	-	-
PCFT 025	5*	2.09179	1.84552	9	0.8
PCFT 026	4.8	2.08119	1.34774	-	-
PCFT 027	5.2	2.27781	1.65891	32.17	6.2

Name	FM thickness (nm)	g-factor	$\mu_0 M_{\text{eff}}$ (T)	$\alpha_G$ (1x10-3)	$\mu_0 \Delta H$ (mT)
Schoen 001	10*	2.07787	1.979	7	3.6
Schoen 002	5*	2.09107	1.71199	5.92	4.6
Schoen 003	3*	2.08902	1.39444	6.91	2.9
Schoen 004	9	2.08496	2.05596	4.45	0.8
Schoen 005	4.8	2.08643	1.90404	5.56	0.3
Schoen 006	2.8	2.09561	1.72417	7.85	1.9
Schoen 007	2.3	2.08956	1.47899	9.66	1.7
Schoen 008	1.6	2.09604	1.35403	10.95	7.9

\* indicates that for the respective sample no, or no reliable XRD results is present. The thickness is estimated from the deposition rate obtained from the QC. Orange values for Gilbert-alpha and inhomogeneous field allude to no simple linear behavior. A linear function could only be fitted to a part of the measured frequency range.

**Table B.2:** Out of plane FMR results. Empty entries imply that no FMR signal was found or fitting failed due to interleaved resonance peaks.

Name	FM thickness (nm)	g-factor	$\mu_0 M_{\text{eff}}$ (T)	$\alpha_G$ (1x10-3)	$\mu_0 \Delta H$ (mT)
Schoen 005	4.8	2.06089	1.9182	1.16	5.6
Schoen 006	2.8	2.05565	1.75851	35.6	2.9
Schoen 007	2.3	2.04713	1.50283	4.63	7.4
Schoen 008	1.6	2.04433	1.39289	5.41	9.2
PCFT-S 001	5.3	1.97019	1.9674	3.48	1.1
PCFT-S 002	1.8	2.03512	1.58134	6.99	3.6
PCFT-S 003	2.5	2.05602	1.73931	6.42	1.1
PCFT-S 004	3.5	2.05147	1.87755	5.3	0.6
PCFT-S 005	9	2.02762	2.11152	2.79	0.9
PCFT-S Pump Sink	5*	2.09374	1.9328	6.4	0.8
PCFT-S Pump Mirror	5*	2.09317	1.99548	5.17	0.7
Aloop 001	0.6*	-	-	-	-

Name	FM thickness (nm)	g-factor	$\mu_0 M_{\text{eff}}$ (T)	$\alpha_G$ (1x10-3)	$\mu_0 \Delta H$ (mT)
TCuCFCuP 001	4.1	2.03043	1.8065	3.46	2.5
TCuCFCuP 002	4	1.96617	1.75393	3.15	3.9
TCuCFP	4.7	1.94037	1.78982	7.21	2.7
TCuCFT	5	2.00183	1.78344	4.22	1.3
Schoen-oR-slow	4.2	1.98023	1.9274	2.44	1.4
Schoen-oR 001	8.5	1.98498	2.09839	2.7	0.7
Schoen-oR 002	4.2	2.07153	1.87827	2.42	2.9
Schoen-oR 003	3.6	2.05659	1.69518	2.83	6.7
Schoen-oR 004	2.4	2.06795	1.54544	4.96	6.2
Schoen-oR 005	2.2	2.06029	1.37777	5.5	13.2
Terminal 001	4.63	2.05235	1.81706	1.93	2.9
Terminal 002	9.27	2.01402	2.07474	2.77	2.5
Terminal 003	2.82	2.03757	1.58736	-	-
Terminal 003-30W	3.14	2.05591	1.72968	2.52	2.9
Terminal 004	2.35	2.04815	1.27028	3.56	4.8
Terminal 005	1.60	2.02808	1.07652	5.73	8.1

\* indicates that for the respective sample no, or no reliable XRD results is present. The thickness is estimated from the deposition rate obtained from the QC.

Orange values for Gilbert-alpha and inhomogeneous field allude to no simple linear behavior. A linear function could only be fitted to a part of the measured frequency range.

## Appendix C

# Frequently Encountered Issues with the PicoMaster 200

### C.1 Focus Capture

The PicoMaster 200 is a very sensitive writing unit which made it necessary to develop a proper spin coating process. Focus errors frequently appeared as it requires a very homogeneous dispersion of resist. Reflections of a red laser are measured resulting in a so called "focus sum" voltage. The acceptable range lies between -1 V and -10 V. In case of exceeding the limit on either the low or the high margin a focus error will be returned. A smooth thickness distribution leads to a steady focus sum. Analogously, a rough surface causes high variations in the reference voltage. The red laser power (RLP) has to be adjusted for each sample in order to obtain a focus sum level where the acceptable range is met over the whole writing area. The success of this adjustment turned out to depend strongly on the spin coating. It was found that fast coating, i. e., a maximum time between pouring resist on the substrate and starting the spinning of 2 s is crucial for a successful fabrication. A common issue is the abort of the writing process right at the start of the procedure. At the beginning of a project the module tries to find the focus. The starting position herefore is not the top left point of the writing area but a bit to the top (scan axis). The laser needs some space for acceleration depending on the writing speed. For 50 mm/s the starting point is 0.5 mm before the actual writing start in scan axis. The step axis is unaffected. As this point is usually nearer to the edge of the substrate, it often occurs that the focus sum returns higher values than for the center of the substrate. Even though the upper focus sum limit is -10 V the module cannot catch values higher than -8 V due to an overshoot exceeding the limit. When the focus was found before, a sum voltage between -8 V and -10 V is of no problem. It often occurred that in the center of the substrate the sum voltage was near the lower limit of -1 V making it necessary to increase the RLP. At the same time this adjustment led to values higher than -8 V at the edge of the sample impeding the first catch of the focus. It was found that by changing the RLP, the focus sum only changes slowly. It is thus possible to implement the desired RLP in the setup settings and then check the focus on the substrate manually. By reducing the RLP by a factor of two the focus sum drops. When its saturation value is met it is possible to then start the process. As the PicoMaster 200 then tries to catch the focus at the starting position with the higher implemented RLP the focus sum still needs to ramp up. The resulting

overshoot does not exceed the intrinsic limit and a stable focus sum is found, necessary for the project to start.

For the first spin coating tests  $10 \times 6 \text{ mm}^2$  substrates were used. This testing series foundered due to too small writing fields. The writable area did not even reach  $4 \times 2.5 \text{ mm}^2$  as resist distribution at the borders becomes irregular causing focus errors on both limits during exposure. Later on  $12 \times 12 \text{ mm}^2$  substrate were used and the spin coating process was optimized for this larger sizes. A sample list of the  $12 \times 12 \text{ mm}^2$  substrates is presented in appendix C. Even though  $10 \times 6 \text{ mm}^2$  seem to be hopeless it has to be mentioned that the optimized process has not been tested on them.

## C.2 Module Collision and Misalignment

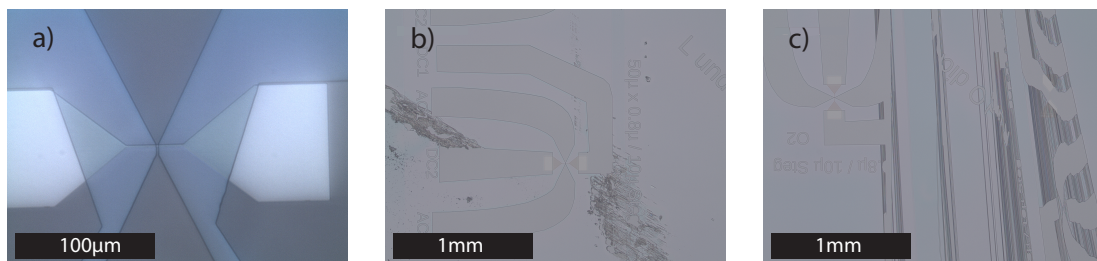


**Figure C.1:** Micrographs showing issues regarding the photolithography. a) The Alignment failed as a centered crossing of the two small strips was planned. b) The structure was written successfully but the writing module crashed into the substrate leaving scratches in the resist. c) The first part of the structure was written but then focus errors appeared. At its occurrence the laser writes an entire line. Apparently the module crashed the sample leading to a position and orientation change. This can be seen due to the tilt of the lines.

Figure C.1 depicts some frequently appearing errors. In C.1 a) the alignment failed. A centered crossing of a  $\text{Co}_{25}\text{Fe}_{75}$  strip and an aluminum antenna was planned. The photo shows that the ferromagnetic strip crosses the contact pad instead of the antenna. For sample fabrication and alignment a marker step was performed before. The empty sample was coated and markers on the top left and bottom right corner of the substrate were written and deposited. The markers defined a writable area of  $8 \times 8 \text{ mm}^2$  on the  $12 \times 12 \text{ mm}^2$  substrate. These markers were then used for the subsequent deposition steps to reference a coordinate system. This method should intrinsically remove all kinds of alignment errors within the following lithographical steps with respect to each other. Apparently this was not the case for the present sample and its reason is as follows.

The PicoMaster 200 uses a camera installed with the writing module at a fixed offset from the writing laser. When declaring the positions of the substrate using the camera the software can then calculate the positions for the laser to write. When a focus error appears and a substrate thickness is implemented the machine virtually has a safety capture function to avoid crashing the writing head into the sample. Unfortunately, this safety feature does rarely work making it possible to crash. The lowest point of the head is not the laser lens but another part on the module a bit to the left of the laser. The left scratches

of the crash can be seen in Fig. C.1 b). As the picture shows, the structure was written without problems even though we see the marks on both sides, left and right. Picture C.1 c) shows the very same sample but the frame is a bit more to the right. The laser writes from left to right and it is clearly visible at what point errors started to occur. This is the actual laser position when the module crashed into to the sample, but as the lowest part of the module seems to be to the left, scratches on the samples are to the left at a position it already wrote (see C.1 b)). By collision the sample's position and tilt is changed. The machine then loses focus as it suspects the sample where it now is not. When a focus error appears it draws an entire line from top to bottom which can be seen in Fig. C.1 c). When the rotation of the sample is changed also the lines are tilted as the axes became mismatched. If this were the only problem one could then clean and coat the sample again and retry the procedure. But the collision also changes the offset of the camera to the laser by several microns making it a complicated task to rearrange the alignment. The offset can be changed in the software but to find out its real offset is a time-consuming procedure. Regarding that the offset change occurs every once in a while it is easier to manipulate the fine tuning of the marker. For this, one has to look for the encountered offset and quantify it roughly in x and y direction. If the newly written structure is, e. g., too far to the bottom left one has to subtract the determined x-offset in the Fiducial settings from the current step axis value and add the y-offset to the scan axis. Hence, positive step axis values shift the writing field to the left and positive scan axis values shift the writing area to the top. When no collisions appear, or better, the collision issue is solved, the first marker step should foil all offset errors as it creates its own reference system. At that point, no changes have to be undertaken.



## Appendix D

### Laserlithography - Optimization Parameters

The recipe described in chapter 2 was found by testing different cleansing, amount of resist poured onto the substrate, spinning parameters and exposure dose. In the following a sample table containing the different parameters is presented. As the "dirtiest" cleansing (3 min in ultra-sound bath with highest power in acetone and afterwards the same step with isopropanol) was found to be sufficient these parameters will not be presented. First samples were cleansed by 5 min in hot acetone (70° C) and 3 min in ultra-sound with highest power. This step was performed twice and afterwards repeated with isopropanol. As the baking step was always the same (70s at 110° C) it also will not be displayed in the table. Some samples were exposed more than once, e. g., because of dose tests or multistep fabrication. The first testing series with the 10 × 6 mm<sup>2</sup> will also not be shown as photolithography failed for almost all substrates with this size. Different spinning velocities were tested and also the pre-spinning was omitted for the small samples. As one can extract from the tables, the first samples showed a higher accumulation of focus errors even though the quantified parameters were not changed significantly. As mentioned before, the time the resist is exposed to air until it got spinned is crucial. With time the execution became faster by confidence gain and hence, the number of focus error decreased. To enable faster performance the volume measure was changed from drops to µl. Towards the end of the sample list one sees that focus error again tend to appear more frequently. We assume that this is because of aging of the resist as too much solvent evaporated from the resist bottle. Presumably, decanting the resist is necessary for further usage. In the following, table D.1 presents the spin coating parameters and table D.2 lists the exposure parameters. The samples SSO12-16 - SSO12-36 were coated by the student assistant Christoph Scheuer.

**Table D.1:** Spin Coating parameters and the returned focus errors from the writing unit. Acceleration times for the prespinning were chosen to be the fastest possible, i. e., 200 ms for 500 rpm and 600 ms for 5000 rpm.

Name	Coating Date	Pre-spinning (rpm)	Spinning (rpm)	Volume	Error Count
SSO12-01	17.10.17	500 (5sec)	5000	6 drops	0
SSO12-02	17.10.17	500 (5sec)	5000	6 drops	$>10^2$
SSO12-03	17.10.17	500 (5sec)	5000	6 drops	0
SSO12-04	20.10.17	500 (5sec)	5000	6 drops	0
SSO12-05	20.10.17	500 (5sec)	5000	6 drops	0
SSO12-06	20.10.17	500 (5sec)	5000	6 drops	1
SSO12-07	20.10.17	500 (5sec)	5000	6 drops	23
SSO12-08	20.10.17	500 (5sec)	5000	6 drops	0
SSO12-09	20.10.17	500 (5sec)	5000	6 drops	$>10^3$
SSO12-10	25.10.17	500 (5sec)	5000	6 drops	$>10^2$
SSO12-12	25.10.17	500 (5sec)	5000	6 drops	0
SSO12-13	27.10.17	500 (5sec)	5000	6 drops	2
SSO12-14	27.10.17	500 (5sec)	5000	6 drops	5
SSO12-15	27.10.17	500 (5sec)	5000	6 drops	0
SSO12-16	6.11.17	500 (5sec)	5000	6 drops	1
SSO12-17	6.11.17	500 (5sec)	5000	6 drops	$>10^2$
SSO12-18	6.11.17	500 (5sec)	5000	6 drops	0
SSO12-19	27.11.17	500 (5sec)	5000	6 drops	$>10^2$
SSO12-20	27.11.17	500 (5sec)	5000	6 drops	0
SSO12-21	27.11.07	500 (5sec)	5000	6 drops	0
SSO12-22	6.12.17	500 (5sec)	5000	6 drops	$>10^2$
SSO12-23	6.12.17	500 (5sec)	5000	6 drops	$>10^2$
SSO12-24	6.12.17	500 (5sec)	5000	6 drops	5
SSO12-25	30.11.17	500 (5sec)	5000	6 drops	0
	01.12.17	500 (5sec)	5000	6 drops	0
	05.12.17	500 (5sec)	5000	6 drops	0
SSO12-26	30.11.27	500 (5sec)	5000	6 drops	0
	01.12.17	500 (5sec)	5000	6 drops	0
SSO12-27	30.11.27	500 (5sec)	5000	6 drops	0
	01.12.17	500 (5sec)	5000	6 drops	0

Name	Coating Date	Pre-spinning (rpm)	Spinning (rpm)	Volume	Error Count
SSO12-28	11.12.17	500 (5sec)	5000	6 drops	0
SSO12-29	11.12.17	500 (5sec)	5000	6 drops	0
SSO12-30	11.12.17	500 (5sec)	5000	6 drops	0
SSO12-31	18.12.17	500 (5sec)	5000	120 $\mu$ l	0
SSO12-32	18.12.17	500 (5sec)	5000	120 $\mu$ l	0
SSO12-33	18.12.17	500 (5sec)	5000	120 $\mu$ l	0
SSO12-34	8.1.18	500 (3sec)	5000	120 $\mu$ l	0
SSO12-35	8.1.18	500 (3sec)	5000	120 $\mu$ l	59
SSO12-36	8.1.18	500 (3sec)	5000	120 $\mu$ l	2
Marker-D-01	05.12.17	500 (5sec)	5000	6 drops	0
	05.12.17	500 (5sec)	5000	6 dops	0
Marker-D-02	05.12.17	500 (5sec)	5000	6 drops	0
	05.12.17	500 (5sec)	5000	6 drops	0
Marker-D-03	05.12.17	500 (5sec)	5000	6 drops	0
	05.12.17	500 (5sec)	5000	6 drops	0
Marker-D-04	14.12.17	500 (5sec)	5000	6 dops	0
	14.12.17	500 (5sec)	5000	110 $\mu$ l	0
Marker-D-05	14.12.17	500 (5sec)	5000	120 $\mu$ l	0
	14.12.17	500 (5sec)	5000	110 $\mu$ l	45
Marker-D-06	14.12.17	500 (5sec)	5000	110 $\mu$ l	0
	14.12.17	500 (5sec)	5000	110 $\mu$ l	0
Marker-D-07	19.12.17	500 (5sec)	5000	110 $\mu$ l	-
Marker-D-08	19.12.17	500 (5sec)	5000	110 $\mu$ l	-
	19.12.17	500 (3sec)	5000	120 $\mu$ l	0
	19.12.17	500 (3sec)	5000	120 $\mu$ l	-
Marker-D-09	19.12.17	500 (3sec)	5000	110 $\mu$ l	0
	19.12.17	500 (3sec)	5000	120 $\mu$ l	
Marker-D-10	18.12.17	500 (5sec)	5000	110 $\mu$ l	14
	19.12.17	500 (3sec)	5000	120 $\mu$ l	0
	21.12.17	500 (3sec)	5000	120 $\mu$ l	0
Marker-D-11	18.12.17	500 (5sec)	5000	110 $\mu$ l	0
	19.12.17	500 (3sec)	5000	120 $\mu$ l	0
	16.01.18	500 (3sec)	5000	120 $\mu$ l	0

Name	Coating Date	Pre spinning (rpm)	Spinning (rpm)	Volume	Error Count
Marker-D-12	18.12.17	500 (5sec)	5000	110 $\mu$ l	0
	19.12.17	500 (3sec)	5000	120 $\mu$ l	0
	02.02.18	500 (3sec)	5000	120 $\mu$ l	$>10^3$
	05.02.17	500 (3sec)	5000	120 $\mu$ l	0
	05.02.18	500 (3sec)	5000	120 $\mu$ l	0
	06.02.18	500 (3sec)	5000	120 $\mu$ l	0
	07.02.18	500 (3sec)	5000	120 $\mu$ l	0
	08.02.18	500 (3sec)	5000	120 $\mu$ l	0
	09.02.18	500 (3sec)	5000	120 $\mu$ l	0
inception 01	01.02.18	500 (3sec)	5000	120 $\mu$ l	0
	02.02.18	500 (3sec)	5000	120 $\mu$ l	0
	14.02.18	500 (3sec)	5000	120 $\mu$ l	$>10^4$
inception 02	01.02.18	500 (3sec)	5000	120 $\mu$ l	0
	02.02.18	500 (3sec)	5000	120 $\mu$ l	0
	01.03.18	500 (3sec)	5000	120 $\mu$ l	$>10^2$
	01.03.18	500 (3sec)	5000	120 $\mu$ l	$>10^3$
inception 03	01.02.18	500 (3sec)	5000	120 $\mu$ l	0
	02.02.18	500 (3sec)	5000	120 $\mu$ l	-
Hallbars alti 1	22.01.18	500 (3sec)	5000	120 $\mu$ l	$>10^3$
	30.01.18	500 (3sec)	5000	120 $\mu$ l	0
Hallbars alti 2	22.1.18	500 (3sec)	5000	120 $\mu$ l	2
Hallbars alti 3	22.1.18	500 (3sec)	5000	120 $\mu$ l	0
Bones Fine 01	06.02.18	500 (3sec)	5000	120 $\mu$ l	$>10^3$
	06.02.18	500 (3sec)	5000	120 $\mu$ l	0
Bones Fine 02	6.2.18	500 (3sec)	5000	120 $\mu$ l	16
Bones Fine 03	6.2.18	500 (3sec)	5000	120 $\mu$ l	0

**Table D.2:** Exposure parameters for coated samples. The writing speed of 50 mm/s was applied to all samples. The used spot settings are medium resolution and high reduction and a blue laser threshold current of 40 mA was implemented.

Name	Exposure Date	Dose (mJ/cm <sup>2</sup> )	RLP ( $\mu$ W)	Error Count	Development Time (s)
SSO12-01	18.10.17	40	20	0	55
SSO12-02	18.10.17	40	20	$>10^2$	70
SSO12-03	18.10.17	40	25	0	85
SSO12-04	20.10.17	100	25	0	-
SSO12-05	20.10.17	100	30	0	-
SSO12-06	20.10.17	100	30	1	-
SSO12-07	23.10.17	150	30	23	-
	23.10.17	100	30	0	-
	23.10.17	40	30	0	-
SSO12-08	24.10.17	0.1	30	0	-
	24.10.17	0.1	30	0	-
	24.10.17	0.1	30	0	-
	24.10.17	0.1	30	0	-
SSO12-09	24.10.17	0.1	30	$>10^2$	-
	25.10.17	0.1	30	$>10^3$	-
	25.10.17	0.1	30		-
SSO12-10	25.10.17	0.1	30	0	-
	26.10.17	0.1	30	0	-
	26.10.17	0.1	30	$>10^2$	-
	26.10.17	0.1	30	14	-
SSO12-12	27.10.17	0.1	35	0	-
	27.10.17	0.1	35	0	-
	27.10.17	0.1	35	0	-
	27.10.17	0.1	35	0	-
SSO12-13	02.11.17	75	35	0	-
	02.11.17	100	35	0	-
	02.11.17	125	35	1	-
	02.11.17	150	35	1	40
SSO12-14	02.11.17	75	35	1	-
	02.11.17	100	35	1	-
	02.11.17	125	35	3	-
	02.11.17	150	35	0	60
SSO12-15	03.11.17	75	40	0	-
	03.11.17	100	40	0	-
	03.11.17	125	40	0	-
	03.11.17	150	40	0	80

Name	Exposure Date	Dose (mJ/cm <sup>2</sup> )	RLP ( $\mu$ W)	Error Count	Development Time (s)
SSO12-16	08.11.17	100	35	0	-
	08.11.17	120	35	1	-
	08.11.17	140	35	0	-
	08.11.17	160	35	0	45
SSO12-17	08.11.17	100	35	0	-
	08.11.17	120	35	$>10^2$	-
	08.11.17	140	35	0	-
	08.11.17	160	35	0	60
SSO12-18	08.11.17	100	35	0	-
	08.11.17	120	35	0	-
	08.11.17	140	35	0	-
	08.11.17	160	35	0	75
SSO12-19	27.11.17	120	35	$>10^2$	-
SSO12-20	28.11.17	140	35	0	-
	28.11.17	180	35	0	-
	28.11.17	220	35	0	-
	28.11.17	260	35	0	-
SSO12-21	28.11.17	185	40	0	-
SSO12-22	6.12.17	165	32	$>10^2$	60
SSO12-23	11.12.17	165	32	11	-
	11.12.17	170	32	$>10^2$	-
SSO12-24	06.12.17	165	32	0	-
	06.12.17	165	32	5	-
	06.12.17	175	32	0	-
	06.12.17	180	32	0	60
SSO12-25	01.12.17	180	35	0	70
	04.12.17	180	35	0	60
SSO12-26	01.12.17	180	30	0	60
	04.12.17	180	35	0	60
SSO12-27	01.12.17	180	30	0	60
	04.12.17	180	35	0	60
SSO12-28	11.12.17	165	32	0	-
	11.12.17	170	32	0	-
	11.12.17	175	32	0	-
	11.12.17	180	32	0	60
SSO12-29	18.12.17	165	32	0	-
	18.12.17	170	50	0	-
	18.12.17	175	50	0	-
	18.12.17	180	50	0	65

Name	Exposure Date	Dose (mJ/cm <sup>2</sup> )	RLP ( $\mu$ W)	Error Count	Development Time (s)
SSO12-30	19.12.17	195	35	0	-
	19.12.17	190	35	0	-
	19.12.17	185	35	0	-
	19.12.17	180	35	0	60
SSO12-31	20.12.17	195	35	0	-
	20.12.17	190	35	0	-
	20.12.17	185	35	0	-
	20.12.17	180	35	0	65
SSO12-32	08.01.18	195	35	0	-
	08.01.18	190	35	0	-
	08.01.18	185	35	0	-
	08.01.18	180	35	0	60
SSO12-33	08.01.18	195	35	0	-
	08.01.18	190	34	0	-
	08.01.18	185	34	0	-
	08.01.18	180	33	0	55
SSO12-34	10.01.18	195	35	0	-
	10.01.18	190	35	0	-
	10.01.18	185	35	0	-
	10.01.18	180	35	0	55
SSO12-35	10.01.18	195	35	59	-
	10.01.18	190	35	0	-
	10.01.18	185	35	0	-
	15.01.18	180	35	0	60
SSO12-36	15.01.18	195	35	0	-
	15.01.18	190	35	0	-
	15.01.18	185	35	2	-
	15.01.18	180	35	0	65
Marker-D-01	05.12.17	180	35	0	60
	05.12.17	180	30	0	60
Marker-D-02	05.12.17	180	35	0	60
	05.12.17	180	35	0	60
Marker-D-03	05.12.17	180	30	0	60
	12.12.17	180	35	0	60
Marker-D-04	14.12.17	180	35	0	60
	14.12.17	180	30	0	60
Marker-D-05	14.12.17	180	35	0	60
	14.12.17	180	35	45	60

Name	Exposure Date	Dose (mJ/cm <sup>2</sup> )	RLP ( $\mu$ W)	Error Count	Development Time (s)
Marker-D-06	14.12.17	180	35	0	60
	15.12.17	185	35	0	60
Marker-D-08	19.12.17	180	35	0	60
Marker-D-09	19.12.17	180	35	0	60
Marker-D-10	18.12.17	180	50	14	60
	21.12.17	200	35	0	60
	21.12.17	200	35	0	60
Marker-D-11	19.12.17	180	35	0	60
	12.01.18	200	35	0	60
	16.01.18	180	35	0	60
Marker-D-12	19.12.17	180	35	0	60
	01.02.18	180	40	0	60
	02.02.18	180	35	$>10^3$	60
	05.02.18	180	35	0	60
	05.02.18	180	35	0	60
	06.02.18	180	35	0	60
	06.02.18	180	40	0	60
	08.02.18	180	40	0	60
	09.02.18	180	40	0	60
inception 01	01.02.18	180	35	0	60
	13.02.18	175	40	0	60
	14.02.18	175	40	$>10^4$	60
inception 02	01.02.18	180	35	0	60
	28.02.18	175	45	0	60
	01.03.18	175	35	$>10^2$	-
	01.03.18	175	40	$>10^3$	60
inception 03	01.02.18	180	35	0	60
Hallbars alti 1	22.01.18	180	35	$>10^3$	-
	30.01.18	180	34	0	60
Hallbars alti 2	22.01.18	180	36	2	60
Hallbars alti 3	22.01.18	180	38	0	60

---

Name	Exposure Date	Dose (mJ/cm <sup>2</sup> )	RLP ( $\mu$ W)	Error Count	Development Time (s)
Bones	07.02.18	180	38	0	-
Fine 01	07.02.18	175	38	0	-
	07.02.18	170	38	0	-
	07.02.18	185	38	0	60
Bones	06.02.18	180	37	1	-
Fine 02	06.02.18	175	35	15	-
	06.02.18	170	37	0	-
	06.02.18	185	36	0	55
Bones	07.02.18	180	38	0	-
Fine 03	07.02.18	175	38	0	-
	07.02.18	170	38	0	-
	07.02.18	185	38	0	50

---



# Bibliography

- [1] J. Bardeen and W. Brattain, “The Transistor, A Semiconductor Triode”, Proc. IEEE **86**, 29 (1998).
- [2] G. E. Moore, “Cramming more components onto integrated circuits”, IEEE Solid-State Circuits Soc. Newsl. **11**, 33 (2006).
- [3] F. Ulaby, “The Legacy of Moore ’ s Law”, **94**, 1251 (2006).
- [4] M. N. Baibich, J. M. Broto, A. Fert, F. N. Van Dau, F. Petroff, P. Etienne, G. Creuzet, A. Friederich, and J. Chazelas, “Giant Magnetoresistance of (001)Fe/(001)Cr Magnetic Superlattices”, Phys. Rev. Lett. **61**, 2472 (1988).
- [5] G. Binasch, P. Grünberg, F. Saurenbach, and W. Zinn, “Enhanced magnetoresistance in layered magnetic structures with antiferromagnetic interlayer exchange”, Phys. Rev. B **39**, 4828 (1989).
- [6] Guenole Jan, L. Thomas, Son Le, Yuan-Jen Lee, Huanlong Liu, Jian Zhu, J. Iwata-Harms, S. Patel, Ru-Ying Tong, S. Serrano-Guisan, Dongna Shen, Renren He, Jesmin Haq, Jeffrey Teng, Vinh Lam, R. Annapragada, Yu-Jen Wang, Tom Zhong, T. Torng, and Po-Kang Wang, “Achieving Sub-ns switching of STT-MRAM for future embedded LLC applications through improvement of nucleation and propagation switching mechanisms”, in 2016 IEEE Symp. VLSI Technol. (June 2016), pp. 1–2.
- [7] V. Demidov, S. Urazhdin, G. de Loubens, O. Klein, V. Cros, A. Anane, and S. Demokritov, “Magnetization oscillations and waves driven by pure spin currents”, Phys. Rep. **673**, 1 (2017).
- [8] M. A. W. Schoen, D. Thonig, M. L. Schneider, T. J. Silva, H. T. Nembach, O. Eriksson, O. Karis, and J. M. Shaw, “Ultra-low magnetic damping of a metallic ferromagnet”, Nat. Phys. **12**, 839 (2016).
- [9] V. E. Demidov, S. Urazhdin, H. Ulrichs, V. Tiberkevich, A. Slavin, D. Baither, G. Schmitz, and S. O. Demokritov, “Magnetic nano-oscillator driven by pure spin current”, Nat. Mater. **11**, 1028 (2012).
- [10] Z. Wang, Y. Sun, M. Wu, V. Tiberkevich, and A. Slavin, “Control of Spin Waves in a Thin Film Ferromagnetic Insulator through Interfacial Spin Scattering”, Phys. Rev. Lett. **107**, 146602 (2011).
- [11] S. Mankovsky, D. Ködderitzsch, G. Woltersdorf, and H. Ebert, “First-principles calculation of the Gilbert damping parameter via the linear response formalism with application to magnetic transition metals and alloys”, Phys. Rev. B **87**, 014430 (2013).

- [12] H. Ebert, S. Mankovsky, D. Ködderitzsch, and P. J. Kelly, “Ab Initio Calculation of the Gilbert Damping Parameter via the Linear Response Formalism”, *Phys. Rev. Lett.* **107**, 066603 (2011).
- [13] V. Kamberský, “Spin-orbital Gilbert damping in common magnetic metals”, *Phys. Rev. B* **76**, 134416 (2007).
- [14] A. Brataas, Y. Tserkovnyak, and G. E. W. Bauer, “Scattering Theory of Gilbert Damping”, *Phys. Rev. Lett.* **101**, 037207 (2008).
- [15] M. Fähnle and D. Steiauf, “Breathing Fermi surface model for noncollinear magnetization: A generalization of the Gilbert equation”, *Phys. Rev. B* **73**, 184427 (2006).
- [16] A. A. Starikov, P. J. Kelly, A. Brataas, Y. Tserkovnyak, and G. E. W. Bauer, “Unified First-Principles Study of Gilbert Damping, Spin-Flip Diffusion, and Resistivity in Transition Metal Alloys”, *Phys. Rev. Lett.* **105**, 236601 (2010).
- [17] I. Turek, J. Kudrnovský, and V. Drchal, “Nonlocal torque operators in ab initio theory of the Gilbert damping in random ferromagnetic alloys”, *Phys. Rev. B* **92**, 214407 (2015).
- [18] G. Betz and W. Husinsky, “Modelling of cluster emission from metal surfaces under ion impact.”, *Philos. Trans. A. Math. Phys. Eng. Sci.* **362**, 177 (2004).
- [19] Y. Yamamura and H. Tawara, “Energy Dependence of Ion-Induced Sputtering Yields From Monatomic Solids At Normal Incidence”, *At. Data Nucl. Data Tables* **62**, 149 (1996).
- [20] A. Anders, “Tutorial: Reactive high power impulse magnetron sputtering (R-HiPIMS)”, *J. Appl. Phys.* **121**, 171101 (2017).
- [21] M. W. Thompson, “II. The energy spectrum of ejected atoms during the high energy sputtering of gold”, *Philos. Mag.* **18**, 377 (1968).
- [22] Y. Kudriavtsev, A. Villegas, A. Godines, and R. Asomoza, “Calculation of the surface binding energy for ion sputtered particles”, *Appl. Surf. Sci.* **239**, 273 (2005).
- [23] V. Holy, J. Kubena, I. Ohlidal, K. Lischka, and W. Plotz, “X-ray reflection from rough layered systems”, *Phys. Rev. B* **47**, 15896 (1993).
- [24] L. G. Parratt, “Surface Studies of Solids by Total Reflection of X-Rays”, *Phys. Rev.* **95**, 359 (1954).
- [25] Y. H. Phang, D. E. Savage, R. Kariotis, and M. G. Lagally, “X-ray diffraction measurement of partially correlated interfacial roughness in multilayers”, *J. Appl. Phys.* **74**, 3181 (1993).
- [26] Y. Yoneda, “Anomalous Surface Reflection of X Rays”, *Phys. Rev.* **131**, 2010 (1963).
- [27] R. L. Headrick, J. Baribeau, and Y. E. Strausser, “Anisotropic roughness in Ge/Si superlattices”, *Appl. Phys. Lett.* **66**, 96 (1995).
- [28] S. K. Sinha, E. B. Sirota, S. Garoff, and H. B. Stanley, “X-ray and neutron scattering from rough surfaces”, *Phys. Rev. B* **38**, 2297 (1988).

- [29] R. G. Newton, *Scattering Theory of Waves and Particles*, 2nd ed. (Springer Berlin Heidelberg, Berlin, Heidelberg, 1982), p. 745.
- [30] V. Granville, M. Krivanek, and J.-P. Rassin, “Simulated annealing: a proof of convergence”, *IEEE Trans. Pattern Anal. Mach. Intell.* **16**, 652 (1994).
- [31] H.-G. Rhee, “Direct Laser Lithography and Its Applications”, in *Lithography*, edited by K. Pesek (InTech, Feb. 2010), pp. 1–16.
- [32] M. C. Wu, A. Aziz, J. D. S. Witt, M. C. Hickey, M. Ali, C. H. Marrows, B. J. Hickey, and M. G. Blamire, “Structural and functional analysis of nanopillar spin electronic devices fabricated by 3D focused ion beam lithography”, *Nanotechnology* **19**, 485305 (2008).
- [33] P. P. Freitas, F. A. Cardoso, V. C. Martins, S. A. M. Martins, J. Loureiro, J. Amaral, R. C. Chaves, S. Cardoso, L. P. Fonseca, A. M. Sebastião, M. Pannetier-Lecoer, and C. Fermon, “Spintronic platforms for biomedical applications”, *Lab Chip* **12**, 546 (2012).
- [34] K. Inomata, N. Ikeda, N. Tezuka, R. Goto, S. Sugimoto, M. Wojcik, and E. Jedryka, “Highly spin-polarized materials and devices for spintronics”, *Sci. Technol. Adv. Mater.* **9**, 014101 (2008).
- [35] D. Bisero, P. Cremon, M. Madami, M. Sepioni, S. Tacchi, G. Gubbiotti, G. Carlotti, A. O. Adeyeye, N. Singh, and S. Goolaup, “Effect of dipolar interaction on the magnetization state of chains of rectangular particles located either head-to-tail or side-by-side”, *J. Nanoparticle Res.* **13**, 5691 (2011).
- [36] S. Ikeda, J. Hayakawa, Y. M. Lee, F. Matsukura, Y. Ohno, T. Hanyu, and H. Ohno, “Magnetic Tunnel Junctions for Spintronic Memories and Beyond”, *IEEE Trans. Electron Devices* **54**, 991 (2007).
- [37] S. Terry, J. Jerman, and J. Angell, “A gas chromatographic air analyzer fabricated on a silicon wafer”, *IEEE Trans. Electron Devices* **26**, 1880 (1979).
- [38] E. F. Nuwaysir, W. Huang, T. J. Albert, J. Singh, K. Nuwaysir, A. Pitas, T. Richmond, T. Gorski, J. P. Berg, J. Ballin, M. McCormick, J. Norton, T. Pollock, T. Sumwalt, L. Butcher, D. Porter, M. Molla, C. Hall, F. Blattner, M. R. Sussman, R. L. Wallace, F. Cerrina, and R. D. Green, “Gene expression analysis using oligonucleotide arrays produced by maskless photolithography.”, *Genome Res.* **12**, 1749 (2002).
- [39] S. M. Dirk, S. W. Howell, S. Zmuda, K. Childs, M. Blain, R. J. Simonson, and D. R. Wheeler, “Novel one-dimensional nanogap created with standard optical lithography and evaporation procedures”, *Nanotechnology* **16**, 1983 (2005).
- [40] T. Inokuchi, T. Marukame, T. Tanamoto, H. Sugiyama, M. Ishikawa, and Y. Saito, “Reconfigurable characteristics of spintronics-based MOSFETs for nonvolatile integrated circuits”, in 2010 Symp. VLSI Technol. (June 2010), pp. 119–120.
- [41] MicroChemicals, *Baking Steps in Photoresists Processing*, 2013.
- [42] MicroChemicals, *Exposure of Photoresists*, 2013.

- [43] S. S. P. Parkin, *Ultrathin Magnetic Structures II* (Springer Berlin Heidelberg, Berlin, Heidelberg, 1994), pp. 148–186.
- [44] E. Montoya, T. McKinnon, A. Zamani, E. Girt, and B. Heinrich, “Broadband ferromagnetic resonance system and methods for ultrathin magnetic films”, *J. Magn. Magn. Mater.* **356**, 12 (2014).
- [45] I. S. Maksymov and M. Kostylev, “Broadband stripline ferromagnetic resonance spectroscopy of ferromagnetic films, multilayers and nanostructures”, *Phys. E Low-Dimensional Syst. Nanostructures* **69**, 253 (2015).
- [46] J. Beik Mohammadi, J. M. Jones, S. Paul, B. Khodadadi, C. K. A. Mewes, T. Mewes, and C. Kaiser, “Broadband ferromagnetic resonance characterization of anisotropies and relaxation in exchange-biased IrMn/CoFe bilayers”, *Phys. Rev. B* **95**, 064414 (2017).
- [47] J. C. Scott, “Ferromagnetic resonance studies in the bilayer system Ni 0.80 Fe 0.20 / Mn 0.50 Fe 0.50 : Exchange anisotropy”, *J. Appl. Phys.* **57**, 3681 (1985).
- [48] R. D. McMichael, M. D. Stiles, P. J. Chen, and W. F. Egelhoff, “Ferromagnetic resonance linewidth in thin films coupled to NiO”, *J. Appl. Phys.* **83**, 7037 (1998).
- [49] O. Yaln, ed., *Ferromagnetic Resonance - Theory and Applications* (InTech, July 2013).
- [50] T. Kodama, S. Tomita, T. Kato, D. Oshima, S. Iwata, S. Okamoto, N. Kikuchi, O. Kitakami, N. Hosoito, and H. Yanagi, “Ferromagnetic Resonance of a Single Magnetochiral Metamolecule of Permalloy”, *Phys. Rev. Appl.* **6**, 024016 (2016).
- [51] R. Gross and A. Marx, *Festkörperphysik*, 2nd ed. (De Gruyter Oldenbourg, München, 2014), p. 1006.
- [52] J. M. MacLaren, T. C. Schulthess, W. H. Butler, R. Sutton, and M. McHenry, “Electronic structure, exchange interactions, and Curie temperature of FeCo”, *J. Appl. Phys.* **85**, 4833 (1999).
- [53] L. Landau and E. Lifshits, “On the Theory of the Dispersion of Magnetic Permeability in Ferromagnetic Bodies”, *Phys. Z. Sowietunion* **8** (1935) 2071–0194.
- [54] T. Gilbert, “Classics in Magnetism A Phenomenological Theory of Damping in Ferromagnetic Materials”, *IEEE Trans. Magn.* **40**, 3443 (2004).
- [55] L. Liensberger, “Spin-Orbit Torques and Magnetization Dynamics in Non-collinear Magnets”, Master Thesis (Technische Universität München, 2017).
- [56] C. Kittel, “On the theory of ferromagnetic resonance absorption”, *Phys. Rev.* **73**, 155 (1948).
- [57] D. Polder, “On the theory of ferromagnetic resonance”, London, Edinburgh, Dublin *Philos. Mag. J. Sci.* **40**, 99 (1949).
- [58] A. G. Gurevich and G. A. Melkov, *Magnetization Oscillations and Waves* (CRC Press, 1996), p. 464.

- [59] B. Lax and K. J. Button, *Microwave Ferrites and Ferrimagnetics* (McGraw-Hill, 1962), p. 752.
- [60] P. D. Louis, “Broadband-Spectroscopy of Magnetic Materials at Low Temperatures”, Master Thesis (Technische Universität München, 2016).
- [61] D. D. Stancil and A. Prabhakar, *Spin Waves* (Springer, Boston, Ma, 2009), p. 332.
- [62] L. Dreher, M. Weiler, M. Pernpeintner, H. Huebl, R. Gross, M. S. Brandt, and S. T. B. Goennenwein, “Surface acoustic wave driven ferromagnetic resonance in nickel thin films: Theory and experiment”, *Phys. Rev. B* **86**, 134415 (2012).
- [63] Y. Tserkovnyak, A. Brataas, and G. E. W. Bauer, “Enhanced Gilbert Damping in Thin Ferromagnetic Films”, *Phys. Rev. Lett.* **88**, 117601 (2002).
- [64] Y. Tserkovnyak, A. Brataas, G. E. W. Bauer, and B. I. Halperin, “Nonlocal magnetization dynamics in ferromagnetic heterostructures”, *Rev. Mod. Phys.* **77**, 1375 (2005).
- [65] A. Brataas, Y. Tserkovnyak, and G. E. Bauer, “Spin-pumping in ferromagnet-normal metal systems”, *J. Magn. Magn. Mater.* **272-276**, 1981 (2004).
- [66] O. Mosendz, J. E. Pearson, F. Y. Fradin, G. E. W. Bauer, S. D. Bader, and A. Hoffmann, “Quantifying Spin Hall Angles from Spin Pumping: Experiments and Theory”, *Phys. Rev. Lett.* **104**, 046601 (2010).
- [67] K. Ando, Y. Kajiwara, K. Sasage, K. Uchida, and E. Saitoh, “Inverse spin-hall effect induced by spin pumping in various metals”, *IEEE Trans. Magn.* **46**, 3694 (2010).
- [68] A. Kapelrud and A. Brataas, “Spin Pumping and Enhanced Gilbert Damping in Thin Magnetic Insulator Films”, *Phys. Rev. Lett.* **111**, 097602 (2013).
- [69] M. V. Costache, M. Sladkov, S. M. Watts, C. H. van der Wal, and B. J. van Wees, “Electrical Detection of Spin Pumping due to the Precessing Magnetization of a Single Ferromagnet”, *Phys. Rev. Lett.* **97**, 216603 (2006).
- [70] E. Saitoh, M. Ueda, H. Miyajima, and G. Tatara, “Conversion of spin current into charge current at room temperature: Inverse spin-Hall effect”, *Appl. Phys. Lett.* **88**, 182509 (2006).
- [71] G. Woltersdorf, O. Mosendz, B. Heinrich, and C. H. Back, “Magnetization Dynamics due to Pure Spin Currents in Magnetic Double Layers”, *Phys. Rev. Lett.* **99**, 246603 (2007).
- [72] M. Weiler, M. Althammer, M. Schreier, J. Lotze, M. Pernpeintner, S. Meyer, H. Huebl, R. Gross, A. Kamra, J. Xiao, Y.-T. Chen, H. Jiao, G. E. W. Bauer, and S. T. B. Goennenwein, “Experimental Test of the Spin Mixing Interface Conductivity Concept”, *Phys. Rev. Lett.* **111**, 176601 (2013).
- [73] M. Althammer, “Pure spin currents in magnetically ordered insulator/normal metal heterostructures”, *47* (2018).

- [74] M. A. W. Schoen, D. Thonig, M. L. Schneider, T. J. Silva, H. T. Nembach, O. Eriksson, O. Karis, and J. M. Shaw, “Ultra-low magnetic damping of a metallic ferromagnet”, *Nat. Phys.* **12**, 839 (2016).
- [75] M. Hiebel, *Fundamentals of Vector Network Analysis* (Rhode & Schwarz, Portsmouth, NH, U.S.A., 2007), p. 420.
- [76] O. Karlqvist, *Calculation of the magnetic field in the ferromagnetic layer of a magnetic drum*, 1954.
- [77] H. T. Nembach, T. J. Silva, J. M. Shaw, M. L. Schneider, M. J. Carey, S. Maat, and J. R. Childress, “Perpendicular ferromagnetic resonance measurements of damping and Landè g-factor in sputtered (Co<sub>2</sub>Mn)<sub>1-x</sub>Gex thin films”, *Phys. Rev. B* **84**, 054424 (2011).
- [78] J. M. Shaw, H. T. Nembach, and T. J. Silva, “Measurement of orbital asymmetry and strain in Co<sub>90</sub>Fe<sub>10</sub> / Ni multilayers and alloys: Origins of perpendicular anisotropy”, *Phys. Rev. B* **87**, 054416 (2013).
- [79] M. Farle, B. Mirwald-Schulz, A. Anisimov, W. Platow, and K. Baberschke, “Higher-order magnetic anisotropies and the nature of the spin-reorientation transition in face-centered-tetragonal Ni(001)/Cu(001)”, *Phys. Rev. B - Condens. Matter Mater. Phys.* **55**, 3708 (1997).
- [80] C. Kittel, “On the Gyromagnetic Ratio and Spectroscopic Splitting Factor of Ferromagnetic Substances”, *Phys. Rev.* **76**, 743 (1949).
- [81] C. Kittel, W. Yager, and F. Merritt, “On the Gorter normal field ferromagnetic resonance experiment”, *Physica* **15**, 256 (1949).
- [82] F. Gimbert and L. Calmels, “First-principles investigation of the magnetic anisotropy and magnetic properties of Co/Ni(111) superlattices”, *Phys. Rev. B* **86**, 184407 (2012).
- [83] P. Bruno, “Tight-binding approach to the orbital magnetic moment and magnetocrystalline anisotropy of transition-metal monolayers”, *Phys. Rev. B* **39**, 865 (1989).
- [84] G. Woltersdorf, “Spin-pumping and Two-magnon Scattering in Magnetic Multilayers”, PhD thesis (Simon Fraser University, 2004).
- [85] R. Arias and D. L. Mills, “Extrinsic contributions to the ferromagnetic resonance response of ultrathin films”, *Phys. Rev. B* **60**, 7395 (1999).
- [86] L. Chen, S. Mankovsky, S. Wimmer, M. A. W. Schoen, H. S. Körner, M. Kronseder, D. Schuh, D. Bougeard, H. Ebert, D. Weiss, and C. H. Back, “Emergence of anisotropic Gilbert damping in ultrathin Fe layers on GaAs(001)”, *Nat. Phys.* **14**, 490 (2018).
- [87] J. Seib, D. Steiauf, and M. Fähnle, “Linewidth of ferromagnetic resonance for systems with anisotropic damping”, *Phys. Rev. B* **79**, 092418 (2009).

- 
- [88] D. Steiauf and M. Fähnle, “Damping of spin dynamics in nanostructures: An ab initio study”, *Phys. Rev. B* **72**, 064450 (2005).
- [89] V. L. Safonov, “Tensor form of magnetization damping”, *J. Appl. Phys.* **91**, 8653 (2002).
- [90] K. Gilmore, M. D. Stiles, J. Seib, D. Steiauf, and M. Fähnle, “Anisotropic damping of the magnetization dynamics in Ni, Co, and Fe”, *Phys. Rev. B* **81**, 174414 (2010).
- [91] V. E. Demidov, S. Urazhdin, A. Zholud, A. V. Sadovnikov, and S. O. Demokritov, “Nanoconstriction-based spin-Hall nano-oscillator”, *Appl. Phys. Lett.* **105**, 172410 (2014).
- [92] Y. Li, X. de Milly, F. Abreu Araujo, O. Klein, V. Cros, J. Grollier, and G. de Loubens, “Probing Phase Coupling Between Two Spin-Torque Nano-Oscillators with an External Source”, *Phys. Rev. Lett.* **118**, 247202 (2017).
- [93] J. B. Youssef and C. Brosseau, “Magnetization damping in two-component metal oxide micropowder and nanopowder compacts by broadband ferromagnetic resonance measurements”, *Phys. Rev. B* **74**, 214413 (2006).
- [94] D. Wu, Z. Zhang, L. Li, Z. Zhang, H. B. Zhao, J. Wang, B. Ma, and Q. Y. Jin, “Perpendicular magnetic anisotropy and magnetization dynamics in oxidized CoFeAl films”, *Sci. Rep.* **5**, 12352 (2015).
- [95] M. V. Costache, M. Zaffalon, and B. J. van Wees, “Spin accumulation probed in multiterminal lateral all-metallic devices”, *Phys. Rev. B* **74**, 012412 (2006).
- [96] F. J. Jedema, H. B. Heersche, A. T. Filip, J. J. A. Baselmans, and B. J. van Wees, “Electrical detection of spin precession in a metallic mesoscopic spin valve”, *Nature* **416**, 713 (2002).
- [97] E. R. J. Edwards, H. T. Nembach, and J. M. Shaw, “Co<sub>25</sub>Fe<sub>75</sub> Thin Films with Ultralow Total Damping”, (2018).
- [98] A. J. Lee, J. T. Brangham, Y. Cheng, S. P. White, W. T. Ruane, B. D. Esser, D. W. McComb, P. C. Hammel, and F. Yang, “Metallic ferromagnetic films with magnetic damping under 0.0014”, *Nat. Commun.* **8**, 234 (2017).
- [99] C. T. Boone, H. T. Nembach, J. M. Shaw, and T. J. Silva, “Spin transport parameters in metallic multilayers determined by ferromagnetic resonance measurements of spin-pumping”, *J. Appl. Phys.* **113**, 153906 (2013).
- [100] S. Yakata, Y. Ando, T. Miyazaki, and S. Mizukami, “Temperature dependences of spin-diffusion lengths of Cu and Ru layers”, *Japanese J. Appl. Physics, Part 1 Regul. Pap. Short Notes Rev. Pap.* **45**, 3892 (2006).
- [101] L. Brillouin, “Diffusion de la lumière et des rayons X par un corps transparent homogène”, *Ann. Phys. (Paris)*. **9**, 88 (1922).
- [102] T. Sebastian, K. Schultheiss, B. Obry, B. Hillebrands, and H. Schultheiss, “Micro-focused Brillouin light scattering: imaging spin waves at the nanoscale”, *Front. Phys.* **3**, 1 (2015).

- [103] C. Mühlenhoff, “Microwave Frequency Magnetoacoustic Interactions in Ferromagnetic Thin Films”, Master Thesis (Technische Universität München, 2017).
- [104] J. Sandercock, *Tandem Fabry-Perot Interferometer TFP-1*, tech. rep. (2009), pp. 1–82.
- [105] V. E. Demidov, S. Urazhdin, R. Liu, B. Divinskiy, A. Telegin, and S. O. Demokritov, “Excitation of coherent propagating spin waves by pure spin currents”, *Nat. Commun.* **7**, 10446 (2016).
- [106] H. T. Nembach, J. M. Shaw, M. Weiler, E. Jué, and T. J. Silva, “Linear relation between Heisenberg exchange and interfacial Dzyaloshinskii-Moriya interaction in metal films”, Master Thesis (Simon Fraser University, 2015), pp. 825–829.
- [107] M. Bailleul, D. Olligs, and C. Fermon, “Propagating spin wave spectroscopy in a permalloy film: A quantitative analysis”, *Appl. Phys. Lett.* **83**, 972 (2003).
- [108] B. A. Kalinikos and A. N. Slavin, “Theory of dipole-exchange spin wave spectrum for ferromagnetic films with mixed exchange boundary conditions”, *J. Phys. C Solid State Phys.* **19**, 7013 (1986).
- [109] J. Stigloher, M. Decker, H. S. Körner, K. Tanabe, T. Moriyama, T. Taniguchi, H. Hata, M. Madami, G. Gubbiotti, K. Kobayashi, T. Ono, and C. H. Back, “Snell’s Law for Spin Waves”, *Phys. Rev. Lett.* **117**, 037204 (2016).
- [110] O. Gladii, D. Halley, Y. Henry, and M. Bailleul, “Spin-wave propagation and spin-polarized electron transport in single-crystal iron films”, *Phys. Rev. B* **96**, 174420 (2017).
- [111] J.-Y. Chauleau, H. G. Bauer, H. S. Körner, J. Stigloher, M. Härtinger, G. Woltersdorf, and C. H. Back, “Self-consistent determination of the key spin-transfer torque parameters from spin-wave Doppler experiments”, *Phys. Rev. B* **89**, 020403 (2014).
- [112] H. S. Körner, M. A. W. Schoen, T. Mayer, M. M. Decker, J. Stigloher, T. Weindler, T. N. G. Meier, M. Kronseder, and C. H. Back, “Magnetic damping in poly-crystalline Co 25 Fe 75 : Ferromagnetic resonance vs. spin wave propagation experiments”, *Appl. Phys. Lett.* **111**, 132406 (2017).
- [113] V. V. Kruglyak, S. O. Demokritov, and D. Grundler, “Magnonics”, *J. Phys. D. Appl. Phys.* **43**, 264001 (2010).
- [114] A. A. Awad, P. Dürrenfeld, A. Houshang, M. Dvornik, E. Iacocca, R. K. Dumas, and J. Åkerman, “Long-range mutual synchronization of spin Hall nano-oscillators”, *Nat. Phys.* **13**, 292 (2016).
- [115] C. Moreau-Luchaire, C. Moutafis, N. Reyren, J. Sampaio, C. A. F. Vaz, N. Van Horne, K. Bouzehouane, K. Garcia, C. Deranlot, P. Warnicke, P. Wohlhüter, J.-M. George, M. Weigand, J. Raabe, V. Cros, and A. Fert, “Additive interfacial chiral interaction in multilayers for stabilization of small individual skyrmions at room temperature”, *Nat. Nanotechnol.* **11**, 444 (2016).
- [116] A. N. Bogdanov and U. K. Röbber, “Chiral Symmetry Breaking in Magnetic Thin Films and Multilayers”, *Phys. Rev. Lett.* **87**, 037203 (2001).

# Acknowledgments

Throughout this year, working on this thesis, I experienced a lot of support in many kinds of ways. I'd like to thank several people, whose help made this work possible. I would like to thank:

Prof. Dr. Rudolf Gross, for offering me the possibility to realize my master thesis at the Walther-Meißner Institut and supporting us as students.

Dr. Mathias Weiler as my supervisor. I am grateful, for his open ears to my questions and problems. For always taking the time needed to draw a bigger picture and if necessary give more extensive explanations which allow me to gain a deeper understanding. Your ample knowledge motivates me. Thank you very much for the repeated proof-reading and all the effort you invested in me.

Dr. Matthias Althammer as my supervisor. For all the support during the fabrication process and sharing his experience with me. His ever patient help with the SUPERBOWL and resolving all kinds of problems. Without him, all the fabrication would have been way more difficult. For your frequently visits in my office and demonstrating interest in my progress. Thank you also very much for the proof-reading and your time invested.

Dr. Frank Deppe for his support and sharing his experience with the optical lithography and the spin coating. Thank you for accompanying me in the different progress steps with the PicoMaster and the conversations with the PicoMaster support.

Dr. Stephan Geprägs for his support on the reflectometry measurements and technical questions.

Lukas Liensberger for the collaboration on the BLS measurements. Thank you for all the times you spent explaining physics, data processing and programming to me.

Tom Brenninger for his frequent support at the SUPERBOWL.

Christoph Scheuer as my student assistant helping me with optimizing the spin coating process and exposure dose. Thank you for your time spent making SEM pictures for quality feedback.

Birte Coester and Uli Zweck, my office colleagues for the kind atmosphere. For the physics and non-physics related talks and taking a break together when needed.

The workshop crew for their fast and kind support when I needed special laboratory equipment fabricated.

All the WMI members filling this place with a good mood and a friendly and productive atmosphere.

My family and in special my mother, Isabel Sanchez, for the never ceasing love and support. Thank you all, for the comfort, peace, encouragement, advices and making this family so precious.

I thank God for being my hope. He is my source of comfort and joy. For his son Jesus Christ who gave his life for me and shows me who I want to be.